

DELFT UNIVERSITY
OF TECHNOLOGY

VAN OORD DREDGING &
MARINE CONTRACTORS

MASTER THESIS

Fatigue Analysis and Loading Scenarios of Steel Chain Links used for Subsea Rock Installation

CONFIDENTIAL

Author:

W.N. DE WILDT

Graduation committee:

Prof. dr. A. METRIKINE

Dr. M.A.N. HENDRIKS

Dr. A. ROMELJN

Ir. J.S. HOVING

Company Supervisor:

Ir. J.R. VOORMOLEN

*A thesis submitted in fulfilment of the requirements
for the degree of Master of Science*

in the

Offshore and Dredging Engineering
Mechanical, Maritime and Materials Engineering

August 2013

"An investment in knowledge always pays the best interest."

Benjamin Franklin

DELFT UNIVERSITY OF TECHNOLOGY
VAN OORD

Abstract

Faculty of Materials, Mechanical and Maritime Engineering
Offshore and Dredging Engineering

Master of Science

Fatigue Analysis and Loading Scenarios of Steel Chain Links used for Subsea Rock Installation

by W.N. DE WILDT

This study analyses the fatigue failure and the loading scenarios of steel chain links used for suspending a Flexible Fall Pipe during Subsea Rock Installation. For that purpose, OrcaFlex is used to evaluate and quantify the global loading conditions in the chain links during the Subsea Rock Installation process. In Ansys, a Finite Element Model is created which investigates the chain links on a local scale when subjected to the loading conditions from OrcaFlex. Further, through an analytical design process and fatigue testing experiments, fatigue curves are constructed under various conditions. As a result, a method has been established for predicting the fatigue damage factor over the length of the Flexible Fall Pipe chains for various conditions, inter alia water depth, wave height and rock installation rate. Fatigue was found mainly in the upper part of the Flexible Fall Pipe chains. The level of fatigue increases rapidly and further down the Flexible Fall Pipe with increasing working depth and wave height. Additionally, it was found that chain link rotations can increase the peak stresses and the effect is larger with a higher friction factor. For further study, it is recommended to verify the OrcaFlex model by means of tests in a towing tank and the established fatigue curves by means of further fatigue testing experiments.

Acknowledgements

Writing a thesis is a long and laborious process that knows many ups and downs. For me, the coaching in this process was very important to have. Therefore, I would like to express my gratitude to my graduation committee. What I really value is that, even with all your busy schedules, it was possible for me to drop by for questions or a discussion on short notice. Andrei, at the very start you pointed me in the right direction and you have a clear view on how to approach a thesis, thank you for that. Arie, my thanks go to you for your valuable input in the fatigue area, the suggestion of analytically deriving the fatigue curves has a high added value to my thesis. Max, I have been stuck in my Finite Element Analysis many times, but each time your pointers gave me something to work on, I appreciate it. Jeroen, with any question, I can count on your advice which has been very helpful, thank you. Job, at the start of my thesis you told me that you do not want to have too many graduates, as you want to be able to give them qualitatively good coaching. For me, you have more than succeeded in that, and you are particularly good at keeping me out of the 'hassle of the day', which enabled me to focus on my thesis. My gratitude goes to Robert for having countless fatigue discussions with me, you are a sound sparring partner. Thanks go to my girlfriend, for supporting me during my thesis and for giving me some valuable input. Surely, there are many more people involved who have helped me in the process of writing my thesis, and for those whom I have not named, thank you. Finally, many thanks go to Van Oord, for giving me the opportunity to write my thesis on a very interesting subject.

Contents

Abstract	ii
Acknowledgements	iii
List of Figures	vii
List of Tables	ix
Abbreviations	x
Symbols	xi
1 Introduction	1
2 Problem Description	2
2.1 Background of the Problem	2
2.1.1 System Description	3
2.1.1.1 Subsea Rock Installation Process in General	3
2.1.1.2 Bucket Guidance Frame and Measurement System	4
2.1.1.3 Flexible Fall Pipe	5
2.1.2 Flexible Fall Pipe Incidents	8
2.2 Statement of the Problem	9
2.3 Theoretical Framework	10
2.3.1 Methods for Assessing Fatigue	10
2.3.1.1 Fracture Based Mechanics	11
2.3.1.2 Strain-life Approach	11
2.3.1.3 Stress-life Approach	12
2.3.2 Fatigue Life of Mooring Chain	14
2.3.3 Effect of Proof Loading on the Fatigue Life of Chain	15
2.3.4 Effect of Mean Load on the Fatigue Life of Chain	16
2.3.5 Failure of Chains by Out-of-Plane Bending	17
2.3.6 Low Temperature Fatigue Behavior of Steels	18
2.4 Significance of the Study	19
3 Methodology	21
3.1 Objective of the Study	21
3.2 Research Approach	21

3.3	Procedure	22
3.3.1	OrcaFlex Numerical Model	22
3.3.1.1	Modeling of the Vessel	22
3.3.1.2	Modeling of the Flexible Fall Pipe System	23
3.3.1.3	OrcaFlex Loading Scenarios	25
3.3.2	Finite Element Model of the Chain Link	26
3.3.2.1	Creating the Finite Element Model	27
3.3.2.2	Finite Element Model Loading Scenarios	27
3.3.3	Fatigue Testing of the Chain Links	30
3.3.4	Analytical Derivation of the Fatigue Curve	30
3.4	Data Processing and Analysis	31
4	Results	33
4.1	OrcaFlex Results	33
4.1.1	Calibration and Validation of the OrcaFlex Model	33
4.1.1.1	Hysteresis in the Measurement Frame	35
4.1.1.2	Effect of Rock Friction on the Chain Tension	36
4.1.2	OrcaFlex Loading Scenarios Results	37
4.1.2.1	General Loading Scenarios Results	37
4.1.2.2	Extreme Current Scenarios Results	39
4.1.2.3	Directional Current Profiles Scenarios Results	40
4.1.2.4	Subsea Rock Installation Scenarios Results	40
4.1.2.5	Deepwater Buckets Scenarios Results	41
4.1.2.6	Vessel Loading Condition Scenario Results	42
4.1.2.7	Chain Link Rotations	42
4.2	Results from Finite Element Model of the Chain Link	43
4.2.1	Quarter Chain Link Model	43
4.2.2	Full Chain Link Model	46
4.2.2.1	Contact Analysis	46
4.2.2.2	Analysing the Stress Distribution	47
4.2.2.3	Chain Link Rotations	48
4.3	Results from the Fatigue Testing of the Chain Links	50
4.4	Results from the Analytical Derivation of the Fatigue Curves	51
4.4.1	Fatigue Curve Predictions	59
4.5	Fatigue Predictions	61
4.5.1	Fatigue Range Graphs	61
4.5.2	Radio Frequency IDentification	62
4.5.3	Safety Factors	62
4.5.3.1	Fatigue Safety Factor	63
4.5.3.2	Safe Working Load and Safety Factor	64
4.5.4	Subsea Rock Installation in Arctic Conditions	65
5	Discussion	66
5.1	Purpose of the Study	66
5.2	Methods and Procedures	66
5.3	Major Findings	67
5.4	Discussion	70

5.4.1	OrcaFlex Loading Scenarios	71
5.4.2	Finite Element Model of the Chain Link	71
5.4.3	Fatigue Testing of the Chain Links	72
5.4.4	Analytical Derivation of the Fatigue Curve	72
6	Conclusion	74
6.1	Conclusion	74
6.1.1	Conclusions from Loading Scenarios	75
6.1.2	Conclusions from Fatigue Analysis	76
6.2	Recommendations	77
6.2.1	Recommendations for Further Study	77
6.2.2	Practical Recommendations	79
A	System Overview	81
B	Environmental Conditions	84
C	Theory	86
C.1	OrcaFlex Theory	86
C.1.1	Global Theory	86
C.1.2	Environment Theory	87
C.1.3	Line Theory	87
C.1.4	Buoys, Shapes and Winches	87
C.2	Nominal Stress in the Chain Link	88
C.3	Analytical Derivation of the Fatigue Curve	89
D	Results	91
D.1	Calibration and Validation Results	94
D.1.1	Time Series	94
D.1.2	Frequency Spectra	98
D.2	General Loading Conditions Results	101
D.3	Extreme Current Scenarios Results	110
D.4	Directional Current Profiles Scenarios Results	110
D.5	Subsea Rock Installation Scenarios Results	110
D.6	Deepwater Buckets Scenarios Results	112
D.7	Vessel Loading Condition Scenario Results	114
D.8	Finite Element Model Results	114
	Bibliography	116

List of Figures

2.1	Flexible Fall Pipe Vessel Nordnes	4
2.2	Bucket and chain winch	4
2.3	Bucket guidance frame and FFP configuration	5
2.4	Flexible Fall Pipe configuration	5
2.5	Dominator connection link	6
2.6	Chain link and plastic attachment	6
2.7	Remotely Operated Vehicle in operations	7
2.8	Proposed Radio Frequency Identification system	8
2.9	Fatigue fracture surface of a chain link	11
2.10	Definition of cyclic stress	13
2.11	S-N curve	13
2.12	Rainflow counting algorithm	15
2.13	Fatigue curves for mooring chain	15
2.14	Constant life curve	17
3.1	Graphical representation of the Umbilical Moonpool Frame	23
3.2	Umbilical Moonpool Frame modeled in OrcaFlex	23
3.3	Representation of the Solid186-element with 20 nodes	27
3.4	Quarter of a chain link in ANSYS	27
3.5	FEM loading scenarios for the quarter chain link	28
3.6	FEM loading scenarios for the full chain links	29
3.7	Experimental set-up for fatigue testing at TNO	30
4.1	Modeled and measured chain tension	34
4.2	Modeled and measured chain tension - frequency spectrum	34
4.3	Hysteresis in the measurement frame	36
4.4	Effect of rock friction on the chain tension	36
4.5	Rock friction as a function of dumping rate	37
4.6	Chain tension in time - scenario 11	37
4.7	Chain tension range graph - scenario 11	38
4.8	Chain tension range graph - scenario 11, 12, 13	39
4.9	UMF contact force for three extreme current distributions	40
4.10	UMF contact force for directional current	40
4.11	Chain tension comparison - SRI versus increased self weight	41
4.12	Range graph normal buckets and deepwater buckets	41
4.13	UMF contact force for normal and deepwater buckets	42
4.14	Chain tension - Stornes 100% loaded versus 25% loaded	42
4.15	FEM loading scenarios for the quarter chain link	43

4.16	Quarter chain link - Finite Element Analysis versus analytical solution . . .	44
4.17	Representation of the contact elements in ANSYS	46
4.18	Full chain link FEM results - Von Mises peak stresses	47
4.19	Chain link rotations FEM results - Von Mises peak stresses	48
4.20	Full chain link FEM results - chain link rotations case 1	49
4.21	Full chain link FEM results - chain link rotations case 2	50
4.22	Fatigue testing results and fatigue curves from literature	51
4.23	Synthetic fatigue curve	52
4.24	Stress-strain diagram	53
4.25	Stress gradient χ^* at the inner bend region of the chain link	54
4.26	Quantifying the mean stress influence factor F_m	56
4.27	Synthetic fatigue curve and fatigue testing results	57
4.28	Endurance limit N_D as a function of fatigue curve slope k	58
4.29	Modified synthetic fatigue curve and fatigue testing results	59
4.30	Effect of mean stress on position of synthetic fatigue curve	60
4.31	Effect of surface roughness on position of synthetic fatigue curve	60
4.32	Fatigue damage factor for scenario 11	61
4.33	Example of 2.5% exceedance level fatigue curve	64
5.1	Chain tension range graph - scenario 11, 12, 13	67
5.2	Stress distribution full chain link	68
5.3	Fatigue testing results and fatigue curves from literature	69
5.4	Effect of mean stress on position of synthetic fatigue curve	69
5.5	Fatigue damage factor for scenario 11	70
A.1	Flexible Fall Pipe Vessel Stornes: side and top view	82
A.2	Steel bucket: dimensions and geometry	82
A.3	Dominator connection links dimensions	82
A.4	Round steel chain link: dimensions and geometry	82
B.1	Location of the Ormen Lange field	84
B.2	Annual wave height and period distribution at Ormen Lange	85
B.3	Annual wave height and direction at Ormen Lange	85
B.4	Limit case current profiles at the Ormen Lange field	85
C.1	OrcaFlex structural model	88
C.2	Free Body Diagram of the chain link	89
C.3	Design process for the analytical derivation of the fatigue curve	90

List of Tables

3.1	Ormen Lange base case loading scenario	25
3.2	Fatigue testing specifications	31
4.1	FEM results - quarter chain link case 1	45
4.2	FEM results - quarter chain link case 2	45
4.3	Friction factor and maximum rotation	49
4.4	Fatigue testing results	50
4.5	Results from the analytical derivation of the fatigue curve	59
A.1	Flexible Fall Pipe Vessel Stornes	81
A.2	Round steel chain link: spectral analysis	82
A.3	Specifications: chain link, Dominator connection link and steel bucket . .	83
D.1	Results overview - calibration and validation	91
D.2	Results overview - general loading scenarios	92
D.3	Results overview - other loading scenarios	93

Abbreviations

API	American Petroleum Institute
DNV	Det Norske Veritas
DP	Dynamic Positioning
FDF	Fatigue Damage Factor
FEA	Finite Element Analysis
FEM	Finite Element Modeling
FFP	Flexible Fall Pipe
FFPV	Flexible Fall Pipe Vessel
FPS	Floating Production System
JIP	Joint Industry Project
MBL	Minimum Break Load
RAO	Response Amplitude Operator
RFID	Radio Frequency IDentification
ROV	Remotely Operated Vehicle
SCF	Stress Concentration Factor
SRI	Subsea Rock Installation
UMF	Umbilical Moonpool Frame

Symbols

α	angle	°
α_k	form factor	—
β_k	notch factor	—
γ_F	fatigue safety factor	—
γ_L	working load safety factor	—
μ	friction factor	—
σ_a	stress amplitude	Nmm^{-2}
σ_{aD}	synthetic endurance limit stress	Nmm^{-2}
$\sigma_{aDfictive}$	fictive synthetic endurance limit stress	Nmm^{-2}
σ_e	endurance limit stress	Nmm^{-2}
σ_m	mean stress	Nmm^{-2}
σ_{nom}	nominal stress	Nmm^{-2}
σ_{peak}	peak stress	Nmm^{-2}
σ_r	stress range	Nmm^{-2}
σ_t	threshold fatigue stress	Nmm^{-2}
σ_W	fatigue strength material	Nmm^{-2}
σ_{Wk}	fatigue strength component	Nmm^{-2}
χ^*	stress gradient	mm^{-1}
d_c	characteristic fatigue damage	—
d_F	adjacent fatigue damage ratio	—
F	external force	N
F_0	surface factor	—
F_{0T}	technological and surface factor	—
F_{0Tk}	fatigue strength reduction factor	—

F_m	mean stress influence factor	—
F	force	N
F_p	force perpendicular to cross-section	N
F_t	force transverse to cross-section	N
F_T	technological factor	—
I	area moment of inertia	m ⁴
K	intercept parameter	—
k	slope synthetic fatigue curve	—
M	mean stress sensitivity	—
M_b	bending moment	Nm
m	slope fatigue curve	—
N	number of cycles	—
n	supporting factor	—
N_D	endurance limit cycles	—
R	stress ratio	—
R_e	deformation limit stress	Nmm ⁻²
R_e^*	deformation fatigue limit stress	Nmm ⁻²
R_m	break strength	Nmm ⁻²
R_m^*	ultimate fatigue strength	Nmm ⁻²
$R_{p0.2}$	yield stress	Nmm ⁻²
R_z	surface roughness	μm
T	tension	N
W_b	section modulus (bending)	m ³
y	outer fiber distance	m

This page is left intentionally blank.

Chapter 1

Introduction

Van Oord is executing the largest Subsea Rock Installation (SRI) ever attempted in the North Sea. This requires the precise placement of millions of tonnes of rock in water depths approaching 1,000m. To accurately place the rocks on the sea bottom Van Oord uses a Flexible Fall Pipe (FFP). The Flexible Fall Pipe system consists of a series of open-ended buckets that are suspended from the vessel by means of two steel chains. During the operations, both static and dynamic loads are imposed on the Flexible Fall Pipe, and especially on the steel chains that suspend the Flexible Fall Pipe. Van Oord is moving into deeper water and continuously operating in more difficult conditions. To review the suitability of this system it is required to systematically look at the fatigue under the static and dynamic loading. Therefore, the two main goals of this research are (1) to find out what the magnitude and configuration of the external loading conditions is during the Subsea Rock Installation Process and (2) to gain more insight in the fatigue behavior of the Flexible Fall Pipe chains under these conditions. To reach the goals of this study, this thesis will use a combination of numerical modeling, theoretical modeling and experiments.

Contents This report starts with the Problem Description in Chapter 2, which gives an overview of the system, a description of the problem and a theoretical framework. The research methodology is discussed in Chapter 3, and describes what models will be constructed, how the problem will be approached and what the scope of the problem is. In Chapter 4, the results are presented and discussed for the different models. Chapter 5, Discussion, will summarize the major findings of this study and go into the points of discussion. In Chapter 6, conclusions are drawn, recommendations for further study are made and practical recommendations are discussed. In the Appendices section, additional system information and environmental conditions are presented, background theory is described and a full overview of all the results is given.

Chapter 2

Problem Description

This chapter starts with the background of the problem in Section 2.1, which includes a system description and a short overview of the incidents that have occurred with this system. Section 2.2 makes a statement of the problem and describes the gap in knowledge that will be addressed. In Section 2.3, this thesis is placed into context by means of a theoretical framework. Finally, the significance of the study is discussed in Section 2.4.

2.1 Background of the Problem

The offshore oil and gas industry has rapidly expanded over the last decades, with projects moving into deeper water and harsher conditions. Although the Flexible Fall Pipe Vessels (FFPV) Nordnes and Stornes have been designed for water depths up to 1200 meters, it is only recently that projects approaching these depths have come to market. Van Oord currently has operational experience for projects up to 900 meters water depth. Over the years, Van Oord has really specialized in performing the deepest, most challenging Subsea Rock Installation projects. Under the combined interaction of waves, current and the rock friction, the loading conditions on the Flexible Fall Pipe become more severe in deeper water. This will require a critical review of the system suitability for projects in deep water as new design criteria arise: fatigue failure of the chain from which the FFP is suspended. The importance of the design of the FFP for fatigue became evident in the autumn of 2012, when the FFP chains failed and the FFP landed on the Remotely Operated Vehicle (ROV). This clearly calls for an in depth investigation into the loading conditions that are sustained by the FFP chain and how this affects the fatigue life of the chain.

2.1.1 System Description

For the reader to gain a better understanding about the problem, first the Subsea Rock Installation process and the FFP system will be discussed. The order by which the FFP system is discussed is from top to bottom: it is started with the FFPV, followed by the guidance frame and measurement system, the actual Flexible Fall Pipe, the steel and plastic buckets, the chain, the connection links, the telescopic pipe, the Remotely Operated Vehicle and finally a Radio Frequency IDentification (RFID) system which is currently in development. Further, Section 2.1.2 will deal with the incidents that have taken place with the FFP system, which is one of the drivers for this research.

2.1.1.1 Subsea Rock Installation Process in General

Subsea Rock Installation is the process by which rocks are installed on the seabed for bottom-stability, free-span correction, cable or pipeline protection, scour protection or other reasons. The Subsea Rock Installation vessels that are in operation by Van Oord have different working principles. Side stone dumping vessels push the rocks over the side of the vessel, split hopper barges have an opening hull that releases the rocks and a Flexible Fall Pipe Vessel guides the rocks to the correct position by means of a Flexible Fall Pipe (de Heer, 2008). The FFP consists of open-ended buckets that are hung from two chains that are suspended by the vessel. The latter working principle, which uses the FFP to guide the rocks, is subject of this study. The two FFP vessels that are subject of this investigation are the Nordnes (Figure 2.1) and the Stornes. The Nordnes has a length of 166.7 meters and a water displacement of 35,966 tonnes; the Stornes has a length of 175 meters and a water displacement of 39,353 tonnes. Both vessels have a Dynamic Positioning Class 2 system, which maintains position during the Subsea Rock Installation process. The Stornes is Van Oord's latest FFPV, but the specifications of the vessel and the FFP system are very similar to those of the Nordnes. An overview of the Stornes and Nordnes, including additional specifications, can be found in Appendix A. In a quarry, the rocks are loaded into several cargo holds in the hull of the FFPV. When fully loaded, the FFPV sails to the Subsea Rock Installation location to discharge the rocks. By means of a double conveyor belt system the rocks can be continuously transported from the bottom cargo holds of the vessel along the deck to the moonpool, which is located at the center of the vessel. The moonpool is a rectangular open section of 7 by 5.6 m at the center of vessel, from where the FFP is suspended. The FFP is located at this particular location to minimize the effects of water and vessel motions. When the system is in operations, the conveyor belt system transports the rocks to the moonpool where the rocks are dumped into a funnel that guides the rocks into the FFP. The rocks then travel downwards through the FFP towards the seabottom. At

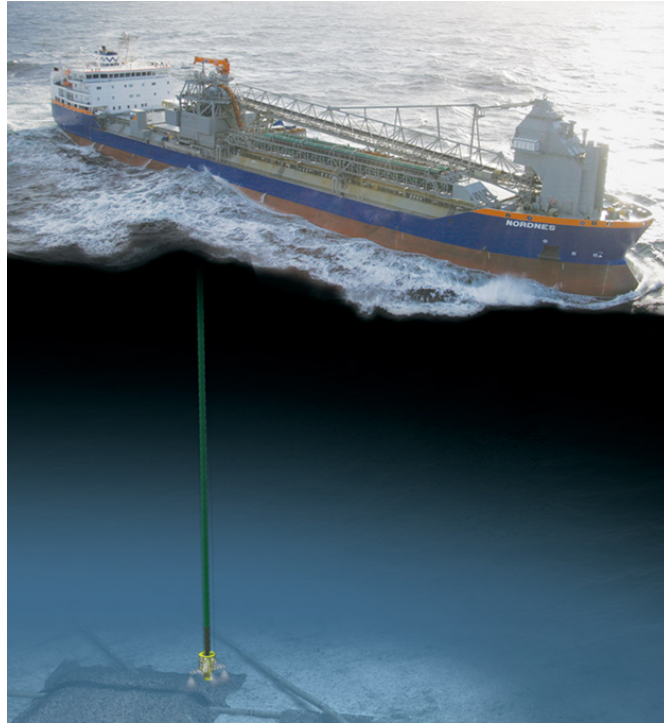


FIGURE 2.1: Flexible Fall Pipe Vessel Nordnes

the bottom part of the FFP, the ROV can correct the FFP position in the horizontal plane by means of thrusters. The rock deflector on the bottom of the ROV enables one to control the direction of rock flow.

2.1.1.2 Bucket Guidance Frame and Measurement System

On the FFPV, a winch is used to launch, recover and suspend the FFP. Both the portside and starboard chain run over this winch, which has a working principle similar to an anchor winch, as can be seen in Figure 2.2. The configuration of the FFP on the

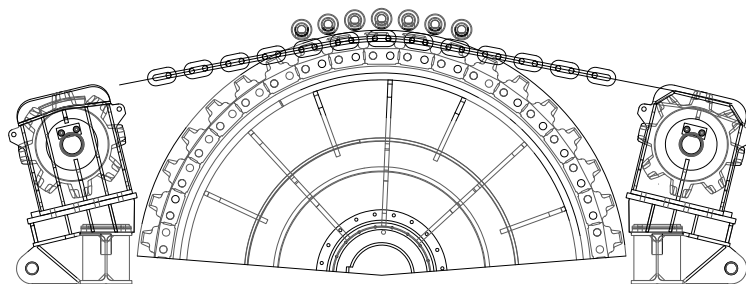


FIGURE 2.2: Bucket and chain winch

bucket guidance frame can be seen in Figure 2.3. This bucket guidance frame is located directly above the moonpool at the center of the FFP Vessel. The guidance frame that suspends the FFP has a measurement frame installed to measure the tension in the top

section of the FFP chains. When the tension in the chains exceeds certain limit values, this is registered by the measurement frame. As a result, production is stopped and measures are taken to reduce the tension in the FFP chains. In addition to the tension measurement system, there is a sensor in the moonpool area which logs motion data and rock flow rate. At the bottom of the FFP, the ROV is equipped with sensors that also capture motion data.

2.1.1.3 Flexible Fall Pipe

The Flexible Fall Pipe consists of steel and plastic buckets that are suspended from the FFPV by a portside and starboard chain. The top part of the FFP consists of ten steel buckets, as this part needs to be able to sustain the wave loading and rock impact without the buckets collapsing. The middle part of the FFP is made of plastic buckets as they do not have to sustain high loading, and these plastic buckets are buoyant. The bottom part of the FFP consists of twenty steel buckets. When the FFP is recovered, these last twenty buckets are stored on the bucket guidance frame, which makes it difficult to replace them. Therefore, these last buckets are made of steel, rather than plastic, so they can endure much longer. Also, the additional weight makes it easier to control the FFP during the launch. In Figure 2.4, it can be seen how the FFP runs from the bucket guidance frame, through the moonpool, to the ROV. The ROV is suspended by three umbilical wires, while the FFP is only suspended by the two chains. However, there are some small chains that connect the umbilical wires to the FFP chains, to keep the entire system together.

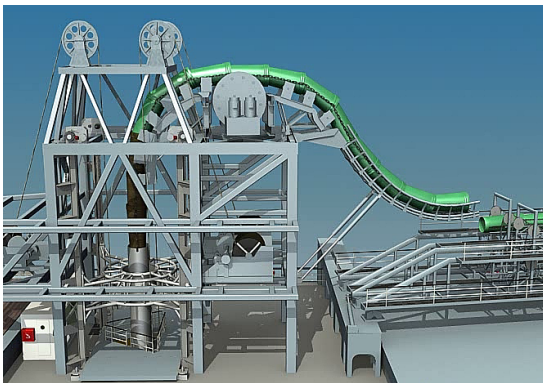


FIGURE 2.3: Bucket guidance frame and FFP configuration (B3D, 2013)

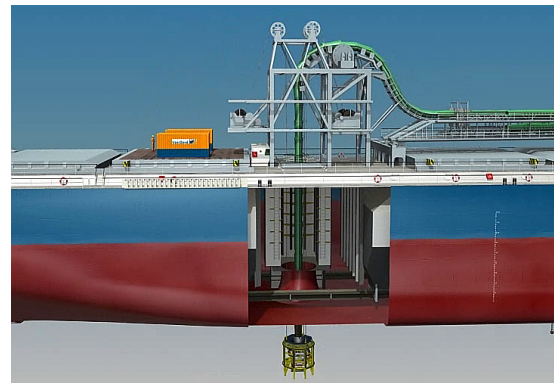


FIGURE 2.4: Flexible Fall Pipe configuration (B3D, 2013)

Steel and Plastic Buckets The buckets that are used on the FFPV *Stornes* and *Nordnes* are 1100-buckets, which means that the largest outer diameter of the buckets is 1100 mm. The buckets are tapered and hollow, which makes it unnecessary to add water to the system, as the water can flow freely through and along the buckets. An attachment

piece allows the buckets to hinge on the chain. The dimensions and specifications of the steel buckets can be found in Appendix A, Figure A.2 and Table A.3. The geometry and dimensions of the plastic buckets is very similar to the steel buckets. The steel buckets have a submerged weight of 400 kg, whereas the plastic buckets have a submerged weight of minus 5 kg.

Round Steel Chain Link The chain used to suspend the Flexible Fall Pipe is a 30x108 mm chain (Figure 2.6) which means that the diameter of the original bar is 30 mm and the effective length of the chain link is 108 mm. The FFP string consists of 17 meter chain sections (corresponding to 10 buckets) that are connected by special Dominator connection links that are discussed in the next paragraph. By building up the FFP string from 17 meter chain sections this enables the piece-wise replacement of string sections, in case part of the string is damaged and needs replacement. Both the chain and connection links are manufactured by the German company RUD, and this particular chain was originally manufactured for the mining industry. An overview of the dimensions, geometry and specifications of the chain can be found in Table A.3 and Figure A.4 in Appendix A.



FIGURE 2.5: Dominator connection link (RUD Ketten, 2012)



FIGURE 2.6: Chain link 30x108 mm and plastic attachment

Dominator Connection Link The 'Dominators' are special connection links that can be used to connect two strings of chain together (Figure 2.5). The Dominator consists of two parts that interlock by means of teethshaped protrusions. These two parts are then locked together by means of a locking pin that is hammered into the Dominator. An overview of the dimensions, geometry and specifications of the Dominator connection link can be found in Table A.3 and Figure A.3 in Appendix A.

Telescopic Pipe At the bottom of the FFP there is a telescopic pipe which can extend and retract. This mechanism allows for height adjustment (in case of a sloping seabed,

spring-neap effects or the vessel's change in draft) without having to stop production. The telescopic pipe is made out of three sections and during normal operations two sections are hanging on the FFP. The third section is supported by the ROV which hangs from the three umbilical wires. The submerged weight of the telescopic pipe is 2343 kg for the middle and upper section and 1174 kg for the bottom section that is supported by the ROV.

Remotely Operated Vehicle and Umbilical Wires The ROV is suspended from FFPV by means of three steel umbilical wires. Along the length, these umbilical wires are also connected to the FFP chains by means of small chains, for the purpose of keeping the umbilical wires and the FFP together in case of cross-flow. The global position of the FFP is determined by the FFPV, whereas the ROV ensures the precise placement of rocks on the sea bottom at the location of interest. Opening valves on the ROV direct the rock flow in the right direction and sensors on the ROV acquire data about the position, heading and other relevant variables. The mass of the ROV is 22 tonnes above water and 12 tonnes below the water surface. However, this load is suspended from the umbilical wires and not taken up by the FFP. Figure 2.7 illustrates what the ROV looks like during operations.

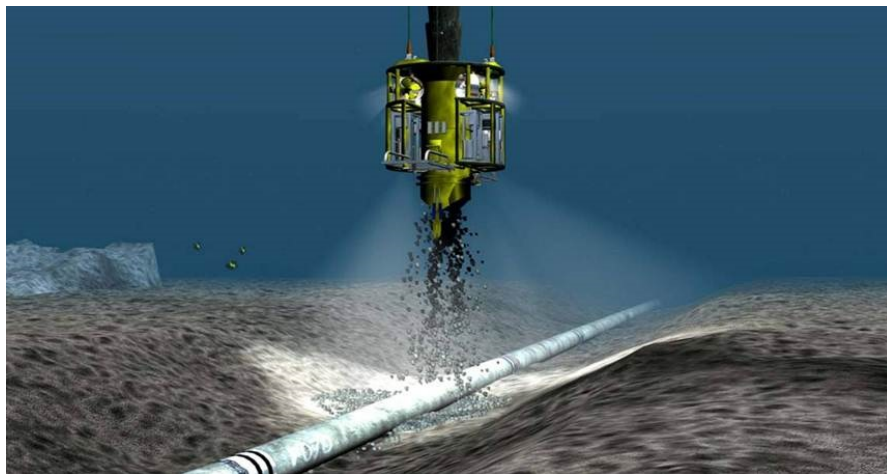


FIGURE 2.7: Remotely Operated Vehicle in operations (B3D, 2013)

Radio Frequency Identification System Van Oord is currently working on the implementation of a Radio Frequency IDentification (RFID) system. The idea is to implement a RFID-chip in every 17 meter chain string and Dominator connection link. During launching or recovery of the FFP, a registration unit on the bucket winch will scan the RFID-chips. The onboard computer system will then know exactly what FFP section has been where, for how long and under what conditions. The function of the RFID-chips is purely for identification, but it can be coupled to other measurement

data through the onboard computer system. A graphical illustration of the proposed RFID-system is shown in Figure 2.8. This is further discussed in Section 4.5.2.

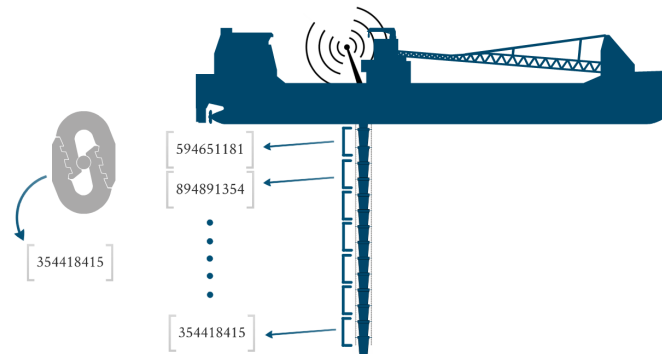


FIGURE 2.8: Graphical illustration of the proposed RFID-system onboard the FFPV

2.1.2 Flexible Fall Pipe Incidents

Over the last couple of years there have been several incidents with the Flexible Fall Pipe of both the Nordnes and the Stornes. This section will discuss the incidents that have occurred and the measures that have been taken.

Dominator Failure On several occasions during Subsea Rock Installation operations on the Nordnes over the last years, there have been failures of the Dominator connection links. Luckily, in every instance, the Dominator connection link only failed on one side of the chain strings and it was detected quickly by the load measurement system. This enabled the crew to recover the FFP on the remaining FFP chain string before the second string would break off. From the investigations following the Dominator failures it was learned that the Dominators failed due to fatigue. The following measures were taken: Dominator connection links are to be kept in pairs and the replacement period is shortened to 3 months. Fatigue testing was initiated to gain more insight into the fatigue life of the Dominator links. The information regarding the failure of the Dominator connection links has been obtained from Van Oord (2008).

Failure of the Flexible Fall Pipe Chains On 14 October 2012 at 15.07 hours, while working on the Ormen Lange Project for Norske Shell, the two chains at the top of the FFP system of the Stornes failed. This resulted in approximately 850 meters of the FFP string including rocks landing on top of the ROV. The ROV and the failed FFP were at that point suspended from the three umbilical wires at approximately 5 meters above the seabed. Operations were stopped immediately and the Captain, Offshore Construction Manager and Client representative discussed the best options to reduce the possible risks to vessel, crew, nearby subsea pipelines and ROV including

FFP. It was decided to stay in position and to prevent crossing any subsea pipeline or the umbilical. At 15.30 hours the Van Oord and Shell onshore representatives were informed about the situation. The management of V-Ships, Van Oord and Shell were informed at around 16.20 hours. Investigations were immediately started to identify the causes of the FFP failure and to take appropriate countermeasures to avoid failure on future works. Part of the investigations was the examination of the failed chain link that was found next to the moonpool. From the initial investigations it became clear that the bucket chain had failed as a result of fatigue. It also became clear that the replacement interval of the bucket chain assembly was insufficient. It was recommended to develop a system to determine the remaining fatigue life of the FFP chains and to review the suitability of the bucket chain system for Subsea Rock Installation in deep water. The replacement period of the entire FFP system has been shortened to three months until further insight is gained in this problem. The information regarding the FFP failure on the 14th of October 2012 and the subsequent investigations has been obtained from Van Oord (2012).

2.2 Statement of the Problem

The statement of the problem would be, in short, that it is required to (1) get a better understanding of the magnitude and configuration of the external loading conditions during the Subsea Rock Installation process and (2) to gain more insight in the fatigue behavior of the Flexible Fall Pipe chains under these conditions. A specific statement of the gap in knowledge that this thesis addresses will now be made.

Gap in the Knowledge For mooring chains, one can already find an extensive amount of information in the literature. However, mooring chain is usually dimensioned to have the majority of the loading below the endurance limit, which is necessary to guarantee a fatigue life of e.g. twenty years. The Flexible Fall Pipe chains have a fatigue life which is much shorter, and there is still a gap of knowledge in the use of chains in this fatigue range. Furthermore, the mean level of the tension in the chains is, relative to the Minimum Break Load (MBL), much higher than for mooring applications. Mooring chain extends, at maximum, a few hundred meters. The Flexible Fall Pipe chains extend up to a 1000 meters and they have to carry the other components of the system, including the rock friction. This makes the mean load in the chains relatively much higher and this is an effect that can strongly affect the fatigue life. For the fatigue under this high mean load there is still much knowledge to be gained. In addition, this thesis investigates the effects of chain link rotations in combination with friction. The

loading of the chain links other than purely axial is subject of many recent studies, as described in Section 2.3.5, which makes this study very topical.

2.3 Theoretical Framework

This section will discuss the literature that is available on the subject of fatigue in chains and by this theoretical framework, this thesis will be placed into context. Section 2.3.1 describes the methods that are available for assessing fatigue: fracture-based mechanics, strain-life approach and stress-life approach. Section 2.3.2 then gives an overview of the fatigue failure of mooring chain in particular. The effects of proof loading and the mean load on the fatigue life of chain will be discussed in Section 2.3.3 and 2.3.4. Section 2.3.5 will deal with a failure mechanism that can occur as a result of bending of the chain link in deep water mooring systems. Finally, Section 2.3.6 will evaluate the effects of low temperature on the fatigue behavior of steels.

2.3.1 Methods for Assessing Fatigue

Before going into the different methodologies for assessing fatigue, it is useful to start with a definition of the concept of fatigue. Fatigue is commonly described as the cumulative damage of a material component that is subjected to repeated loading. As described by Xiong and Shenoi (2011), there are several characteristics that are typical for fatigue failure. In case of failure due to fatigue, the failure occurs at a stress level less than the static strength of the material or structure. Furthermore, in general for plastic materials, there is no significant permanent deformation before the fatigue fracture. This makes it difficult to detect fatigue damage during inspection and maintenance procedures. A third characteristic of fatigue failure is the fracture zone which shows smooth and coarse zones. Once micro-cracks have formed at the fatigue origin, these cracks will propagate under the repeated loading; this creates a smooth zone. As the crack grows, the materials cross-section that bears the loading decreases significantly. This continues until the material ultimately cannot bear the loading anymore, and a sudden rupture takes place, leaving a coarse zone. Hence, three stages can be identified in the fatigue failure process: (1) fatigue crack formation (initiation), (2) stable fatigue crack propagation and (3) unstable fatigue crack propagation to result in a sudden breakdown (Xiong and Shenoi, 2011). In Figure 2.9, a typical fatigue fracture surface can be seen for one of the chain links used in the FFP system. Throughout the literature, three different methods for assessing fatigue are reported: fracture-based mechanics, strain-life approach and stress-life approach. The first two methods will be briefly touched upon, whereas the third method (stress-life approach) will be discussed more elaborately as this is the adopted method throughout this research.



FIGURE 2.9: Fatigue fracture surface of a chain link

2.3.1.1 Fracture Based Mechanics

The method of fracture based mechanics uses linear elastic fracture mechanics and crack growth material properties to determine the rate at which a crack propagates. This analysis can provide estimates for the remaining life of a structure that contains a crack. Fracture mechanics is based on the concept of stress intensity, K , that describes the magnitude of both the stress and strain fields around a crack. It is computed from the stress range, $\Delta\sigma$, the crack size, a , and the crack shape $f(a/b)$, which can be seen in Equation 2.1.

$$\Delta K = \Delta\sigma\sqrt{\pi a}f\left(\frac{a}{b}\right) \quad (2.1)$$

Therefore, the rate of the crack growth is determined by the loading, crack size and crack shape (Xiong and Shenoi, 2011). For the purpose of this study, to investigate fatigue failure in chains, fracture mechanics may not be the best choice as research methodology. Fracture mechanics is commonly used to assess the severity of cracks that are already present in a structure. For chain, it is difficult to detect cracks during inspection and maintenance procedures. Furthermore, for the stress-life approach (Section 2.3.1.3) there is an abundance of data available for (anchor) chain in the literature. Therefore, this study will not look further into fatigue failure by means of fracture mechanics.

2.3.1.2 Strain-life Approach

The second method for assessing fatigue is the strain-life approach. According to the strain-life approach, local stresses and strains around a stress concentration control the fatigue life. For most structures and materials, the nominal stresses remain in the elastic region, but occasional high loads and stresses can cause plastic deformations around notches. The fatigue damage is dependent on these local plastic strains (Socie and Malton, 2009). The strain life approach is often used in the case of low-cycle fatigue, whereas the stress-life approach in the following section is generally used for high-cycle

fatigue.¹ For the fatigue assessment in this study, the strain-life approach is not adopted as the first predictions show that the stresses remain in the elastic region. Also, for this study, tests have already been done in which the stresses were documented, and strains were not.

2.3.1.3 Stress-life Approach

The stress-life approach is the most commonly used method for assessing fatigue in structures. This method has its origins in the work of Wöhler in 1850, who investigated the fatigue failure of a rotating railway axle. Wöhler found that the fatigue life of a structure was strongly dependent on two parameters: the stress range to which the structure is subjected and the number of cycles. When plotted on a double logarithmic scale, Wöhler discovered that a straight line provided a very good fit with the measurement data. Several years later, A. Palmgren and A. Miner build further upon the work of Wöhler and they established the well-known Palmgren-Miner rule. According to the Palmgren-Miner rule, every stress cycle causes a small amount of damage to the system. This is further explained in the next paragraph.

Cyclic Stress and S-N Curve In general, cyclic stress is assumed to vary in a sinusoidal form, which can be seen in Figure 2.10. The highest maximum stress is denoted by σ_{max} and the minimum stress is denoted by σ_{min} . The mean of the maximum and minimum stresses is defined as the mean stress σ_m :

$$\sigma_m = \frac{\sigma_{max} + \sigma_{min}}{2} \quad (2.2)$$

The stress amplitude is defined as:

$$\sigma_a = \frac{\sigma_{max} - \sigma_{min}}{2} \quad (2.3)$$

This is graphically shown in Figure 2.10. The most destructive type of cyclic loading is when the mean load is positive (tensile). To account for the mean stress and the type of loading, the stress ratio parameter R is introduced, which is shown in Equation 2.4.

$$R = \frac{\sigma_{min}}{\sigma_{max}} \quad (2.4)$$

Under the cyclic loading, the resistance of the material is usually represented using a S-N curve and a fatigue limit. The most common representation for the S-N curve is by means of Equation 2.5. In Equation 2.5, m denotes the slope of the line on a double

¹The transition between low-cycle and high-cycle fatigue differs somewhat throughout the literature, but usually lies somewhere between 10^4 and 10^5 number of cycles to failure.

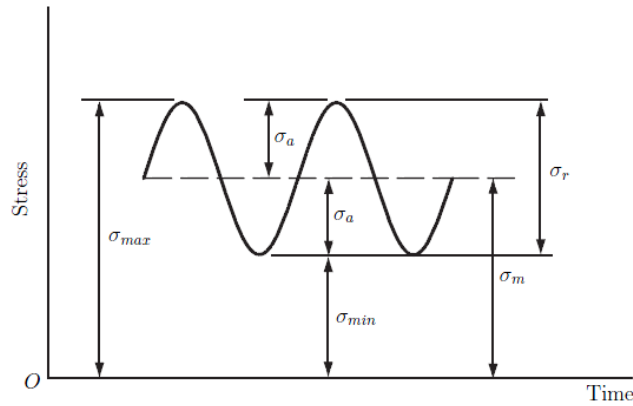


FIGURE 2.10: Definition of cyclic stress (Marghitu, 2001)

logarithmic scale, N is the number of cycles to failure, σ_a is the stress amplitude and K is usually referred to as the intercept parameter (Xiong and Shenoi, 2011).

$$\sigma_a^m N = K \quad (2.5)$$

Equation 2.5 can be adjusted for local stress hot spots, which can arise due to geometry or material imperfections. To account for a local stress hot spot, σ_a is corrected with the stress concentration factor as shown in Equation 2.6.

$$\text{SCF} = \frac{\sigma_{peak}}{\sigma_{nom}} \quad (2.6)$$

In Equation 2.6, σ_{peak} denotes the peak stress at the stress hot spot location, and σ_{nom} denotes the nominal stress. Figure 2.11 depicts the fatigue curve from Equation 2.5 and the fatigue limit. The fatigue limit describes the endurance limit stress below which the material has infinite life. The Palmgren-Miner rule states that every stress cycle above the endurance limit stress σ_e accounts for a part of the total damage. For example, at

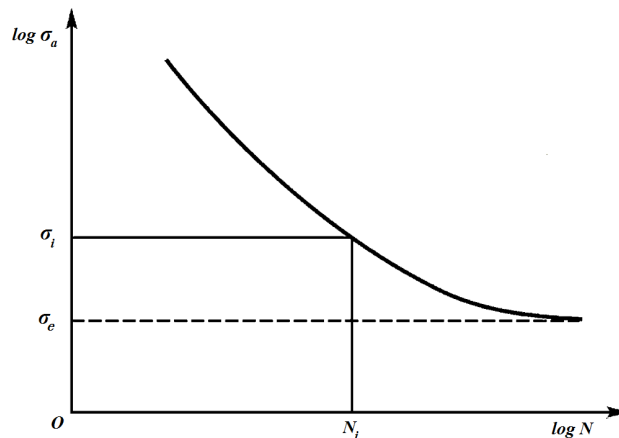


FIGURE 2.11: S-N curve (Xiong and Shenoi, 2011)

a stress range of 250 N mm^{-2} , the material component will last for 70,000 cycles. The damage of one stress cycle of that particular magnitude is then $\frac{1}{70,000}$. By summing up all the damage from the different stress cycles, one obtains the cumulative damage factor. The method for obtaining the cumulative fatigue damage factor is shown by Equation 2.7.

$$D = \sum_{i=1}^k \frac{n_i}{N_i} \quad (2.7)$$

In Equation 2.7, n_i is the number of cycles within a stress range interval i ; N_i is the number of cycles to failure corresponding to the stress range σ_i as given by the S-N curve from Equation 2.5. According to the theory, the component fails when the cumulative fatigue damage factor equals 1.

Rainflow Counting Algorithm For many of the systems that are subjected to cyclic loading, the stress pattern is not as steady as depicted in Figure 2.10. The measured stress pattern is usually erratic, with varying amplitudes and cycles which sometimes cannot easily be identified. To distill the stress cycles, which can be used in conjunction with the Palmgren-Miner rule (Equation 2.7), the rainflow counting algorithm is usually applied. For the rainflow counting algorithm the stress-time plot is turned 90° on its side, with every peak representing a pagoda style roof (Figure 2.12). Rain is then imagined to fall on these pagoda roofs and this is used to determine the number of half-cycles by looking for terminations in the flow. These terminations take place when the end of the time history is reached, when the flow merges with a flow that started from an earlier peak or when it flows opposite a peak of greater magnitude. This creates a series of half-cycles and stress ranges which can be used in conjunction with equations 2.5 and 2.7 (Matsuishi and Endo, 1968).

2.3.2 Fatigue Life of Mooring Chain

For mooring chain, there is an extensive body of literature available that reports about the fatigue properties of anchor lines when subjected to cyclic loading. For floating structures, which are stationary moored by anchor lines for years, the estimation of the fatigue life of the anchor lines is very important. On this subject, Rossi (2005) proved to be an interesting source of information. Rossi (2005) gives an overview of the fatigue curves for chain mooring lines with the information based on recent tests, rules and published papers. This data is presented on a double logarithmic scale in which a least squares or maximum likelihood straight line is fitted to obtain a mean fatigue curve. For every line, the slope m and the intercept parameter K are given. In Figure 2.13, the best-fit lines from Rossi (2005) are plotted. It should be noted that the data which is not relevant for this thesis has been omitted (e.g. the results from the special chain type

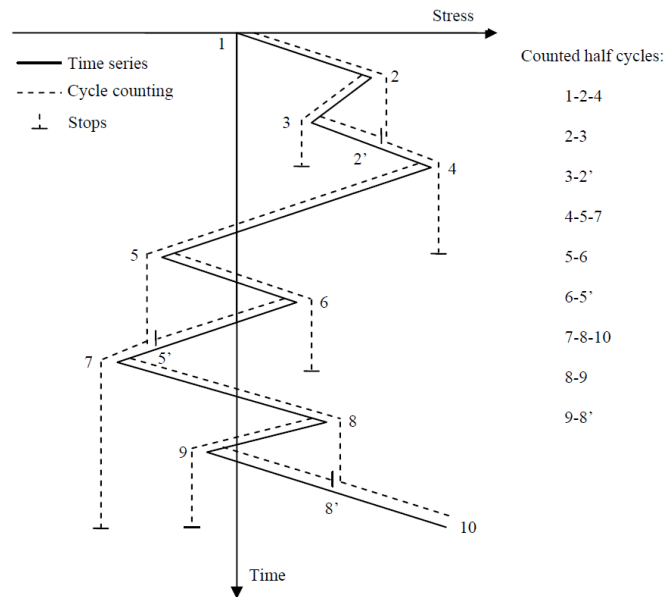


FIGURE 2.12: Rainflow counting algorithm (Marghitu, 2001)

and non-chain mooring line). The graphical representation in Figure 2.13 is slightly different as compared to Figure 2.11, as the tension *range* is plotted here instead of the stress *amplitude*. The range of tension is plotted as a percentage of the Minimum Breaking Load (MBL) on the vertical axis, which makes it possible to compare data from different tests with different chain sizes. It is interesting to see from Figure 2.13 that when normalized, indeed the different chains exhibit a similar failure pattern. When a fatigue curve has been established for the chain that is subject of this study, it would be interesting to see how it relates to the findings from Rossi (2005).

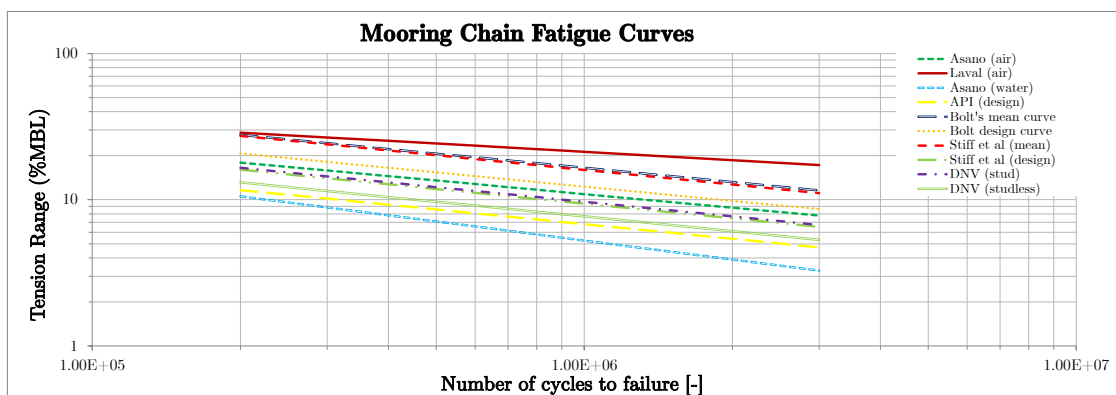


FIGURE 2.13: Fatigue curves for mooring chain (Rossi, 2005)

2.3.3 Effect of Proof Loading on the Fatigue Life of Chain

Proof loading is a step in the chain manufacturing process by which the chain is axially loaded to a certain percentage of its break load, in which the chain deformations often

reach into the plastic region. The reasons for proof loading a chain are: (1) to test if the chain can withstand the proof load, (2) to make sure the chain falls into the tolerance limits for its dimensions and (3) to extend the fatigue life of the chain. One of the first to have reported about the effect of proof loading on the fatigue life was Celander and Strom-Ljusne (1972). It was put forward that when the chain link is unloaded after the proof load, residual stresses exist in the chain link. These residual stresses act in a favourable way as a repeated load must first overcome these residual stresses. The line of reasoning as presented in Celander and Strom-Ljusne (1972) is supported by more recent literature, e.g. in Shoup et al. (1992).

2.3.4 Effect of Mean Load on the Fatigue Life of Chain

Beside the magnitude of the stress range and the number of repetitions, also the mean load has effect on the fatigue life of chain. For a positive R value, which implies tension-tension loading, the increase of the mean stress σ_m will lead to a decrease of the endurance limit stress σ_e (Gudehus, 1999). The S-N curve will thus shift downwards for increasing mean stress. To take the mean stress effect into account for the endurance limit stress σ_e , there are several methods available: Goodman, Soberberg and Gerber correction. For clarity, the following equations enable one to correct the endurance limit stress for the mean stress. The Goodman equation is shown in Equation 2.8.

$$\frac{\sigma_a}{\sigma_e} + \frac{\sigma_{mean}}{\sigma_{break}} = 1 \quad (2.8)$$

The ultimate tensile strength of the material is denoted by σ_{break} . Equation 2.8 is adopted for brittle materials while being conservative for ductile materials. The Gerber parabolic equation is usually applied for ductile materials and is shown by Equation 2.9.

$$\frac{\sigma_a}{\sigma_e} + \left(\frac{\sigma_{mean}}{\sigma_{yield}} \right)^2 = 1 \quad (2.9)$$

In Equation 2.9, σ_{yield} denotes the tensile yield stress of the material. The Soderberg equation is most conservative and shown by Equation 2.10.

$$\frac{\sigma_a}{\sigma_e} + \frac{\sigma_{mean}}{\sigma_{yield}} = 1 \quad (2.10)$$

Equations 2.8 to 2.10 are depicted in Figure 2.14. In Figure 2.14, the horizontal axis shows the mean stress, and by means of the Goodman, Gerber or Soderberg line one can read off the endurance limit stress on the vertical axis. Most of the experimental data falls between the Goodman and Gerber equation.

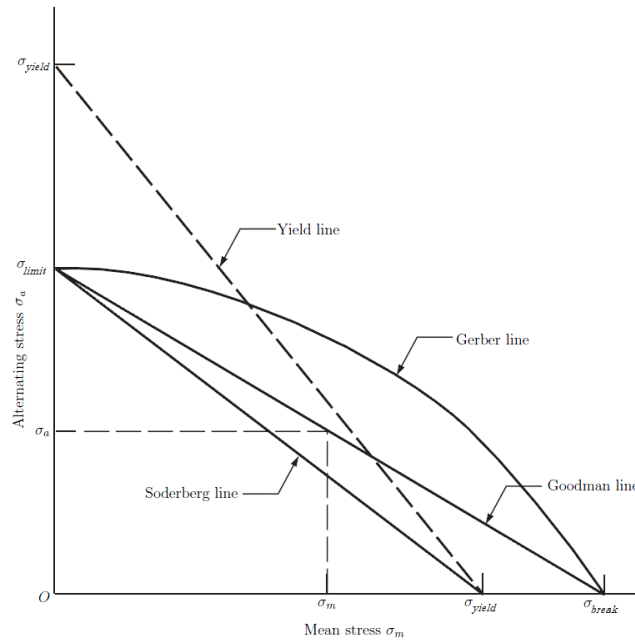


FIGURE 2.14: Constant life curve (Marghitu, 2001)

2.3.5 Failure of Chains by Out-of-Plane Bending

There are situations in which a chain can be subjected to a combination of tension and an out-of-plane bending moment, which can have severe effects in terms of the fatigue life. This combination of tension and bending can occur when the chain runs over a fairlead or winch, such as the one used for the FFP system on page 4. The out-of-plane bending moment is the result from the local geometry of the contact between the chain link and gypsy wheel bearing surfaces (Noble Denton, 2006). The effect is enhanced where the change of angle is greater, for a five pocket as opposed to a seven or a nine pocket fairlead. Also the 'twist' or out of flatness in the unstressed link is of significance. The effect of the higher stresses in the fairlead is taken into account by means of the stress concentration factor SCF, as indicated with Equation 2.6. For chain links that are frequently located on a chain wheel (fairlead) with seven pockets, Det Norske Veritas (2010) prescribes a SCF of 1.15 due to out-of-plane bending. It should be noted that the nominal stress σ_{nom} in Det Norske Veritas (2010) is obtained by dividing the tension T by cross sectional area of the chain A , which is equal to $2 \cdot \frac{\pi}{4} D^2$. In other literature, such as Gudehus (1999), the nominal stress is equal to the stress due to the tension and the bending moment, which is the result of the eccentricity of the applied tension. Besides fairleads, there have been recent reports about the failure due to out-of-plane bending in mooring chain used on a off-loading buoy (Vargas and Jean, 2005). When the interlink rotations are combined with significant chain tensions, this can cause bending stresses in the chain links. In Melis et al. (2005), testing results are presented that show that stresses due to

bending in chain links can be a significant source of fatigue damage. The results show that the out-of-plane stresses are a function of the applied chain tension. The higher the tension the higher the out-of-plane bending stresses. Further, the out-of-plane bending stresses are a function of interlink rotation, the higher the interlink rotation, the higher the out-of-plane bending stresses. The significance of the effect of local chain bending on fatigue is further corroborated by van der Cammen et al. (2007). In Lassen et al. (2009), the behavior of chain segments subjected to pretension and a rotation angle at the segment end was investigated both experimentally and by numerical modeling. It was concluded that the out-of-plane bending stresses are significant for critical links close to the hang-off area in moored floaters. The effect must be taken into account when carrying out fatigue life predictions, and it is suggested that a stress hot spot method be applied.

2.3.6 Low Temperature Fatigue Behavior of Steels

Van Oord will most likely be performing SRI operations in conditions that qualify as Arctic, i.e. conditions with low temperatures and the presence of snow and ice onboard of the vessel. Therefore, it is important to quantify the effects of low temperature on the fatigue behavior of the chain. An extensive literature study on the fatigue and fracture toughness of cast steels at low temperature was performed by Stephen (1982). The authors carried out a literature review to investigate the low temperature fatigue behavior in steels for constant amplitude loading. In this review, a distinction was made between high cycle and low cycle fatigue, and notched and unnotched samples.² The general conclusions for low temperature fatigue behavior in steels are that unnotched high-cycle fatigue strengths have consistently increased at low temperatures. Increases may be small such as a few percent or can be substantial such as several hundred percent. The increased fatigue life can be attributed to the tensile strength and yield strength which generally increases at lower temperatures. Notched high-cycle fatigue strengths have substantially smaller increases at low temperature and in some cases small decreases were found. For low-cycle low temperature fatigue the unnotched and notched resistance can be increased, decreased or have little change. At low-cycle low temperature fatigue the effect of the reduced fracture toughness and reduced ductility plays a larger role, which explains the difference with high-cycle low temperature fatigue behavior. As the fracture toughness is reduced at lower temperatures, the critical crack lengths can be substantially reduced which can reduce total fatigue life. As the studies have been performed at constant amplitude loading, the low temperature fatigue behavior of steels

²It is assumed that the chain links used for the Subsea Rock Installation process operate in the high cycle fatigue range.

in real-life variable amplitude loading needs further investigation. An example of the difference between constant and variable amplitude loading is that residual stresses formed prior to or during real-life loading can alter both crack initiation and propagation at low temperatures. It was recommended in this study that further research examines the effect of low temperature on the fatigue life under variable amplitude loading (Stephen, 1982).

2.4 Significance of the Study

The Subsea Rock Installation that Van Oord is executing requires the precise placement of millions of tonnes of rock in water depths approaching 1,000 meters. The expenditures for these projects are high and make downtime as a result of chain fatigue failure very costly. The implications of such incidents could clearly be seen on the 14th of October 2012, when both FFP chains on the Stornes failed and the FFP fell down on the ROV. To give an indication, if one looks at the dayrates for the FFP vessels, these already go towards the 0.1 million euro a day. Secondly, the ROV at the bottom of the FFP is highly specialized and has a long lead time, which makes it expensive and valuable equipment to lose. And then there are the safety implications when the chain 'snaps', as the upper part of the FFP system can become a deadly projectile to the workers in the moonpool area. As the implications of chain fatigue failure are very undesirable, one could say it would be much easier to just be highly conservative and consequently replace the chain more regularly. The difficulty is that the chain has a substantial lead time and the downtime involved in constantly replacing the chain is undesirable. Another solution to this problem would be to increase the size of the chain, however this requires the change of the entire onboard system to the new size. More importantly, the system becomes heavier as the chain size increases, which makes it less suitable for deep water. This demonstrates that the easy options to this problem are not satisfactory and a more in-depth study into the fatigue failure of the chains is necessary, especially for the deeper water projects in the near future. This short analysis already shows the significance of this study for this particular application. However, also in a more general sense this study is of significance. In the entire maritime industry, chain is widely applied in terms of mooring of floating structures. At a lifetime of 20 years and an average wave period of 9 seconds, mooring lines are subjected to $70 \cdot 10^6$ cycles, which makes fatigue an important design criteria. As indicated in Section 2.3, there is a substantial amount of research on the topic of chain fatigue. Furthermore, a Joint Industry Project (JIP) was launched in 2006, with the main objective to improve the integrity of the mooring systems on Floating Production Systems (FPSs) (Noble Denton, 2006). Two

recommendations from this study that are particularly interesting in view of this thesis are:

1. To evaluate bending and tension-bending fatigue in chains and also to measure how chain surface finish can affect the friction between links.
2. To better understand tension-tension fatigue for chains, currently given by T-N curves, derived from full scale tests made in the late 1990's. The hot-spot S-N approach, i.e. stresses by Finite Element Analysis, derived from tests on small scale specimen could be fruitfully used.

The overlap between the recommendations from Noble Denton (2006) and the scope of this thesis clearly indicates that the findings from this thesis are also significant to applications other than Van Oord's Subsea Rock Installation. To sum up, the addition from this thesis to the existing body of literature comes from the further insights into the aspects of chain fatigue failure. These aspects consist of a particular focus on the high mean stress and the effects of the interlink rotations under the influence of friction. Additionally, fatigue curves for this application are derived analytically and compared to measurement data. The design process for the analytical derivation of fatigue curves could also be applied in the design of future deepwater mooring projects. To conclude, as a result of this thesis, the public gains a better understanding of the process of fatigue failure for chains, which will ultimately lead to better and safer designs in the maritime industry.

Chapter 3

Methodology

This chapter starts with a short recap of the objective of this study in Section 3.1. The research approach will then be discussed in Section 3.2. In Section 3.3, the research procedure will be dealt with, which involves a description of the numerical and theoretical models that will be used and the experiments that will be undertaken. The data processing and analysis is discussed in Section 3.4.

3.1 Objective of the Study

To restate once again, the two main goals of this research are (1) to find out what the magnitude and configuration is of the external loading conditions during the Subsea Rock Installation process and (2) to gain more insight in the fatigue behavior of the Flexible Fall Pipe chains under these conditions. From thereon, it will be possible to make predictions regarding the fatigue life of the chains, their replacement frequency and what measures could be undertaken to improve this system.

3.2 Research Approach

To reach the goals of this study, this thesis will use a combination of numerical modeling, theoretical modeling and experiments. OrcaFlex, a marine dynamics program, will be used to evaluate and quantify the global loading conditions that are present in the FFP system during the SRI process. On a local scale, by means of a Finite Element Model in Ansys, the actual chain links are studied when subjected to the different loading situations from OrcaFlex. Further, through an analytical design process, the fatigue curves of the chains will be established under various conditions. These fatigue curves will be compared to real-life fatigue testing data which is obtained from fatigue experiments at TNO.

3.3 Procedure

This section will describe the procedure by which the global loading conditions on the Flexible Fall Pipe and the fatigue behavior of the chain will be analysed. Section 3.3.1 will describe how the FFP system is modeled in OrcaFlex and what loading scenarios will be reviewed. In Section 3.3.2 the Finite Element Model of the chain link and the corresponding loading conditions will be dealt with. Section 3.3.3 discusses the fatigue testing setup at TNO and it will give an overview of the proposed fatigue testing specifications. The analytical derivation of the fatigue curve will be shortly described in Section 3.3.4. A more elaborate explanation of this method can be found in Chapter 4: Results.

3.3.1 OrcaFlex Numerical Model

The modeling of the FFP system in OrcaFlex will be described in this section: first the modeling of the vessel is described, then the modeling of the Flexible Fall Pipe system is discussed and finally an overview of the loading scenarios is given. The theory behind OrcaFlex is assumed to be known by the reader. If not, the reader is referred to Appendix C, Section C.1 for background information.

3.3.1.1 Modeling of the Vessel

The Stornes is Van Oord's latest and most sophisticated FFP vessel, and the Stornes will take the lead when Van Oord moves into deeper water and harsher conditions. Therefore, in the modeling process, the main focus will lie on the FFP vessel Stornes. In OrcaFlex, the properties of the Stornes are specified: the dimensions, weight, centre of gravity, moments of inertia and Response Amplitude Operators (RAOs). The values of these properties and further information can be found in Appendix A, Table A.1. It is also possible to specify the Load RAOs, the Wave Drift and Sum Frequency Quadratic Transfer Functions and other properties. However, as the vessel is on Dynamic Positioning during the SRI process these properties are omitted from the model.

Response Amplitude Operators As the RAOs of the Stornes were not available from measurements, simulations were performed to obtain them for a similar bulk carrier in the program 'Octopus'. Response Amplitude Operators are difficult, abstract concepts that are quite prone to errors. However, there are some quality checks which you can perform to check whether or not the general outcome is correct. The most easy way is to check the response of the vessel at very short and very long wave periods. For very short wave periods, the response is suppressed by the vessel's inertia, so the displacement

RAOs should be zero for all degrees of freedom. In very long waves, the vessel will move like a raft on the water surface (Orcina, 2012). These two quality checks and other limit scenarios have been evaluated for the vessel's RAOs and the motions were indeed inline with the expectations. OrcaFlex makes it easy to check this, as it enables plotting the complex amplitude and phase diagrams for the RAOs, for all six degrees of freedom with the limiting cases indicated.

Moonpool Area The moonpool area of the Stornes is represented by a block-shaped space of the type 'Trapped Water' at the center of the vessel. Inside the trapped water shape, the fluid motion is modified, as the trapped water moves and rotates with the vessel. The surface elevation in the moonpool does respond to the wave outside, but it is attenuated to some extent and lags behind the surface outside (Orcina, 2012). As the FFP system is launched and fully extended, a special frame (Figure 3.1) will be lowered to the bottom of the moonpool area: the Umbilical Moonpool Frame (UMF). The FFP system runs through the UMF and is represented in OrcaFlex by a shape of the type 'Elastic Solid' (Figure 3.2).

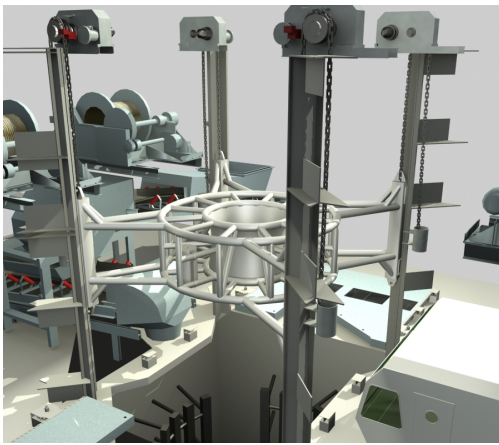


FIGURE 3.1: Graphical representation of the Umbilical Moonpool Frame

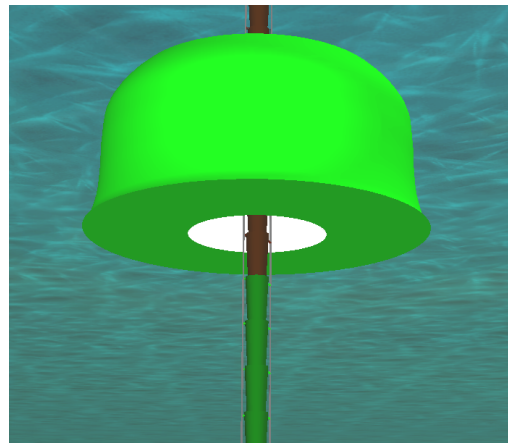


FIGURE 3.2: Umbilical Moonpool Frame modeled in OrcaFlex

3.3.1.2 Modeling of the Flexible Fall Pipe System

The two chains that support the entire FFP system, are represented in OrcaFlex by two lines. The properties of the chain have been obtained from the chain manufacturer, RUD Ketten, and from the OrcaFlex database. As the vessel moves, the chain lines move with it, as the top ends are connected to the vessel. The bottom end of the chain lines is left free. The buckets and telescopic pipe are modeled as follows:

- **Top section** The top section with the first twenty buckets is modeled by means of 3D buoys. The 3D buoys are given the same properties as the buckets in terms of weight, drag and added mass. Every bucket is connected to the lines by means of two highly stiff tethers, which represent the bucket attachments. There is a node in the top section of the line for every bucket, as this section needs to be modeled with higher accuracy as it might come in contact with the Umbilical Moonpool Frame.
- **Middle section** For the middle section of the chain, there is a node every ten buckets. The ten buckets are represented by clump weights which are attached to the line and have properties in terms of weight, drag and added mass.
- **Bottom section** The last section of the lines has a clump weight that represents the telescopic pipe and has corresponding properties. The telescopic pipe consists of three pipes, and it is assumed that two pipes are suspended from the FFP whereas the third is supported by the ROV and the Umbilical Wires.

Umbilical Wires In reality, the Umbilical Wires are connected to the FFP chains every five buckets to keep the entire system together, but they do not 'carry' the chain. Therefore, for the level of tension in the chains, it is not necessary to model the Umbilical Wires. However, it *is* necessary to model the Umbilical Wires when one would look at the contact forces between the FFP and the Umbilical Moonpool Frame. As there is a 15 tonne ROV hanging from the Umbilical Wires, in addition to the self weight of the Umbilical Wires of 6.2 tonnes/km, this largely affects the configuration of the FFP and therefore the contact forces at the Umbilical Moonpool Frame. Now, if one would connect the Umbilical Wires to the chains in the OrcaFlex model, the model quickly becomes quite complex and difficult to solve. OrcaFlex can solve lines separately or when they are connected at the end points. However, when two lines are connected to each other at multiple points along the line, OrcaFlex cannot solve for the two lines at the same time. The only way to solve lines that are connected at multiple points is to manually specify the initial conditions accurately enough for OrcaFlex to find a solution that suffices for both lines separately. Therefore, it was decided to adopt the following modeling strategy: the Umbilical Wires and the ROV will only be modeled for loading scenarios in which the contact forces in the Umbilical Moonpool Frame are investigated. For those specific cases, the Umbilical Wires are connected to the FFP chains at a number of points along the lines.

Subsea Rock Installation The friction of the rocks that travel down the FFP system can be incorporated in the model by two ways: either by increasing the weight of the

chain links or by letting a content flow through the lines. Both situations will be reviewed and discussed.

3.3.1.3 OrcaFlex Loading Scenarios

In the numerical model which was created in OrcaFlex, different loading scenarios will be reviewed in terms of water depths, wave height and period, current speed and distribution, rock dumping rate, vessel speed and vessel loading conditions. The characteristics of the Ormen Lange field, which is used as the base case scenario, is shown in Table 3.1. This base case scenario has been established based on the information from Appendix B.

TABLE 3.1: Ormen Lange base case loading scenario

Design parameter	Value	Design parameter	Value
Water depth	900 m	Current speed seabed	0 m s ⁻¹
Significant wave height	2 m	Current direction	180°
Wave period	6 s	Current distribution	Power law
Wave type	JONSWAP	Current exponent	7
Wave direction	180°	Rock dumping rate	0 tonne h ⁻¹
Current speed surface	0.2 m s ⁻¹	Simulation time	3600 s

From this base case scenario, other loading scenarios will be investigated by changing one or more design parameters. The following loading scenarios will be looked at:

General Loading Scenarios The first 36 loading scenarios are generated by investigating the water depths of 800, 1000, 1200 and 1400 meter for significant wave heights of 2, 4 and 6 meters and current speeds of 0, 0.2 and 0.4 meters per second. These scenarios are the centre of this research and will be used for the chain fatigue predictions when performing SRI operations in deeper waters.

Extreme Current Scenarios Three extreme case current distributions will be examined, of which a graphical overview can be found in Appendix B. These extreme case current distributions have been obtained from extensive field measurements by Shell at the Ormen Lange Field and they have a return period of one year. As these scenarios are designed to evaluate the magnitude of the contact forces between FFP and the Umbilical Moonpool Frame, the Umbilical Wires will be modeled for these scenarios.

Directional Current Profiles Scenarios Three directional current profiles will be investigated in which the current approaches from 0, 90 and 180 degrees with respect to the moving vessel. During the SRI operations, the FFP vessel moves at a slow and constant speed of about 15 cm per second. The associated drag on the FFP can push

the system against the Umbilical Moonpool Frame. It is likely that the direction of the current with respect to the vessel will have an additional effect on the contact forces between FFP and Umbilical Moonpool Frame, depending on its direction. Again, this scenario includes the modeling of the Umbilical Wires.

Subsea Rock Installation Scenarios Twelve scenarios are performed to examine the effect of rock friction on the dynamic behavior of the chain. In three simulations a content flows through the line that represents the chain. This content is equivalent to a dumping rate of 500, 1000 and 1500 tonnes of rock per hour, which will be determined from logdata analysis. In three other simulations, the line weight is increased in accordance with the same dumping rates of 500, 1000, and 1500 tonnes of rock per hour. These six simulations will be run at a significant wave height of 2 meters and 4 meters, which makes a total of twelve simulations. The idea of these simulations is to look at the difference between flowing content and increased self weight. If the difference is only slightly, the SRI process can be modeled by increasing the level of tension in the chains in accordance with the dumping rate. This makes it much easier to look at a large range of rock dumping rates without having to run all these simulations through OrcaFlex.

Deepwater Buckets Scenarios Van Oord is currently looking into using specialized deepwater buckets for Subsea Rock Installation in water depths of more than 1000 meters. These specialized buckets have a buoyancy capacity of 28 kilogram. The idea is that these buckets reduce the mean tension in the chain by lifting the chain up, which will have a positive effect on the fatigue life of the chain. Four scenarios are examined in terms of fatigue: a water depth of 1300 meters for a significant wave height of 2 and 4 meter with deepwater buckets, and the same two scenarios with normal buckets. Additionally, four scenarios are run to identify the contact forces between FFP and Umbilical Moonpool Frame for normal and deepwater buckets, with and without Subsea Rock Installation. These last four scenarios again involve the modeling of the Umbilical Wires and ROV.

Vessel Loading Condition The Stornes will respond differently to the waves depending on the amount of cargo that it contains. In the base case scenario, the Stornes is loaded for 25%. This scenario will look at the vessel's response when it is loaded with rocks to its full capacity of 100%.

3.3.2 Finite Element Model of the Chain Link

To get a better understanding of the fatigue behavior of the chain links, a Finite Element Analysis (FEA) will be performed in ANSYS. This FE-model will give more insights into

the locations and magnitudes of the peak stresses and the stress distribution throughout the chain link. This section will describe step-by-step how this model is generated and what conditions will be reviewed.

3.3.2.1 Creating the Finite Element Model

For this analysis 3D structural solid elements of the type Solid186 will be used. Solid186 is a higher order 3D 20-node solid element that exhibits quadratic displacement behavior (see Figure 3.3). The element is defined by 20 nodes having three degrees of freedom per node: translations in the nodal x, y and z direction (Ansys, 2007). The material properties of the solid elements are set to those of steel with a Young's Modulus of 210 GPa and a Poisson ratio of 0.3. The full chain link is build up from four

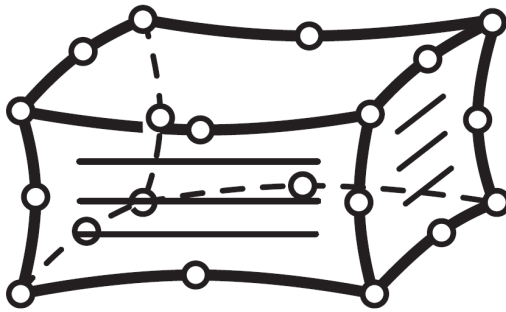


FIGURE 3.3: Representation of the Solid186-element with 20 nodes (Ansys, 2007)

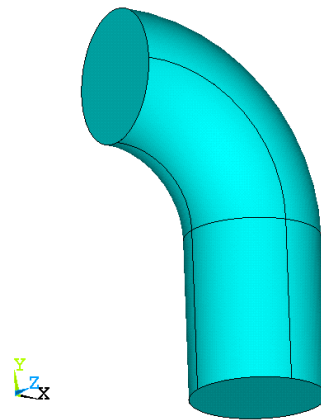


FIGURE 3.4: Quarter of a chain link in ANSYS

identical volumes that each consist of a cylinder and a quarter of torus (Figure 3.4). The volumes are meshed by means of hexahedral (brick) elements. The applied loading will be transferred from one chain link to another by means of contact elements. The contact elements themselves overlay the solid elements and describe the boundary of a deformable body. These contact elements use a 'target surface' and a 'contact surface' to form a contact pair. The target surface is modeled with elements Targe170 and the contact surface is modeled with element type Conta174 (Ansys, 2009).

3.3.2.2 Finite Element Model Loading Scenarios

The different loading scenarios for the Finite Element Model in ANSYS will be discussed in this section. First, the load cases for the quarter chain link model will be described, which is then followed by an overview of the full chain link model. Finally, a description of the method for investigating chain link rotations will be given.

Quarter Chain Link Model The first scenario that will be reviewed is a quarter of the chain link which will be loaded by a force of 125 kN, while being constrained on the bottom area in the nodal x, y and z-direction. This is shown on the left side of Figure 3.5. Initially, no constraints will be applied on the top left area. This enables

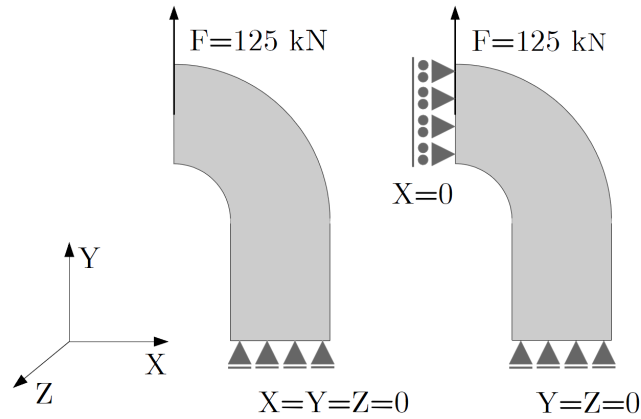


FIGURE 3.5: FEM loading scenarios for the quarter chain link: case 1 (left side) and case 2 (right side)

one to compare the stress distribution on the bottom area of the quarter chain link to the results from a (more straight forward) analytical derivation. The applied forcing of 125 kN is equivalent to a tension of 250 kN in the full chain link, which is roughly the level of tension which is found when performing SRI-operations in water depths of 900 meters. First, a variety of mesh-sizes will be investigated to identify from what level of segmentation the results no longer change significantly. Further, an additional symmetry boundary condition will be imposed on the top left area of the quarter chain link, which then basically functions as a rolling support. This is shown on the right side of Figure 3.5. As a result, an additional bending moment will be present on the top left area, making the problem statically indeterminate for the analytical derivation. However, it gives a more realistic representation of the chain links under loading in the FE-model. When the quarter chain link model gives results that are in line with the analytical derivation, the full model will be established.

Full Chain Link Model The full model consists of half a chain link, which is coupled by means of the contact elements to a full chain link, which in turn is coupled to another half chain link by means of contact elements (see Figure 3.6). The bottom areas of the lower half chain link are constrained in the nodal x and y-directions. Additionally all the nodes of the lower half chain link in the xy-plane are constrained in the z-direction. By selecting the boundary conditions in this manner, it is possible for the bottom sections of the lower half chain link to deflect in the z-direction, which is also the case in reality. The upper half chain link will be loaded in the nodal y-direction by applying an outward

pressure on both top areas that is equivalent to a force of 125 kN. Thus, the tension in the chain links is again 250 kN, which is the same as with the quarter chain link model. This first loading configuration is shown on the right side of Figure 3.6. The stress distributions in the full chain link model will be compared to the results from the quarter chain link model. Additionally, the key parameters that play a role in the contact analysis, i.e. the contact stiffness (FKN), the penetration depth (ICONT) and the pinball radius (PINB) will be evaluated. The reaction forces will be checked to see if the forces are transmitted by the contact elements correctly.

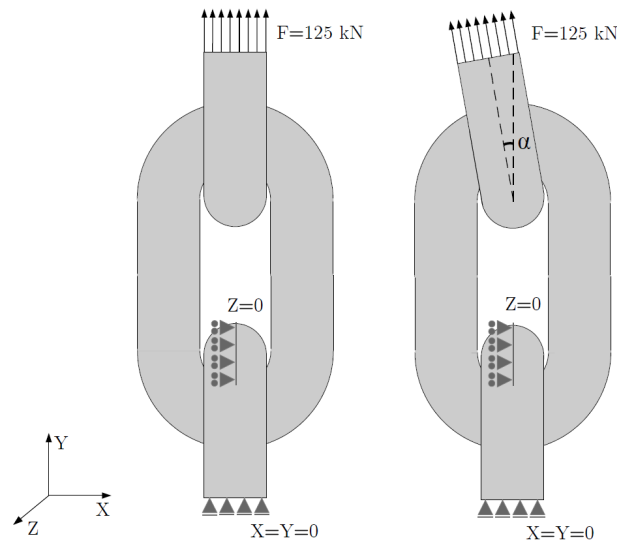


FIGURE 3.6: FEM loading scenarios for the full chain links

Chain Link Rotations When this model functions correctly, the upper half chain link will be rotated about the z-axis over an angle α to simulate the effect of rotations of the chain links with respect to one another (see right side of Figure 3.6). It is expected that chain link rotations occur when, during the SRI-operations, the current gives the FFP an offset position. From OrcaFlex it will become clear what the magnitude of these interlink rotations is. Additionally, as the chain links run over the winch and the sprocket wheels, the chain links are loaded under an angle. It is expected that these rotations will have an effect on the location and magnitudes of the peak stresses. Often, it is the same chain link that is located at this (possibly) most critical position at the winch, which makes it necessary to quantify this effect. At the winch and the sprocket wheels, a maximum interlink rotation of 6.6° is found. Therefore, chain link rotation up to 7° , in steps of 1° will be investigated, at a chain tension of 250 kN. As friction will most likely have an effect on the results, a frictional factor μ of 0.2 - 0.6 in steps of 0.1 will be looked at.

3.3.3 Fatigue Testing of the Chain Links

Fatigue testing experiments will be performed at TNO to gain more insight in the fatigue life of the chain. Three chain links will be constrained on either side in a tensile test bench as shown in Figure 3.7. Before the actual fatigue testing starts, a bag of seawater will be



FIGURE 3.7: Experimental set-up for fatigue testing at TNO

wrapped around the chain to model the conditions of use more accurately. The chemical composition of the seawater was made according to Atlantic Ocean quality. The chains will be cyclically loaded at a frequency of 1 Hertz with a constant amplitude sinusoidal load and a non-zero mean load. The exact specifications of the fatigue testing are shown in Table 3.2. As can be seen from Table 3.2, the fatigue testing has been performed at a mean load which varies between 175 and 300 kN. This mean load increases for higher amplitudes as it was tried to represent the Subsea Rock Installation process as realistic as possible. As the FFP vessels operate in deeper water, the weight, the drag and the added mass increases. As a result, not only does the mean tension level in the chain increase, also the tension amplitudes increase in deeper water. Therefore, in the testing, as the amplitude increases, so does the mean load. Furthermore, similar fatigue testing has been performed for the Dominator connection links and it was tried to reproduce these tests for the normal chain, to enable one to make a comparison.

3.3.4 Analytical Derivation of the Fatigue Curve

The fatigue life of a structure is dependent on various factors, including the stress amplitude σ_a and mean stress σ_m . Furthermore, the fatigue life is dependent on factors such as the surface roughness of the material R_z , the geometry, the size of the component

TABLE 3.2: Fatigue testing specifications

Test no.	Lower range [kN]	Upper range [kN]	Mean load [kN]	Stress range [kN]	Percentage of break-load [%]	Stress ratio R [-]
1	150	200	175	50	4.17	0.75
2	150	250	200	100	8.33	0.60
3	150	250	200	100	8.33	0.60
4	150	250	200	100	8.33	0.60
5	150	300	225	150	12.50	0.50
6	150	300	225	150	12.50	0.50
7	175	375	275	200	16.67	0.47
8	175	375	275	200	16.67	0.47
9	175	375	275	200	16.67	0.47
10	100	400	250	300	25.00	0.25
11	100	500	300	400	33.33	0.20
12	100	500	300	400	33.33	0.20
13	100	500	300	400	33.33	0.20

and the stress gradient χ^* , to name a few. In the fatigue testing from Section 3.3.3, only one mean stress was investigated, whereas in reality the chain links are subjected to a mean stress which depends on the position in the FFP, the rock dumping rate, the water depth and other influences. To investigate the effects of different factors that affect the fatigue life, without having to do real-life testing, one can analytically derive the S-N curves. In Gudehus (1999), an analytical derivation for the S-N curve is proposed. Based on experimental data, relations for the different points in the S-N curve have been established and summarized in the design process on page 90. This method takes into account the type of loading, stress concentration factors and the accompanying stress gradient, the size effect, production methods, surface roughness and mean stress. Thus, by means of this method, the fatigue curves will be constructed and different factors affecting these curves will be evaluated. The full derivation of the analytical S-N curve is discussed in Chapter 4, Section 4.4.

3.4 Data Processing and Analysis

The data processing and analysis will be performed in four software packages: OrcaFlex, Matlab, ANSYS and Excel. For the calibration of the OrcaFlex model, logdata is obtained from the vessel: a chain tension - time series and the corresponding heave - time series. The heave motions are used as input for the OrcaFlex model and the resulting tension is compared to the measured tension. This comparison is made in the time and frequency domain in Matlab. When the model operates satisfactory, OrcaFlex is then used to analyse a variety of loading scenarios in terms of water depth, wave heights, current

speeds, vessel speeds and rock dumping rates. For these scenarios, the chain tension - time series are extracted from OrcaFlex and imported in Matlab, where the rainflow counting algorithm is applied to distil tension cycles from this dataset. The rainflow counting algorithm is adopted from Nieslony (2009). The extracted tension cycles are used in conjunction with the derived fatigue curves in Matlab. In the construction of the fatigue curves and the analysis of the stress distributions, extensive use is being made of the Finite Element software package ANSYS. Finally, the report is written in L^AT_EX.

Chapter 4

Results

This chapter presents and discusses the results from the various models. In Section 4.1, the results from the various scenarios in the OrcaFlex model are presented, followed by the results from the Finite Element model of the chain link in Section 4.2. The fatigue testing results from TNO will be discussed in Section 4.3. In Section 4.4 a full description of the analytical derivation of the fatigue curve will be given. Finally, Section 4.5 couples the different models and makes predictions regarding the fatigue damage factor throughout the Flexible Fall Pipe.

4.1 OrcaFlex Results

In the following sections the results from the OrcaFlex model will be discussed. First, the calibration and validation of the model is presented, which is then followed by the results from various loading scenarios.

4.1.1 Calibration and Validation of the OrcaFlex Model

To calibrate and validate the OrcaFlex model, the following approach is adopted. During operations, the heave motions and the associated chain tension is recorded in the logdata of the FFPV. The recorded heave motion is then used as input for the motion of the vessel in OrcaFlex. The recorded chain tension from the logdata is then compared to the chain tension from the OrcaFlex model. The level of tension in both chains is recorded by the logging system and the chain with the highest level of tension is used for quantifying the model properties of the OrcaFlex model. This is done for eleven datasets which have different water depths, different wave heights and with and without Subsea Rock Installation. Figure 4.1 shows a comparison between the measured chain tension (red line) and the simulated chain tension (blue line) from OrcaFlex. To make the comparison between both datasets somewhat clear, a moving average and a moving

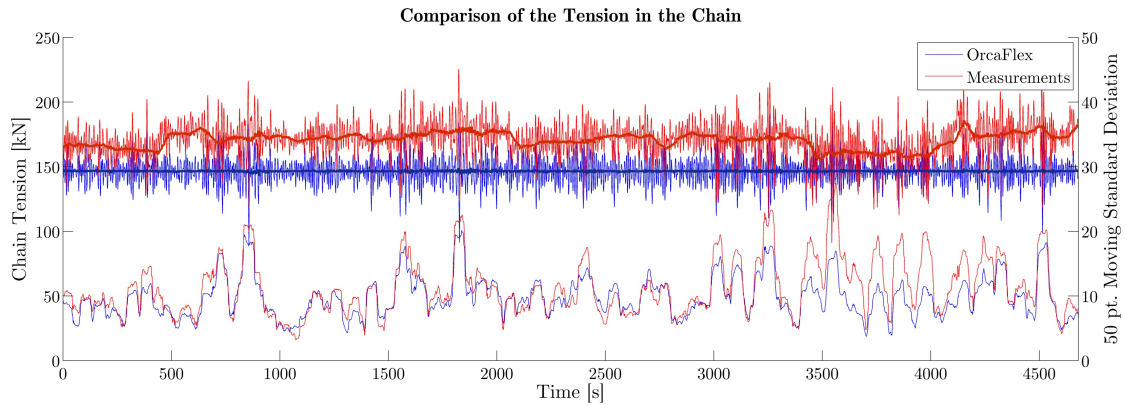


FIGURE 4.1: Comparison of the chain tension for a water depth of 515m with no rock flow

standard deviation over 50 points is plotted. All signals are plotted on the left y-axis, except for the moving standard deviation which is plotted on the right y-axis. There is an abundance of logdata available, however, the datasets have to fulfil a set of criteria to be used for comparison. These criteria require that the dataset should be long enough, heave motion and chain tension recorded simultaneously, fairly constant water depth and the start-up effects of the Subsea Rock Installation process should be faded out. As the motion sensor was faulty for a long period of time and there have been problems with the chain tension measurement frame, there is only a limited amount of data that fulfils all the requirements. For further comparison, a frequency plot of the measured and simulated signal is constructed and shown in Figure 4.2. The large peak at 0.1 Hz can be traced back to the heave period of the vessel. An overview of the comparison between the measured and simulated signals for all eleven datasets can be found in Appendix D, Figures D.1 to D.22 in both the time and frequency domain.

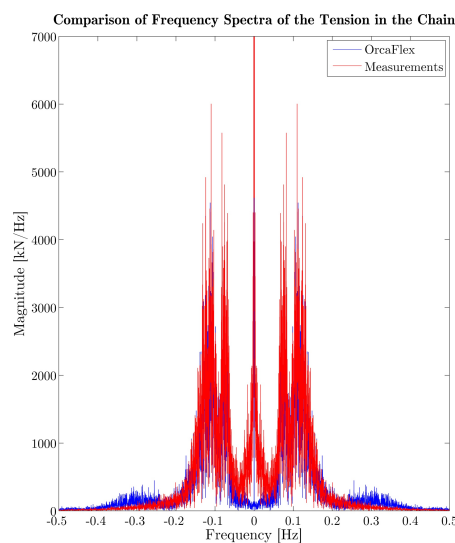


FIGURE 4.2: Frequency spectrum of the chain tension for a water depth of 515m with no rock flow

4.1.1.1 Hysteresis in the Measurement Frame

The tension in the Flexible Fall Pipe chains during the operations is measured onboard of the vessel by a measurement frame. With the help of Figure 4.3, it will become clear that the measurement system experiences hysteresis, i.e. the load path during installation of the FFP is different from the load path during the recovery of the FFP. The data in Figure 4.3 has been obtained from an operation that consisted of three stages:

1. Constant lowering velocity: Lowering of the FFP to 850 meters water depth at a constant velocity of 0.17 m s^{-1} .
2. Constant position: The FFP remains in position at 850 meters water depth for about 50 minutes, no Subsea Rock Installation takes place.
3. Constant recovery velocity: Recovering the FFP at a constant velocity of 0.17 m s^{-1} .

Figure 4.3 shows the average tension in the chains as a function of the depth of the ROV. Two distinct paths can be identified in Figure 4.3. The right path was obtained during the installation of the fallpipe, whereas the left path was obtained during the recovery of the fallpipe. The difference between both paths is about 7 tonnes, which clearly shows the presence of the hysteresis. It is unlikely that the loading difference can be attributed to the difference in streamline of the FFP during installation and recovery. The reason is that the FFP appears to be more streamlined in the downward direction (during installation), but it was during installation that the right path in Figure 4.3 was obtained. Furthermore, this hysteretic behaviour has been investigated during docking of the FFP vessel. In the investigation, a large bag was hung from the measurement frame and slowly filled with water, until a total weight of several tonnes was attained. Then, by releasing a plug in the water bag, it was slowly emptied. During these investigations, the same hysteric behaviour was found as during the installation and recovery procedures on board the FFP vessel. As for the amplitude characteristics in Figure 4.3, both paths are very similar. There may be large deviations at the bottom of the graph, but this is to be expected as there are simply more datapoints there from stage 2 of Figure 4.3. It can be concluded from these findings that the hysteresis in the measurement frame is of such magnitude that the mean axial chain load is unreliable. As the weights of all the FFP components are known, more accurate results will be obtained by the addition of the weights of the separate components of the FFP. Therefore, in the calibration procedures, the focus lies on the cyclic behavior of the chain tension.

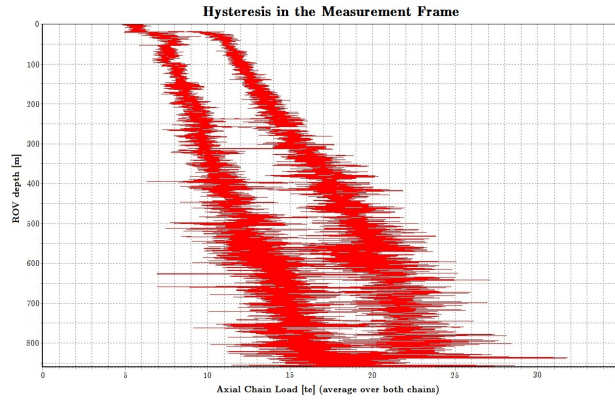


FIGURE 4.3: Hysteresis in the measurement frame

4.1.1.2 Effect of Rock Friction on the Chain Tension

As the rocks travel down the Flexible Fall Pipe during the Subsea Rock Installation process, the friction of the rocks on the inside of the buckets causes the chain tension to increase. Figure 4.4 shows in blue the chain tension (left vertical axis) as a function of time, as recorded on the FFPV. The cyclic behavior can be traced back to the motions of the vessel, whereas the increase in tension at $t=68150$ seconds is due to the rocks that

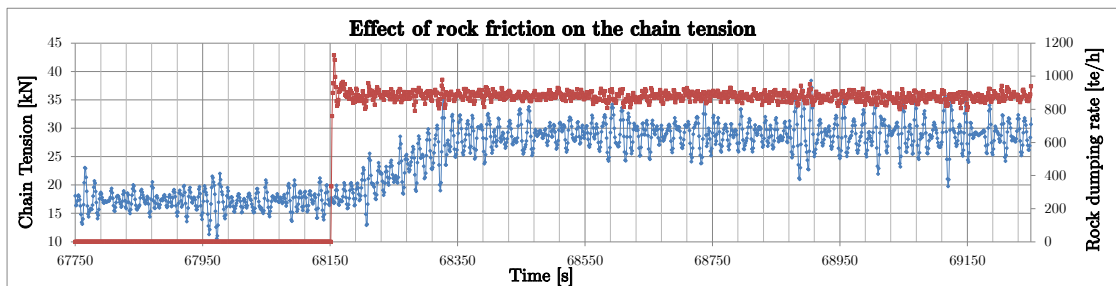


FIGURE 4.4: Effect of rock friction on the level of tension in the chain

start to fall down the Flexible Fall Pipe. The rock dumping rate is shown in red and plotted on the right vertical axis. As the working depth and the rock dumping rate is recorded, it is possible to quantify the amount of friction that is generated by the rocks by looking at the difference in chain tension. Figure 4.5 shows the result of this analysis: on the vertical axis the generated friction is plotted in N m^{-1} and on the horizontal axis the rock dumping rate in tonnes h^{-1} . The datapoints from Figure 4.5 have obtained from various water depths and a second order polynomial best-fit line has been plotted through the datapoints. In the loading scenarios that follow in Section 4.1.2, this best-fit line is used in quantifying the amount of friction generated by the rocks. The rock travelling velocity has been set to 5 m s^{-1} , as it takes roughly 180 seconds for the rocks to reach a depth of 900 meters.

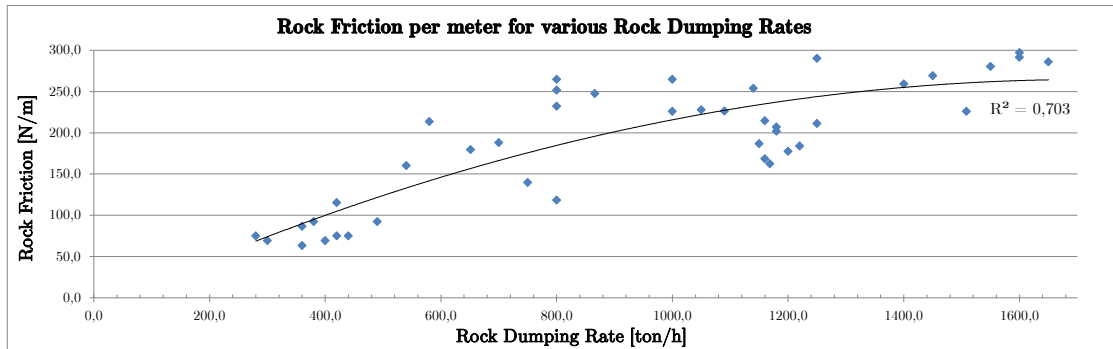


FIGURE 4.5: Amount of rock friction per meter as a function of the rock dumping rate

4.1.2 OrcaFlex Loading Scenarios Results

The results from the OrcaFlex loading scenarios are presented in this section. First, the general loading scenarios are shown, followed by the extreme current distributions and the directional current profiles scenarios. Then, the Subsea Rock Installation scenarios, the deepwater scenarios and the vessel loading conditions scenarios are evaluated. It should be noted that for the scenarios in which the Umbilical Moonpool Frame contact force is plotted, also the Umbilical Wires and the ROV are modeled in OrcaFlex. An overview of all the results can be found in Appendix D.

4.1.2.1 General Loading Scenarios Results

The first 36 loading scenarios are generated by investigating the water depths of 800, 1000, 1200 and 1400 meters for significant waves heights of 2, 4 and 6 meters and current speeds of 0, 0.2 and 0.4 meters per second. In these scenarios, no Subsea Rock Installation takes place. Figure 4.6 shows the level of tension in the top section of the starboard and portside chain as a function of time, for the scenario of 1000m water depth, 4 meter significant wave height and no current. The tension cycles in the chains are predominantly caused by the heave motions of the vessel. By applying the rainflow counting algorithm to the tension profile from Figure 4.6, one can extract tension cycles

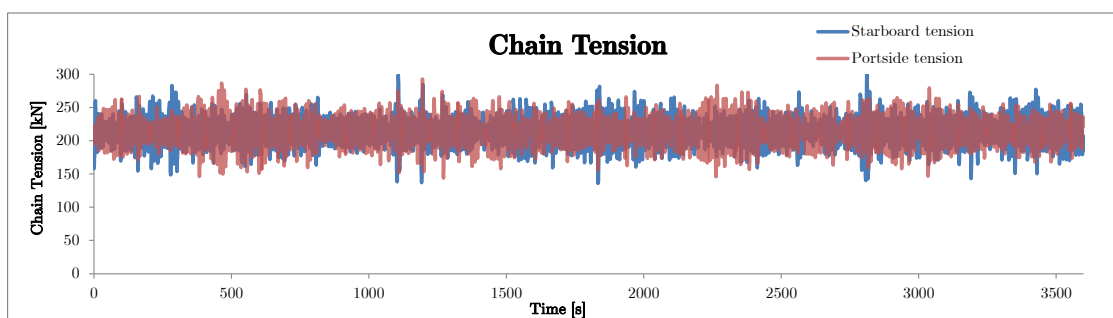


FIGURE 4.6: Chain tension in time - 1000m, 4m significant wave height, 0 m s⁻¹ current

which can be used in conjunction with a corresponding fatigue curve. This would give an estimate of the amount of fatigue that the top section of the chain has sustained. Now, by extracting the tension profiles for the entire FFP chain, and applying the same

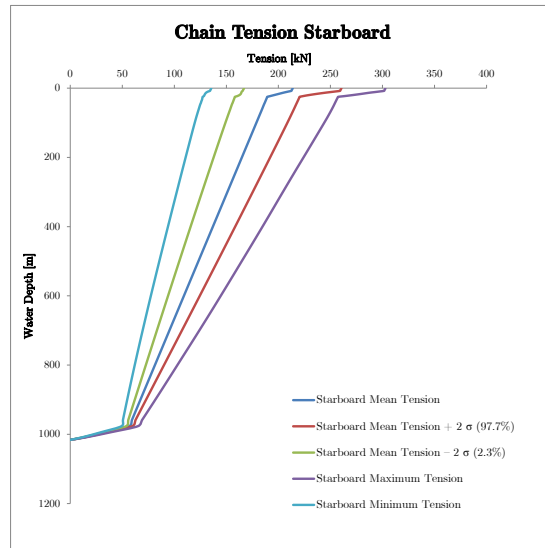


FIGURE 4.7: Chain tension range graph - 1000m, 4m significant wave height, 0 m/s current

reasoning, one can make predictions about how the fatigue progresses along the FFP chains. This will be further discussed in Section 4.5. The way in which the tension level in the chains progresses along the FFP can be presented in a range graph, of which an example can be seen in Figure 4.7. Figure 4.7 shows the level of tension in the starboard chain as a function of the chain length. Only the starboard side chain is plotted, as it is very similar to the portside chain graph. The blue line in Figure 4.7 indicates the average level of tension in the chain links, which is roughly the static weight of the FFP at that location. In the first twenty meters, the mean tension has a sharp decrease, which can be attributed to the steel buckets that are located in the top section of the FFP. After this sharp decrease at the start, the blue line shows a more gentle decrease which can be attributed to the plastic buckets which are much lighter than the steel buckets. The last section again shows a sharp decrease because of the steel buckets and the telescopic pipe in this last section. The green and the red line from Figure 4.7 indicates a bandwidth in which the mean tension plus or minus two standard deviations falls, which equals to 95.5% of the tension peaks and troughs. The light-blue and purple line show the absolute minimum and maximum value of the chain tension. In short, the range graph from Figure 4.7 gives a clear image of the magnitude of the tension cycles and the manner in which it progresses along the length of the FFP. Figure 4.8 shows the effect of the wave height (2m, 4m and 6m) on the tension cycles in the Flexible Fall Pipe for a water depth of 1000 meters, without current. Clearly, the volatility of the tension cycles increases for a higher wave height. What is interesting to see, is that there

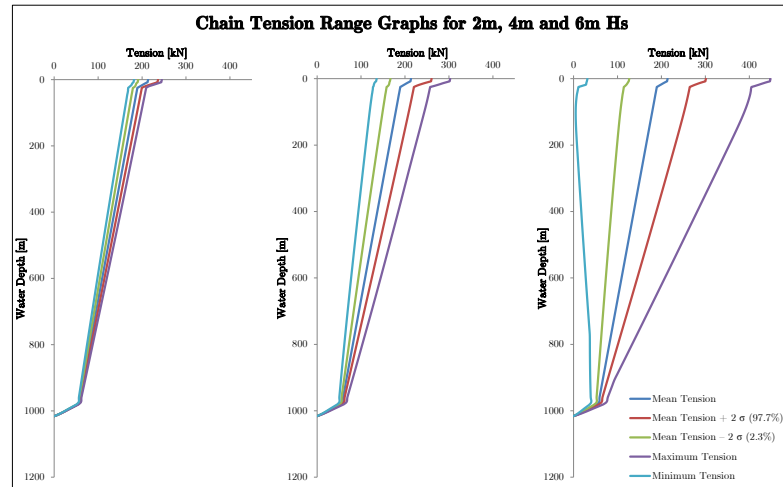


FIGURE 4.8: Effect of wave height on the chain tension - 1000m, 2m/4m/6m significant wave height, 0 m/s current

appears to be a certain 'critical wave' or 'critical vessel motion' for which tension cycles become large enough for the chain to go slack, which is undesirable. This can be seen from the right side of Figure 4.8 for the scenario with a 6m significant wave height at a water depth of roughly 100 meters. What basically happens is that the upper sections of the FFP (steel buckets) moves down more quickly than the FFP section at 100 meters (plastic buckets), causing the chain to go slack. Clearly, it is still a bit far-fetched to be working at 1000 meters with a significant wave height of 6m. However, when measures are taken to reduce the weight of the FFP (e.g. in Section 4.1.2.5), the range graph of Figure 4.8 will tilt to the left, which increases the possibility of a slack chain. Furthermore, also at lower significant wave heights there can be a combination of waves that causes a large tension peak. In the general loading scenarios, the current velocity was one of the variables of investigation. For the chain tension range graphs, almost no difference was observed for the different current speeds. For a complete overview of range graphs for the first 36 loading scenarios, the reader is referred to Figure D.23 to Figure D.58 in Appendix D.

4.1.2.2 Extreme Current Scenarios Results

Three extreme current distributions from the Ormen Lange field have been simulated, of which the distributions can be found in Appendix B. From Figure 4.9, it can be seen that the contact force increases in the first 800 seconds, this is due OrcaFlex ramping up the current speed as the simulation could otherwise become unstable.

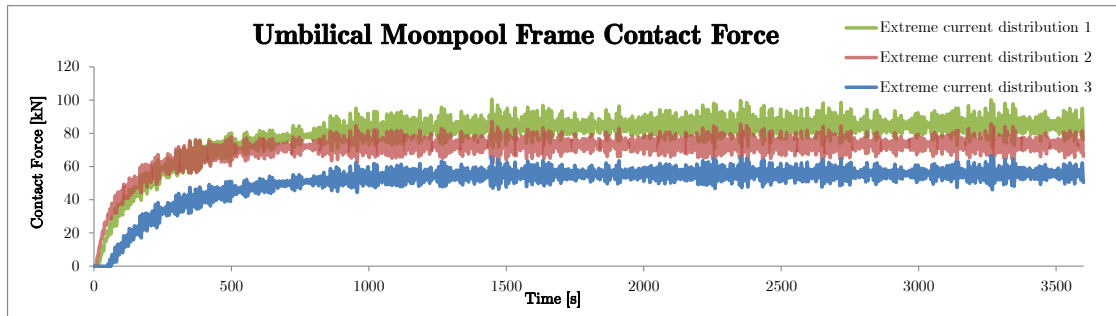


FIGURE 4.9: Umbilical Moonpool Frame contact force for three extreme current distributions - 900m water depth, 2m significant wave height

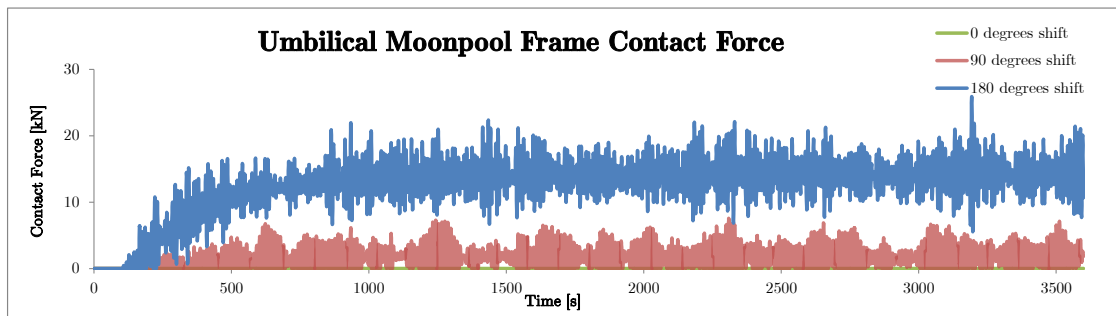


FIGURE 4.10: Umbilical Moonpool Frame contact force for a vessel velocity of 0.15 m s^{-1} and three directional current profiles - 900m water depth, 2m significant wave height and 0.3 m s^{-1} current

4.1.2.3 Directional Current Profiles Scenarios Results

During the Subsea Rock Installation process, the direction of the vessel is almost always chosen in such a way that it faces the waves head on. When the Subsea Rock Installation process is started, the vessel moves on Dynamic Positioning along the pipeline, commonly at a velocity of 0.15 m s^{-1} . During this process, the current can come from any direction really. Three current scenarios have been investigated: a shift of 0 , 90 and 180° with respect to the vessel. Figure 4.10 shows the contact force between the Flexible Fall Pipe chains and the Umbilical Moonpool Frame for these three directional current profiles. The highest contact force is found when the moving direction of the vessel is opposite to the direction of the current, which is the 180° situation.

4.1.2.4 Subsea Rock Installation Scenarios Results

Figure 4.11 shows the chain tension as a function of the time for simulating the Subsea Rock Installation process (by means of content flowing through the two lines) for $1500 \text{ tonnes h}^{-1}$ and for increasing the weight of the chains in accordance with the friction of $1500 \text{ tonnes h}^{-1}$. When simulating the Subsea Rock Installation process, two effects take place: (1) the mean tension increases and (2) a major cycle is induced when applying the rainflow counting algorithm. The dynamic behavior of the chain is more or less

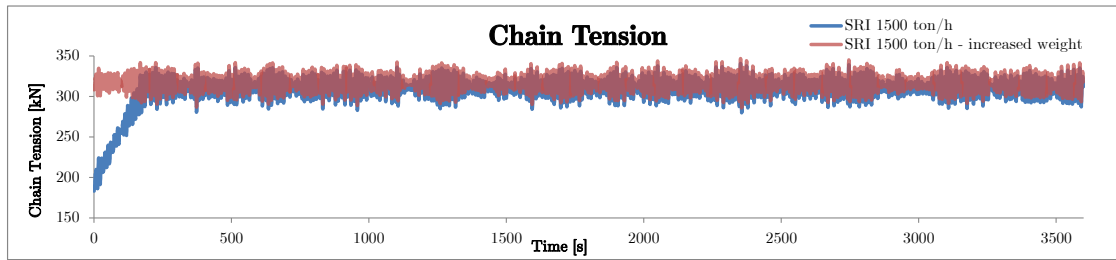


FIGURE 4.11: Chain tension comparison - simulating SRI versus increased self weight for 2m waves and 1500 tonnes h^{-1}

the same as when increasing the weight of the chains. This behavior is observed for all the comparisons between SRI and increased chain weight. Therefore, when excluding the major cycle, the behavior of the tension during the increased weight scenario is almost identical to that of the SRI modeling scenario. The advantage of this approach (increasing the weight) is that many different situations in terms of rock dumping rates can be reviewed, by simply changing the mean level of the tension. This will be further discussed in Section 4.5.

4.1.2.5 Deepwater Buckets Scenarios Results

In Figure 4.12 a range graph is presented for the Flexible Fall Pipe in 1300m water depth, 4m significant wave height, for normal buckets (left side) and deepwater buckets (right side). This scenario has been run under the assumption that the deepwater buckets have the same hydrodynamic properties as the normal buckets. The dynamic behavior

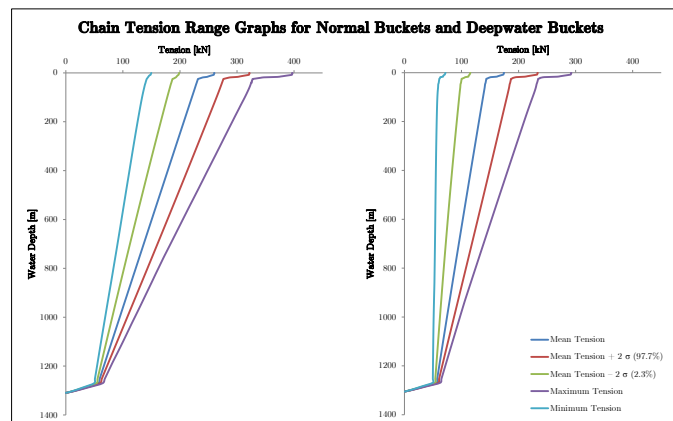


FIGURE 4.12: Chain tension range graph for normal buckets and deepwater buckets - 1300m water depth, 4m significant wave height and 0.3 m s^{-1} current

is again more or less the same, and it is the average tension which tilts to the left due to the buoyant deepwater buckets. As the mean level of tension is lower, this is favourable in terms of fatigue, but as discussed in Section 4.1.2.1, the chances of the chain to go

slack will be higher. Furthermore, when looking at the contact force in the moonpool (Figure 4.13), these forces become larger. This can be attributed to the fact that the system becomes lighter, which makes it easier for the current to shift the Flexible Fall Pipe.

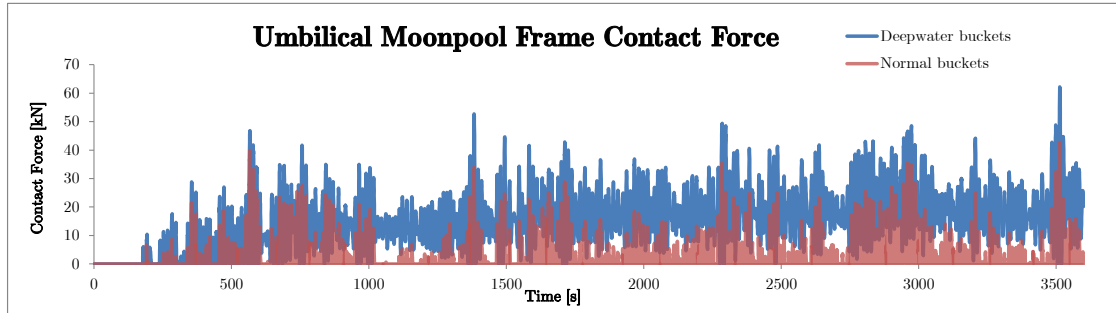


FIGURE 4.13: Umbilical Moonpool Frame contact force for normal and deepwater buckets - 1300m water depth, 4m significant wave height and 0.3 m/s current

4.1.2.6 Vessel Loading Condition Scenario Results

In addition to the standard scenario in which the cargo holds are loaded for 25% with rocks, also the situation for a fully loaded vessel is examined (see Figure 4.14). In contrary to the expectation, it appears that the motions of the vessel, and therefore the tension cycles, become more severe for the fully loaded conditions. The author has no explanation for this effect, other than that the vessel responds differently in the fully loaded condition, and in this particular situation worse. However, this is not part of the scope of this thesis.

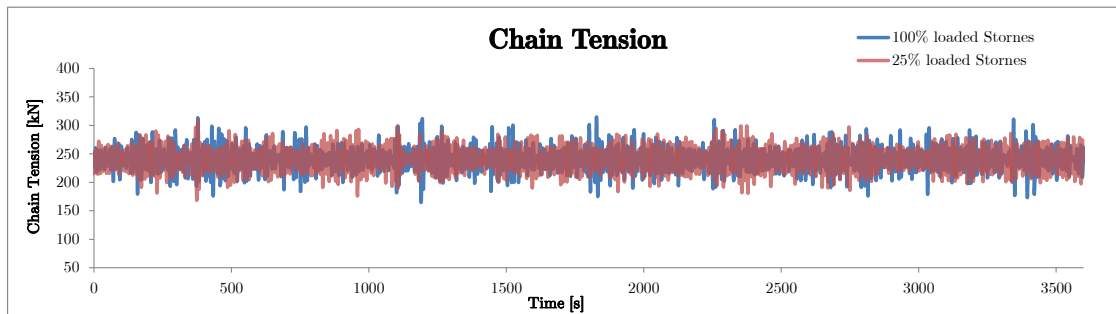


FIGURE 4.14: Chain tension - Stornes 100% loaded versus 25% loaded - 1200m water depth, 4m significant wave height and no current

4.1.2.7 Chain Link Rotations

From OrcaFlex it was found that throughout the Flexible Fall Pipe, chain link rotations are minor. This can be attributed to the fact that the effective length of a single chain

link is 108 mm, which is small compared to the length of the Flexible Fall Pipe. If there is only a small rotation between two chain links at the top, this amounts to a large offset at the bottom of the Flexible Fall Pipe. These minor rotations are considered insignificant with respect to the fatigue life of the chain links. However, there are two exceptions to this: the chain link rotations at the guidance frame on the vessel and the chain link rotations in the moonpool. When the Flexible Fall Pipe is launched and recovered, the two chains run over a guidance frame by means of a winch and seven sprocket wheels, in which the chain links are subjected to a maximum interlink rotation of 6.6° . In the moonpool, a maximum interlink rotation of 3.7° was found during extreme current distribution case 1. However, this might be an overestimation, as the local contact may differ in reality from the OrcaFlex simulation. In OrcaFlex, the chains come into contact with the Umbilical Moonpool Frame, whereas in reality it might be the buckets. As the buckets have a larger bending radius than the chains, the chain link rotations could be less than 3.7° in the moonpool.

4.2 Results from Finite Element Model of the Chain Link

The results of the Finite Element Model of the chain link will be discussed in this section. First, the quarter chain link model will be evaluated and the amount of refinement in the mesh will be established. Then, the full chain link model will be discussed and the parameters in the contact analysis will be reviewed. Finally, the effect of the chain link rotations will be discussed.

4.2.1 Quarter Chain Link Model

In the first loading scenario, the quarter chain link model is constrained in the nodal x, y and z-direction on the bottom area, as shown in Figure 4.15. The top left area

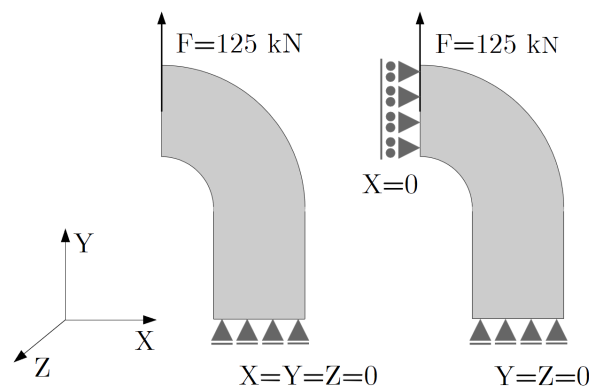


FIGURE 4.15: FEM loading scenarios for the quarter chain link: case 1 (left side) and case 2 (right side)

is loaded by a force of 125 kN, equivalent to a tension level of 250 kN. As there is no displacement boundary conditions on the top left area of the quarter chain link, the y-stress distribution on the bottom section can be calculated analytically by means of Equation 4.1.

$$\sigma_{y\min,\max} = \frac{F}{A} \pm \frac{M_b y}{I} \quad (4.1)$$

In Equation 4.1, F is the external forcing and A is the cross-sectional area of the chain link, which is equal to $\frac{\pi}{4} \cdot D^2$. M_b is the bending moment, in this case equal to $F \cdot e$, in which e is the eccentricity of the applied force with respect to the centre of the bottom area. The outer fiber distance is denoted by y . I is the area moment of inertia, which is equal to $\frac{\pi}{64} \cdot D^4$. The resulting stress distribution in the quarter chain link is shown in Figure 4.16, for different levels of mesh refinement. Additionally, the analytical solution

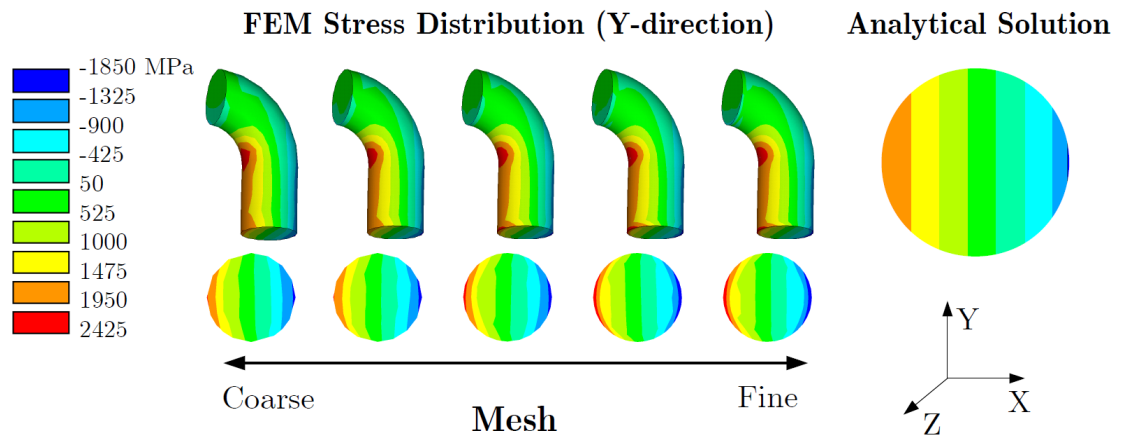


FIGURE 4.16: Quarter chain link y-stress distribution (case 1) - Finite Element Analysis versus analytical solution

for the y-stress distribution is shown on the right side of Figure 4.16 and it is plotted on the same scale as the FEA results. It should be noted that the peak stress can go above the yield stress (1280 MPa) of the material, as ANSYS assumes linear elastic material behaviour. The peak stress is very high in Figure 4.16, as there is no boundary condition on the upper left area of the chain link (yet), which means that there is no counter balancing moment on the left side of the chain link. The location of the peak stress in the inner bend region of the chain link is in accordance with the fatigue failure location that was found from the real-life fatigue testing and from literature.

Setting the Mesh Refinement Before looking into different loading conditions, the amount of mesh refinement has to be established. A finer mesh should give more accurate results, but it comes at the cost of longer computational time. Table 4.1 displays mesh input parameters and some key numerical results, e.g. the minimum and maximum y-stress at the bottom section of the quarter link and the Von Mises peak stress at the bend section of the quarter chain link. When meshing volumes, there are two parameters that

TABLE 4.1: FEM results - quarter chain link case 1

Load case	SMRTSIZE	EXTOPT	Number of elements	Von Mises peak stress [MPa]	$\sigma_{y max}$ (bottom area) [MPa]	$\sigma_{y min}$ (bottom area) [MPa]
1	8	10	270	2431.2	1978.5	-1491.1
2	6	15	525	2320.1	1977.5	-1564.0
3	4	20	1240	2378.9	2126.6	-1563.8
4	2	25	4100	2418.9	2316.8	-1837.3
5	1	35	4585	2409.3	2359.3	-1805.9

can be used to achieve a finer or coarser mesh: SMRTSIZE and EXTOPT. SMRTSIZE sets the sizing level of the mesh from 1 (fine) to 10 (coarse). EXTOPT sets the number of elements divisions in the direction of volume sweep. One should choose both parameters in such a way that both roughly have the same level of finesse, as otherwise very flat or very long elements are created, which leads to reduced accuracy. Table 4.1 shows that as the mesh is further refined, the Von Mises stress converges and in Figure 4.16 the contour lines become smoother. As all nodes on the bottom area of the quarter link are constrained, further mesh refinement gives higher stresses at the edges, which can also be seen from Figure 4.16. The results for the second load case of the quarter chain link (Figure 4.15), in which there is an additional boundary condition on the left side, are shown in Table 4.2. As can be seen from Table 4.2, the peak stresses are more realistic and much lower than for the first case. Again it is observed that the peak stress appears to converge. For load case 9, the stress goes slightly up, however in relative terms it is still acceptable (merely 1.2% difference). For the refinement of the mesh, a value of 4 for the SMRTSIZE option and 20 for the EXTOPT option is selected (middle figure of Figure 4.16). This provides a level of accuracy which is adequate, at a reasonable computational effort.

TABLE 4.2: FEM Results - quarter chain link case 2

Load case	SMRTSIZE	EXTOPT	Number of elements	Von Mises peak stress [MPa]	$\sigma_{y max}$ (bottom area) [MPa]	$\sigma_{y min}$ (bottom area) [MPa]
6	8	10	270	660.3	539.4	-200.3
7	6	15	525	663.7	528.7	-197.0
8	4	20	1240	688.4	554.6	-193.0
9	2	25	4100	701.3	624.4	-192.1
10	1	35	4585	692.7	582.6	-188.3

4.2.2 Full Chain Link Model

For the full chain link model, the contact analysis is first reviewed in Section 4.2.2.1, then the stress distribution is evaluated in Section 4.2.2.2 and lastly, chain link rotations are discussed in Section 4.2.2.3.

4.2.2.1 Contact Analysis

To model contact between two volumes, ANSYS uses contact elements that overlay the deformable body, this can be seen in Figure 4.17. These contact elements use a 'target surface' and a 'contact surface' to form a contact pair. The target surface is modeled with element type Targe170 and the contact element uses element type Conta174. Different parameters can be specified in the contact analysis and the three main parameters will be discussed: the penalty stiffness (PSTIFFNESS), the pinball radius (PINB) and the initial closure (ICONT) (Ansys, 2009). For the penalty stiffness, a method is applied that

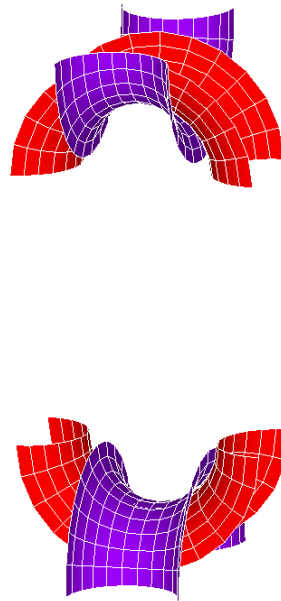


FIGURE 4.17: Representation of the contact elements in ANSYS

uses a contact 'spring' to establish a relationship between the two contacting surfaces. The amount of penetration between the contact and target surfaces depends on this penalty stiffness. Ideally, the stiffness should be as high as possible to have acceptably small penetration, as one will then get closer and closer to the 'real' problem. However, high stiffness values can lead to ill-conditioning of the global stiffness matrix and to convergence difficulties. Therefore, the stiffness should be low enough that the problem is well-behaved in terms of convergence (Ansys, 2009). The penalty stiffness is proportional to the Young's Modulus, and a penalty stiffness ranging from 0.001 to 10 in steps of

a factor 10 has been investigated. Starting from a penalty stiffness of 10, convergence difficulties were experienced. Therefore, the penalty stiffness is set to a value of 1. The second main parameter is the Pinball Radius (PINB), which is the radius in which ANSYS searches for an accompanying target element that can come in contact with the contact element. In 2D, this can be viewed as a circular region, whereas in 3D it can be seen as a sphere. In specifying the Pinball Radius, it has to be large enough to find the accompanying target elements to make contact. At the same time, one wants to specify it to be as small as possible to reduce calculation time. This requires some trial-and-error and ANSYS can assist in finding a correct value for the Pinball Radius. The Pinball Radius is currently set to 1, which is equal to 1 times the depth of the underlying element. Thirdly, there is the initial closure (ICONT), which can be seen as an adjustment band around the target surface. Any contact detection points are internally shifted to be on the target surface. By increasing this parameter the simulation can become more stable, but when the value of this parameter is too high, contact is established where it normally does not occur (spurious contact). The value of this parameter is currently set to 15% of the depth of the target element. Finally, when the parameters are set to these values, 46 of the total 288 contact elements are in contact.

4.2.2.2 Analysing the Stress Distribution

Figure 4.18 shows the loading configuration of the full chain link model (left side) and the Von Mises stress distribution as obtained from ANSYS (right side). The location of the peak stresses in Figure 4.18, in the inner bend region of the chain link, is in correspondance with the quarter chain link model. The magnitudes of the Von Mises

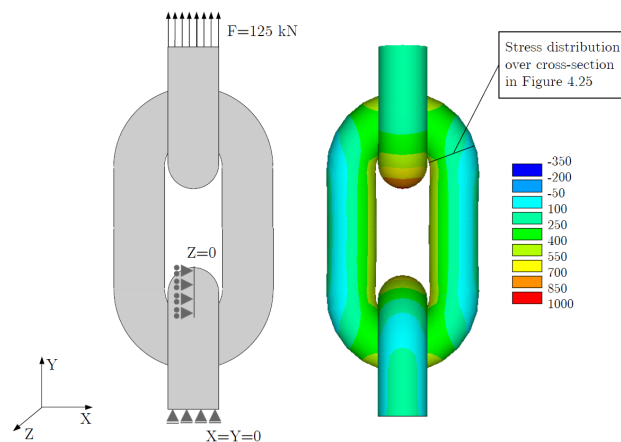


FIGURE 4.18: Full chain link FEM results - Von Mises peak stresses

peak stresses in the full chain link are 612.1, 612.5, 615.8 and 616.4 MPa versus the 688.4 MPa which was found from the quarter chain link model. The Von Mises stress distribution in the upper half chain link from Figure 4.18 is fairly uniform, and low with

respect to the rest of the model. This can be attributed to the fact that there are no displacement constraints at the top half chain link, and the applied loading is a pressure perpendicular to the top two areas. As a result, there is only axial stress in the top part of the upper half chain link, and no bending stress. The lower half chain link exhibits the same stress pattern as the full chain link and the quarter chain link. The two Von Mises peak stresses in the lower half chain link amount to 615.9 and 616.0 MPa. However, when the chain link rotations will be investigated (next section), an additional bending moment will be induced in the lower half chain link as it is constrained at the bottom areas. In reality, the chain link is not constrained half-way and the stress in the lower half chain link will be different. Therefore, in the further analysis, the main focus will lie on the peak stresses in the full chain link.

4.2.2.3 Chain Link Rotations

As discussed in Section 4.1.2.7, a maximum rotation of 6.6° was found on the guidance structure and a maximum rotation of 3.7° was found in the moonpool. Figure 4.19 shows the loading configuration for chain link rotations on the left side, and the resulting Von Mises stress distribution on the right side. Four peak stresses are identified in the

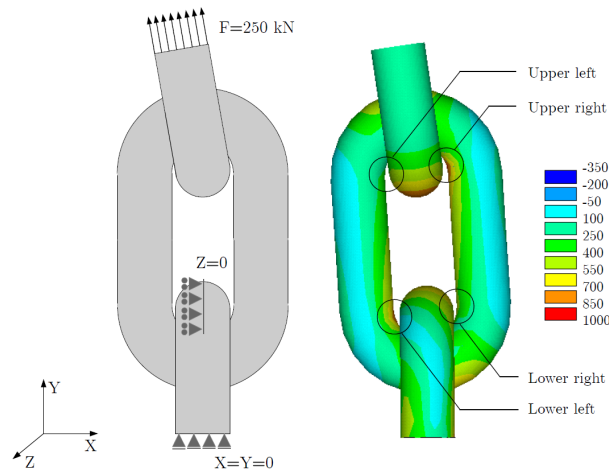


FIGURE 4.19: Chain link rotations Finite Element Model results - Von Mises peak stresses for $\mu=0.4$ and $\alpha=5^\circ$

full chain link: the upper right, upper left, lower right and lower left peak stress. In Figure 4.20 it is shown how these Von Mises peak stresses develop for chain link rotations from 0 to 7° and for friction factors ranging from 0.2 to 0.6 . Now, when reviewing the upper right Von Mises peak stress for a friction factor of 0.2 , it can be seen that the peak stress increases up to a rotation of 3° . For higher rotations, ANSYS cannot solve to a static solution anymore, as there is rigid body motion. This basically means that for rotations up to 3° , the chain link 'sticks' and builds up stress, and for rotations higher than 3° the chain link 'slips' and the stress is released. Now, for a higher friction

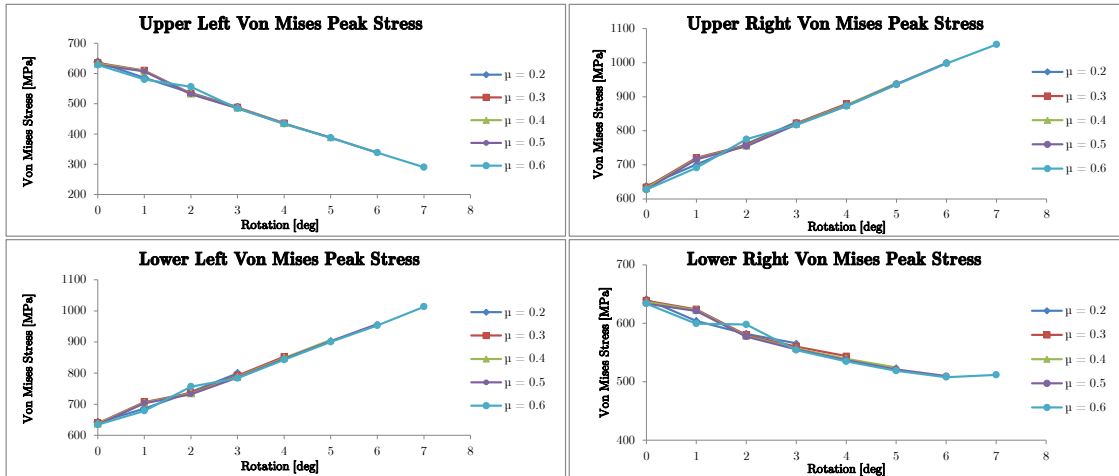


FIGURE 4.20: Full chain link FEM results - Von Mises peak stresses during chain link rotations

coefficient, the chain link can build up more friction before slipping, and the upper right peak stress increases further. For the highest friction coefficient of 0.6, the chain links still stick at 7° rotation. As the full chain link rotates around the center of the bottom half chain link, the same stress build up is observed for the lower left Von Mises peak stress in Figure 4.20. For the upper left and lower right Von Mises peak stress, the stresses decrease as, due to the rotation, compressive stresses are induced which cancel out against a part of the previously imposed tensile stresses. As it is difficult to see from Figure 4.20 as all the lines coincide, Table 4.3 shows the maximum rotation for which the chain links still stick as a function of the friction factor μ . When the chain links

TABLE 4.3: Friction factor and maximum rotation for which 'stick' still occurs

Friction Factor μ	Maximum 'stick' rotation [$^\circ$]
0.2	3
0.3	4
0.4	5
0.5	6
0.6	7

slip, ANSYS cannot solve to a static solution anymore and therefore it was decided to review another load case. In this load case, half of the rotation is applied at the top half chain link and the other half of the rotation is applied at the full chain link. For that load case, the peak stresses exhibit the same pattern as before, but less abundant. This is shown in Figure 4.21 with the open markers, and for completeness the results from Figure 4.20 have also been plotted. For this load case, the chain links can rotate further; only for $\mu = 0.2$ and $\alpha = 7^\circ$ no solution was obtained. A full overview of the peak stresses for the different load cases can be found in Appendix D, Figures D.74 to D.76.

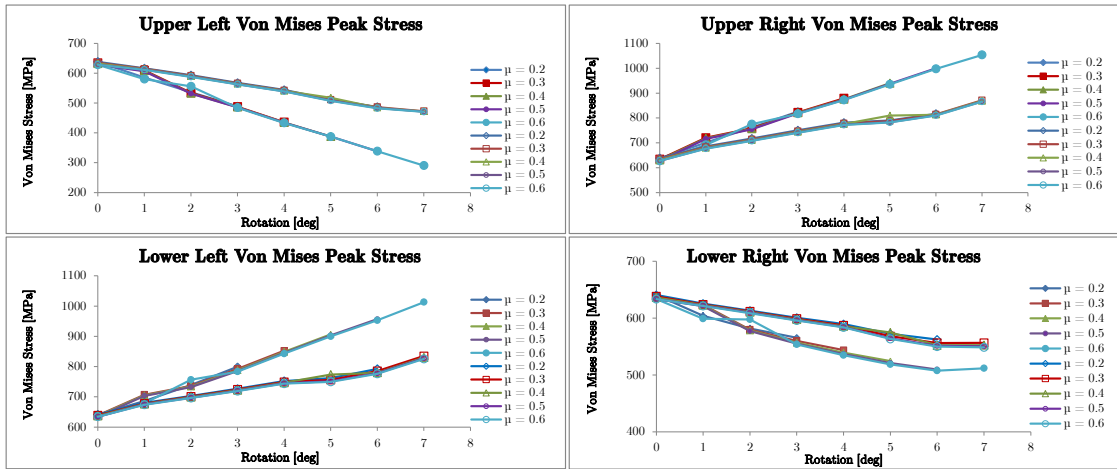


FIGURE 4.21: Full chain link FEM results - Von Mises peak stresses during chain link rotations

4.3 Results from the Fatigue Testing of the Chain Links

At TNO, real-life fatigue tests have been performed on three chain links in a tensile test bench at a frequency of 1 Hz and a constant amplitude sinusoidal load. Before testing, a bag of seawater was wrapped around the chain links to incorporate the effect of corrosion. This seawater was made according to Atlantic Ocean quality. The full specifications of the tests including the results can be seen in Table 4.4. This table shows the applied loading during the fatigue testing, the number of cycles to failure, the stress ratio R , which is the ratio of the minimum stress to the maximum stress, and the failure location. The failure location of the chain link is indicated with a letter S (straight section) or B (bend section) and a number indicating the chain link that failed,

TABLE 4.4: Fatigue testing results

Test no.	Lower range [kN]	Upper range [kN]	Mean load [kN]	Tension range [kN]	Percentage of break-load [%]	Stress ratio R [-]	Failure location	Number of cycles to failure [-]
1	150	200	175	50	4.17	0.75	-	2000000+
2	150	250	200	100	8.33	0.60	B3	358500
3	150	250	200	100	8.33	0.60	B3	305058
4	150	250	200	100	8.33	0.60	B1	315274
5	150	300	225	150	12.50	0.50	S1	117568
6	150	300	225	150	12.50	0.50	B1	155429
7	175	375	275	200	16.67	0.47	S1	48750
8	175	375	275	200	16.67	0.47	B1	65913
9	175	375	275	200	16.67	0.47	B1	54980
10	100	400	250	300	25.00	0.25	S1	18789
11	100	500	300	400	33.33	0.20	S2	12805
12	100	500	300	400	33.33	0.20	B1	14361
13	100	500	300	400	33.33	0.20	B2	16532

with '1' being the top link, '2' being the middle link or '3' being the bottom link. For example, S2 means that the middle chain link failed at the straight section. It should be noted that in every case either the middle chain link failed, or one of the other two chain links failed *on the side* of the middle chain link. In other words, the locations where the top and bottom chain links were connected to the testing setup were smooth enough not to induce local stresses that were high enough to cause failure. The results from the fatigue testing are plotted in Figure 4.22. The number of cycles to failure are plotted on the horizontal axis and the chain tension as a percentage of the Minimum Break Load (MBL) are plotted on the vertical axis. The blue squares indicate the results from the most recent tests with the chain link, whereas the orange triangles show the results from the fatigue testing with the Dominator connection links. Furthermore, the fatigue curves from Rossi (2005), that were discussed in Section 2.3.2, have been plotted in the same graph. The slope of the fatigue curve that was found is very much in line with the curves that were obtained from Rossi (2005). However, the datapoints from the experiments clearly lie below the fatigue curves from Rossi (2005), even below the design curves from DNV and API. Although it is a large difference, it might be partly attributed to the high mean load ($F = 250\text{kN}$) that was used during the tests at TNO. Still, it is evident that the standard design codes are not sufficient for the chain in this application.

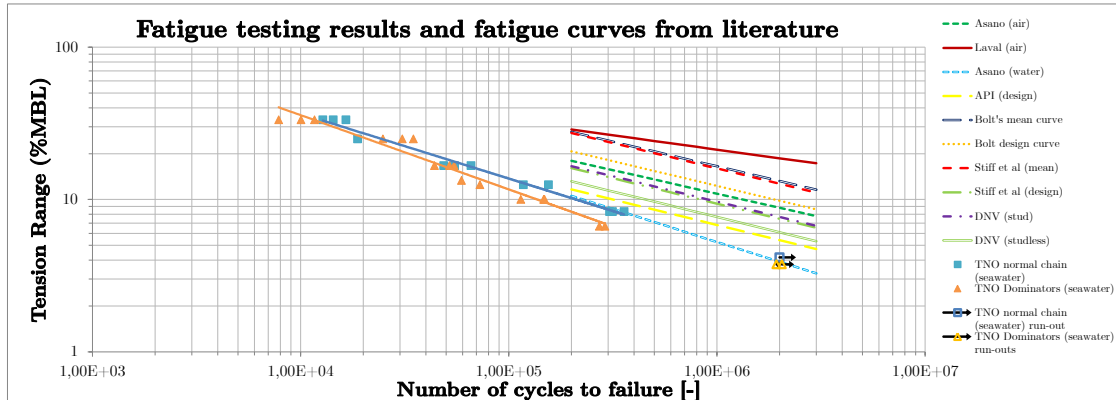


FIGURE 4.22: Fatigue testing results and fatigue curves from literature

4.4 Results from the Analytical Derivation of the Fatigue Curves

To investigate the effects of certain factors (e.g. mean stress, surface roughness) on the fatigue life, one can analytically derive the fatigue curve for the chain link, without having to do real-life testing. For the analytical derivation of the fatigue curve of the chain link, the design process as described in Gudehus (1999) has been adopted (design

flowchart shown in Figure C.3 on page 90). The idea of this method is to identify the five parameters that are required to construct the fatigue curve in Figure 4.23: N_D , the number of cycles at the endurance limit stress, σ_{aD} , the endurance limit stress, k , the slope of the fatigue curve, R_e^* , the deformation fatigue limit stress and R_m^* , the ultimate fatigue strength. These parameters will be fully described later on in this chapter.¹ Figure 4.23 shows a typical fatigue curve with the logarithm of the number of cycles

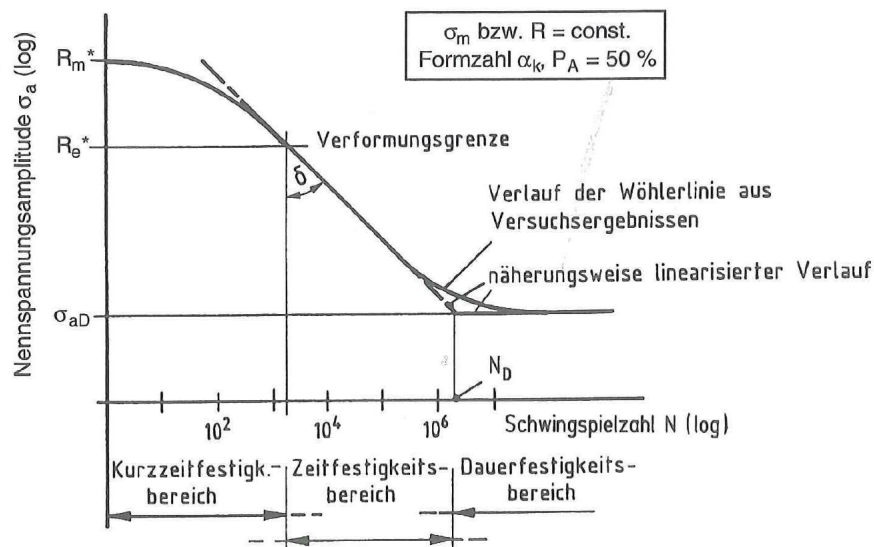


FIGURE 4.23: Synthetic fatigue curve (Gudehus, 1999)

to failure N on the horizontal axis and the logarithm of the stress amplitude σ_a on the vertical axis. It also indicates three ranges, the 'Kurzzeitfestigkeitsbereich' or the low-cycle fatigue strength range, the 'Zeitfestigkeitsbereich' or the high-cycle fatigue strength range and the 'Dauerfestigkeitsbereich' or the infinite fatigue life range. In the derivation of the design points of the synthetic fatigue curve, the graph in Figure 4.24 is useful for clarification. Figure 4.24 shows the stress-strain diagram for an 8x40 mm specimen that was taken from the chain, with the relevant parameters indicated. The diagram in Figure 4.24 shows R_e , the deformation limit stress, which is the stress at which first plastic deformation occurs, $R_{p0.2}$, the stress corresponding to a permanent elongation of 0.2% and R_m , the ultimate break strength of the material. To refer back to the analytical derivation of the fatigue curve, the first step in this design process is to determine the deformation fatigue limit stress R_e^* , which is the pivot point from the low-cycle fatigue range to the high-cycle fatigue range. The calculation of R_e^* is indicated with Equation 4.2.

$$R_e^* = R_e - \sigma_m \quad (4.2)$$

¹The notation for the parameters describing the fatigue curve in this section is in accordance with Gudehus (1999). This notation will only be used when discussing the synthetic fatigue curve.

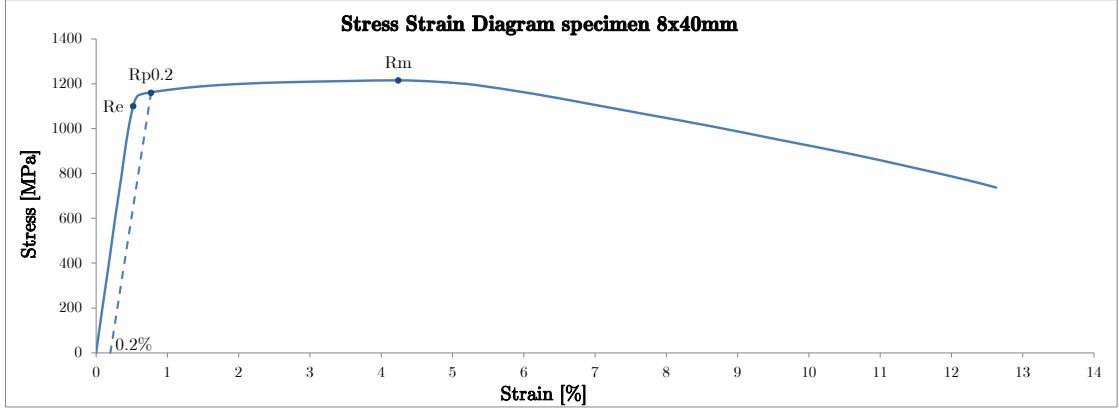


FIGURE 4.24: Stress-strain diagram of a 8x40 mm specimen taken from the chain

Similarly, the ultimate fatigue strength R_m^* is determined by Equation 4.3, in which R_m is the break strength of the material. The ultimate fatigue strength R_m^* is the second design point of the synthetic fatigue curve.

$$R_m^* = R_m - \sigma_m \quad (4.3)$$

The third step in this analytical derivation is to determine the endurance limit stress, σ_{aD} , which is the stress range below which no fatigue failure occurs. The endurance limit stress can be obtained by factorizing the fatigue strength of a smooth steel specimen σ_W to account for non-idealities. The fatigue strength σ_W is a function of $R_{p0.2}$, and is shown in Equation 4.4.

$$\sigma_W = 0.436 \cdot R_{p0.2} + 77 \quad (4.4)$$

The fatigue strength σ_W can be viewed as the ideal strength of a steel specimen. As it is not ideal in reality, σ_W will be corrected for with various factors, accounting for the geometry, size, production methods and surface roughness. The geometry is accounted for with the form factor α_k , which is the ratio of the peak stress σ_{peak} to the nominal stress σ_{nom} , as shown in Equation 4.5. Both stresses are taken in the y-direction.

$$\alpha_k = \frac{\sigma_{peak}}{\sigma_{nom}} \quad (4.5)$$

The peak stress σ_{peak} occurs at the inner bend section of the chain link and is obtained from the FEA from Section 4.2. The nominal stress σ_{nom} is found by utilizing Equation 4.6 at the chain link's cross-section where the peak stress occurs.

$$\sigma_{nom} = \frac{T}{A} + \frac{M_b}{W_b} \quad (4.6)$$

In Equation 4.6, T is the tension, A the cross-sectional area, M_b the bending moment and W_b the bending section modulus. The determination of the bending moment M_b and the

nominal stress σ_{nom} requires some arithmetic and is described in Appendix C on page 86. It should be noted that the definition for the nominal stress σ_{nom} can depend on the literature that is used, as sometimes the bending term in Equation 4.6 is omitted, e.g. in Det Norske Veritas (2010). As one has now obtained the form factor α_k by utilizing Equation 4.5 and 4.6, it can be used to determine the notch factor β_k . The notch factor β_k can be described as the parameter that takes into account the influence of stress raisers on the fatigue life, and it is calculated by means of Equation 4.7. Whereas α_k is only a function of geometry, β_k is also dependent on the mean stress, the type of stress and the influences of the type of material and the size. As this makes the calculation of β_k complex, Gudehus (1999) uses the statistical representation from Equation 4.8.

$$\beta_k = \frac{\alpha_k}{n} \quad (4.7)$$

$$n = 1 + 0.45 \cdot \chi^{*0.30} \quad (4.8)$$

In Equation 4.8, n is the supporting factor and χ^* is the stress gradient at the location of the peak stress (see Figure 4.18). The stress distribution and the associated stress gradient of the inner bend region of the chain link is shown in Figure 4.25. The next step

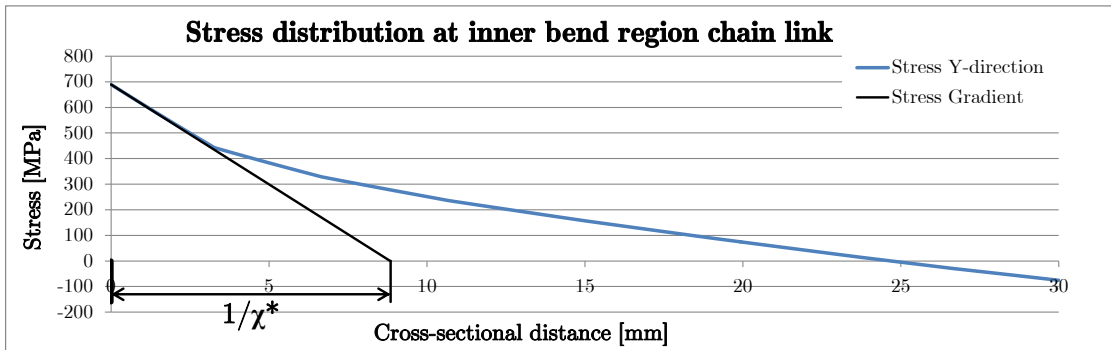


FIGURE 4.25: Stress gradient χ^* at the inner bend region of the chain link (see also Figure 4.18)

is to determine the technological factor F_T , which will factorize the ideal fatigue strength σ_W for the production method that is used. The technological factor F_T is function of the break strength R_m , as a higher break strength involves more rapid quenching during production (and thus a lower F_T value).

$$F_T = \frac{2069 - R_m}{1790} \quad (4.9)$$

As a component is cyclically loaded, small cracks will form (crack initiation) and they will grow (crack propagation) until the component fails (fatigue fracture). It will be easier for cracks to initiate as a material component has a higher surface roughness. Further, the brittleness of the material component also affects the crack formation process and the fatigue life. The surface factor F_0 , shown in Equation 4.10, takes into account the

surface roughness R_z and the brittleness of the material component. The brittleness is incorporated by means of the break strength of the material R_m .

$$F_0 = 1 - 0.22 \cdot R_z^{0.64} \cdot \log R_m + 0.45 \cdot \log R_z^{0.53} \quad (4.10)$$

The technological factor F_T and the surface factor F_0 is combined into the technological and surface factor F_{0T} , which is shown in Equation 4.11.

$$F_{0T} = 1 - \sqrt{(1 - F_0)^2 + (1 - F_T)^2} \quad (4.11)$$

Then, the influence of the notch factor β_k and the technological and surface factor F_{0T} is taken together as the fatigue strength reduction factor F_{0Tk} .

$$F_{0Tk} = \sqrt{\beta_k^2 - 1 + \frac{1}{F_{0T}^2}} \quad (4.12)$$

Thus, the fatigue strength reduction factor F_{0Tk} takes into account the non-idealities and reduces the ideal fatigue strength of material σ_W to the fatigue strength of the component σ_{Wk} , as shown in Equation 4.13.

$$\sigma_{Wk} = \frac{\sigma_W}{F_{0Tk}} \quad (4.13)$$

To find the endurance limit stress σ_{aD} , it is still required to take into account the effect of the mean stress σ_m , by means of the mean stress influence factor F_m , as shown in Equation 4.14.

$$\sigma_{aD} = \sigma_{Wk} F_m \quad (4.14)$$

By constructing the graph which is shown in Figure 4.26, one will be able to determine the mean stress influence factor F_m . This method is based on a modified version of the Goodman line, which was discussed earlier in Section 2.3.4. In Figure 4.26 there is one parameter which has not been discussed thus far: σ_t . The threshold fatigue stress σ_t is the stress at which the mean stress is equal to or larger than the stress amplitude, and it is determined by means of Equation 4.15.

$$\sigma_t = \frac{2 \cdot \sigma_W}{M + 1} \quad (4.15)$$

In Equation 4.15, M is the mean stress sensitivity factor, which can be calculated by means of $M = 0.00035 \cdot R_m - 0.1$. All the parameters required to construct the graph of Figure 4.26 are now known. The horizontal axis of Figure 4.26 shows the mean stress σ_m and the vertical axis shows the stress amplitude σ_a . Further, one can see the solid lines of constant stress ratio R . F_m can be found by reading off the F_m -value for the intersection point between thick solid line and either the line of constant stress ratio R or a line for

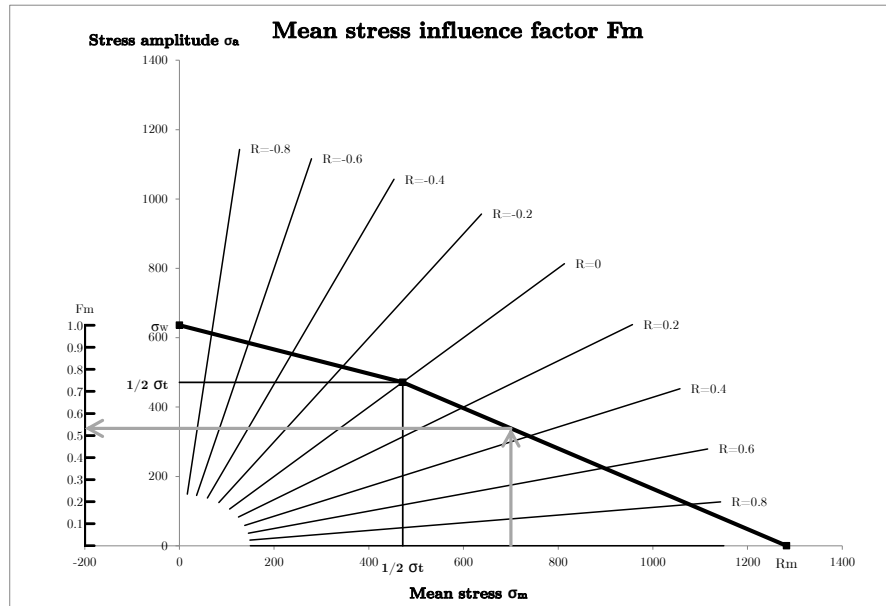


FIGURE 4.26: Quantifying the mean stress influence factor F_m (Gudehus, 1999)

a constant mean stress σ_m , depending on which one is most constant. As the majority of the time during the SRI operations the mean stress in the chain will be constant, F_m is determined based on a constant mean stress. The grey arrow in Figure 4.26 shows an example of the determination of the mean stress influence factor. Consider the situation in which the mean stress is 700 MPa. When now reading off the thick black solid line a F_m correction factor of 0.53 is found. As the method for determining the F_m -value is discussed, it can now be used in Equation 4.14 to determine the endurance limit stress σ_{aD} . To refer back to the synthetic fatigue curve from Figure 4.23, three design points have now been established: the ultimate fatigue strength R_m^* , the deformation fatigue strength R_e^* and the endurance limit stress σ_{aD} . The fourth design point is the slope of the fatigue curve k , which is a function of the fatigue strength reduction factor F_{0Tk} , which was determined from Equation 4.12. By using this method, the slope of the fatigue curve is always larger than 3, as can be seen from the Equation 4.16.

$$k = \frac{12}{F_{0Tk}^2} + 3 \quad (4.16)$$

The fifth and last point in this design process is the endurance limit number of cycles N_D , which belongs to the lower pivoting point of Figure 4.23. The endurance limit number of cycles N_D can be determined using Equation 4.17.

$$\log N_D = 6.4 - \frac{2.5}{k} \quad (4.17)$$

All the parameters required to compose the synthetic fatigue curve are now known. The result of the analytical derivation of the fatigue curve is shown in Figure 4.27 in purple,

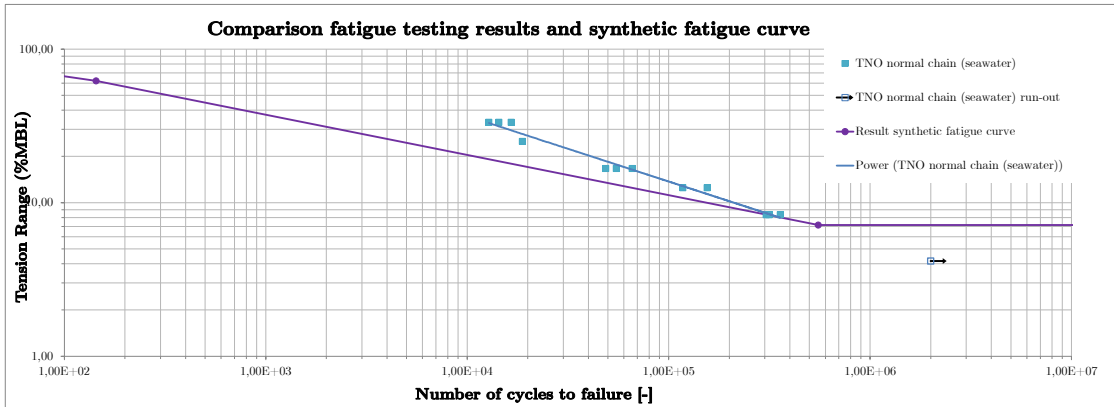


FIGURE 4.27: Comparison between the synthetic fatigue curve and the fatigue testing results

together with the results from the real-life fatigue testing from Section 4.3 in blue. From Figure 4.27 it appears that, except for the synthetic fatigue curve slope k , the analytical derivation comes close to the measurement results. The fact that the slope k is off, was to be expected, as Gudehus (1999) states the following: 'Nach neueren Erfahrungen kann die Neigung k bei Biegung steiler und bei Torsion flacher sein als nach dieser Beziehung.' In other words, for problems which are dominated by bending, which is the case for this chain, new experiences show that the fatigue curve slope k can be steeper than proposed by the relation from Equation 4.16. However, Gudehus (1999) does not specify another relationship for k and other literature was also not decisive on this matter. Therefore, it was decided to adopt the slope from the fatigue measurements, m , to get a better match with the fatigue testing results. As a result of this, the relationship for the endurance limit N_D from Equation 4.17 becomes invalid. The relationship from Equation 4.17 has been obtained from a large number of fatigue tests which is depicted in Figure 4.28, which shows the endurance limit N_D as a function of the fatigue curve slope k . As can be seen from Figure 4.28, the majority of the datapoints are located for slopes ranging from $k = 5$ to $k = 10$. At the very steep slopes (i.e. $k = 2$, $k = 3$), which is key to this research, there is a limited amount of datapoints with a large spread. This makes it unjustified to use the relationship from Equation 4.17. Nevertheless, information regarding the endurance limit N_D can be obtained by utilizing the relationship from Equation 4.18 (Haibach and Pahl, 1992).

$$\frac{N}{N_D} = \left(\frac{\sigma_A}{\sigma_{aD}} \right)^{-k} \quad (4.18)$$

To find N_D from Equation 4.18, it required to know σ_{aD} , k , N and σ_A . The endurance limit stress σ_{aD} was already determined by the analytical derivation and the synthetic fatigue curve slope k is set equal to the fatigue curve slope m from the fatigue measurements. N and σ_A can be found by choosing an arbitrary point on the fatigue curve that

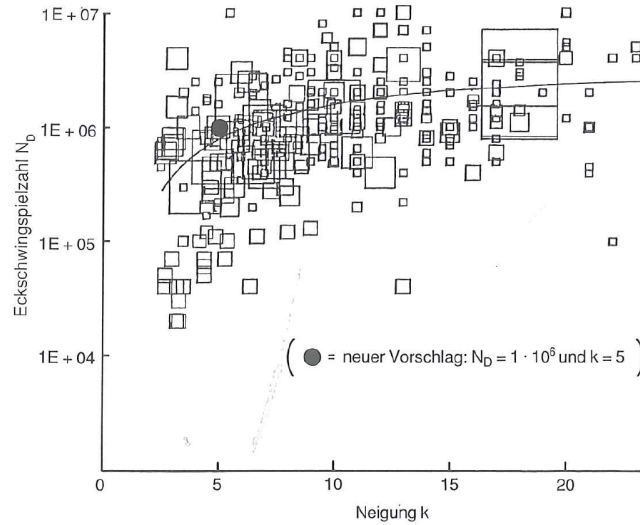


FIGURE 4.28: Endurance limit N_D as a function of fatigue curve slope k (Hück et al., 1983)

was constructed from the measurements (the blue line from Figure 4.27). In Figure 4.27, the fatigue curve continues as a horizontal straight line when the number of cycles N is larger than the endurance limit N_D . However, in practice, it may occur that components fail below this endurance limit stress, especially in a corrosive environment. For this reason, a slightly modified version for the fatigue curve in the infinite fatigue life range is adopted, with a slope which is less steep than in the high-cycle fatigue range (Haibach, 1989). This is shown by Equation 4.19, in which the slope of the fatigue curve in the infinite life range is set equal to $2k - 1$. At $N=2 \cdot 10^6$ cycles, the fatigue curve is cut-off in correspondence with Haibach (1989).

$$N_{fictive} = N_D \left(\frac{\sigma_{ai}}{\sigma_{aD}} \right)^{(2k-1)} \quad (4.19)$$

It should be noted that the relationship in Equation 4.19 has been established based on generic fatigue data, which in general has fatigue curve slopes which are much higher than the fatigue curve slope which was found for this particular application. As a result, the fatigue curve slope in the range which is furthest to the right in Figure 4.29, is still quite steep. This could lead to an under-estimation of the fatigue life in this range. By processing the changes from Equations 4.18 – 4.19, the synthetic fatigue curve changes from Figure 4.27 to Figure 4.29. All the parameters that were used in the analytical derivation of the synthetic fatigue curve can be found in Table 4.5. In the derivation of the fatigue curve, it was assumed that the loading (and therefore the stress) is predominantly in one direction, in this case the y-direction. This is a valid assumption for 'normal' chain loading, i.e. without chain link rotations. The maximum stress in y-direction that was found is 648.5 MPa, whereas the maximum Von Mises stress is

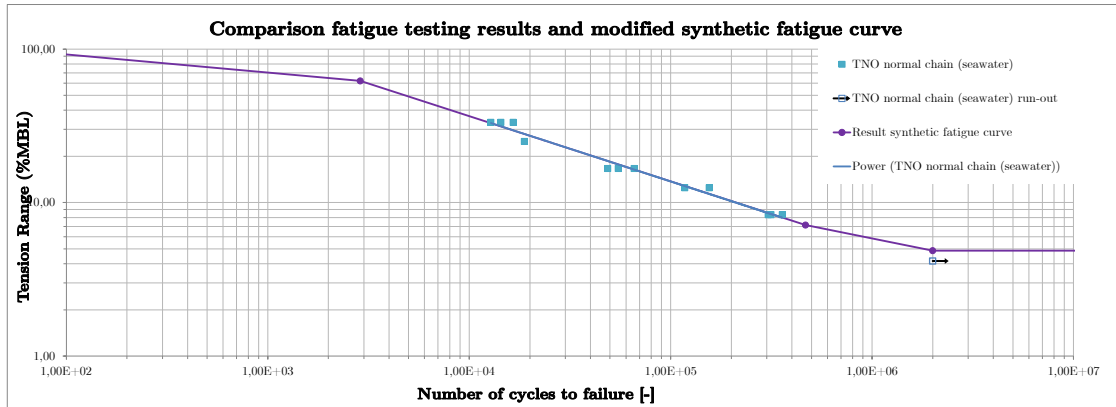


FIGURE 4.29: Comparison between the modified synthetic fatigue curve and the fatigue testing results

slightly lower at 612.1 MPa. In terms of the stress gradient, which is used to determine the notch factor β_k , the slope of the Von Mises stress gradient is slightly higher than the slope of the y-stress gradient (84.0 versus 77.9 MPa mm⁻¹). When investigating a material component that is subject to a loading combination in multiple directions, one would need to move to other methods such as a multi-axial fatigue assessment (see e.g. Lee et al. (2012)). This increases the complexity of the analysis significantly and the analytical derivation of the fatigue curves as proposed by Gudehus (1999) is no longer valid.

TABLE 4.5: Results from the analytical derivation of the fatigue curve

Variable	Value	Unit	Variable	Value	Unit
α_k	1.37	—	F_{0Tk}	3.86	—
β_k	1.11	—	F_{break}	1200	kN
σ_{aD}	7.1	%MBL	F_m	0.71	—
$\sigma_{aDfictive}$	4.9	%MBL	F_T	0.44	—
σ_m	509	Nmm ⁻²	k	3.81	—
σ_t	943	Nmm ⁻²	m	2.35	—
σ_W	636	Nmm ⁻²	n	1.24	—
σ_{Wk}	165	Nmm ⁻²	N_D	553591	cycles
χ^*	0.11	mm ⁻¹	M	0.35	—
$2k - 1$	3.69	—	R_e^*	62.0	%MBL
F_0	0.52	—	R_m^*	159	%MBL
F_{0T}	0.26	—	R_z	250	μm

4.4.1 Fatigue Curve Predictions

As the synthetic fatigue curve has now been established for one mean tension ($F = 250\text{kN}$), one can start to make predictions to quantify the effects of different mean tensions. With the RFID-system up and running (further explained in Section 4.5.2), a

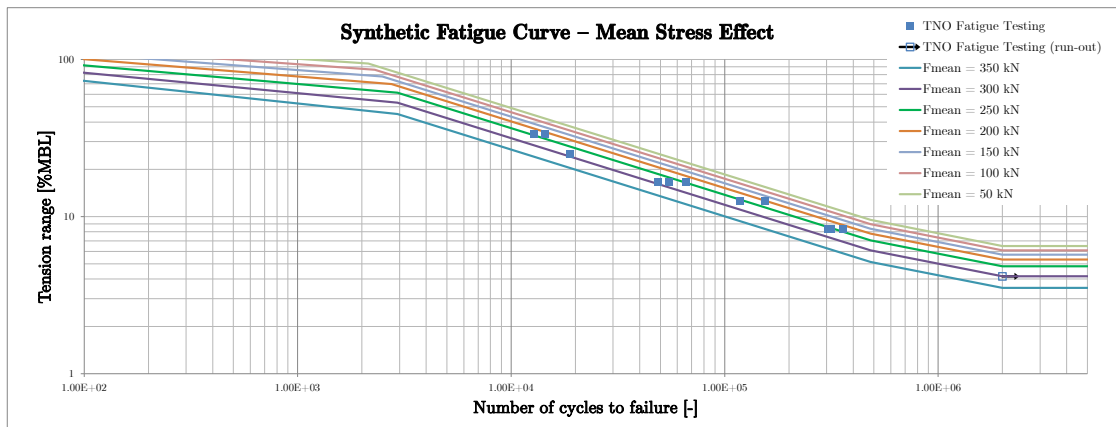


FIGURE 4.30: Effect of mean stress on position of synthetic fatigue curve

different fatigue curve can be used for each chain string, as they all experience different mean tensions. Figure 4.30 shows the effect of different levels of mean tension and how it relates to the fatigue testing results. Another effect which can be investigated by means of the synthetic fatigue curve is the influence of corrosion. During the fatigue testing, corrosion was incorporated by means of bags of seawater around the chain. In the analytical derivation of the fatigue curve, the surface roughness factor might give an indication to what happens when the material corrodes. As the material corrodes, the surface roughness increases, making it easier for the cracks to initiate. In the process that follows, the crack-propagation phase, corrosion will have a negative effect on the fatigue life, also at stresses below the original endurance limit. However, the corrosive effects during the crack-propagation phase can not be directly attributed to the surface roughness. The surface roughness factor can therefore be used only to describe the effects of corrosion during the crack initiation phase. The synthetic fatigue curve for different levels of surface roughness can be seen in Figure 4.31.

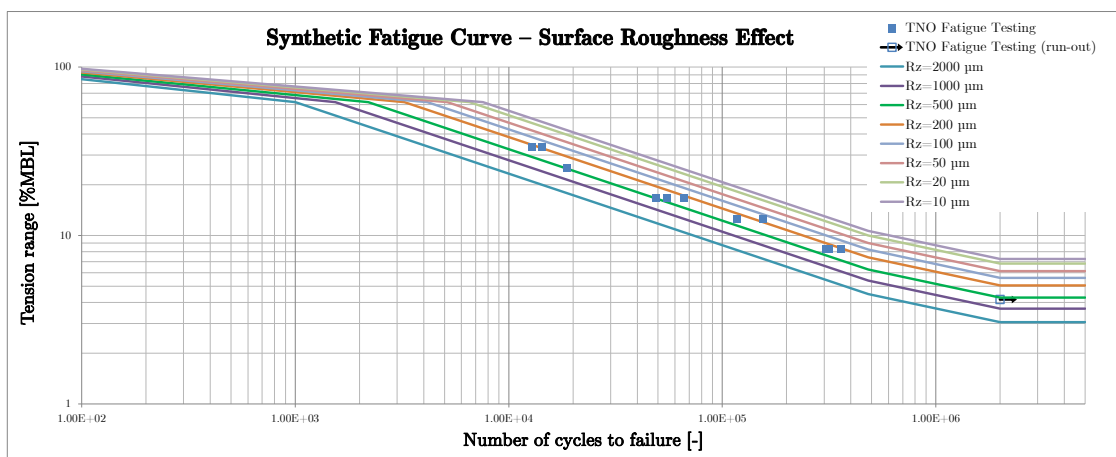


FIGURE 4.31: Effect of surface roughness on position of synthetic fatigue curve

4.5 Fatigue Predictions

In the previous sections, the OrcaFlex loading scenarios have been evaluated and fatigue curves have been established through Finite Element Modeling, fatigue testing experiments and an analytical design process. By coupling the fatigue curves to the tension profile over the length of the Flexible Fall Pipe, one can make predictions about how the fatigue progresses along the Flexible Fall Pipe. These predictions will be discussed in Section 4.5.1, followed by a description of the Radio Frequency Identification system in Section 4.5.2, which will monitor the chain fatigue. Section 4.5.3 will discuss how the safety factors should be applied and in Section 4.5.4 it is qualitatively described how the fatigue predictions change when operating in arctic conditions.

4.5.1 Fatigue Range Graphs

By coupling the results from OrcaFlex to the derived fatigue curves, predictions can be made about the level of fatigue throughout the Flexible Fall Pipe chains. Figure 4.32 shows the range graph for the scenario of 1000 meters, 4m significant wave height and no current. The level tension is plotted on the upper horizontal axis whereas the 1-hour

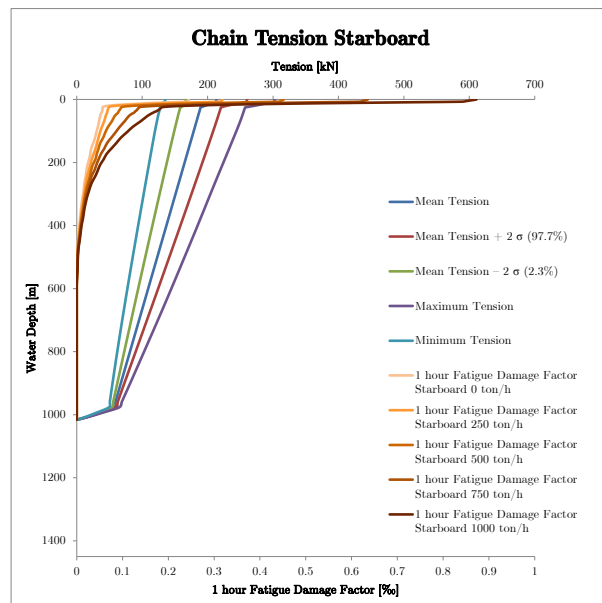


FIGURE 4.32: Fatigue damage factor for 1000m water depth, 4m significant wave height and no current

fatigue damage factor is plotted on the lower horizontal axis in permille ($\%$). For every section of the Flexible Fall Pipe, a different fatigue curve is applied as the mean stress in the chain links decreases towards the bottom of the Flexible Fall Pipe. As can be seen, the level of fatigue is highest at the top sections and it sharply decreases towards the bottom of the FFP in Figure 4.32. Starting from ± 400 meters the tension level

is below the endurance limit stress for this scenario, which results in a fatigue damage factor of zero. The fatigue damage factor is very high in the upper sections of the FFP as the mean level of the tension and the magnitude of the cycles increases sharply (due to the steel buckets). If one would linearly increase the level of tension from bottom to top, in accordance with the level of rock friction that is given by Figure 4.5, one can model the Subsea Rock Installation process. After this linear increase in tension, one can recalculate the fatigue damage factor. The effect of the rock friction is that the level of the fatigue is even more concentrated in the top sections, as these 'carry' all the rock friction, as shown by Figure 4.32.

4.5.2 Radio Frequency IDentification

Van Oord is currently working on the implementation of a Radio Frequency IDentification system. This involves tagging each chain string and Dominator connection link with a RFID-chip. This will give those component a unique number and by scanning the RFID-chip, one can get an overview of entire history of the component: manufacturing data, date when it was taken into use, etcetera. As the Flexible Fall Pipe is launched and recovered, a registration unit on the guidance structure scans each RFID-chip and links that to the onboard software system. For the onboard software system it is then clear what the location is of every component in the Flexible Fall Pipe, and for what period of time it has been in operation. In addition, the tension is measured in the top section of the Flexible Fall Pipe by the onboard measurement frame. By applying rainflow counting to the measured tension-time series, one can extract tension cycles. These tension cycles can be used in conjunction with the corresponding fatigue curve to calculate the fatigue damage factor. As only the tension in the upper sections of the Flexible Fall Pipe is measured, this tension can be scaled, in accordance with the findings of this thesis, to obtain an estimation of the tension profile in the rest of the Flexible Fall Pipe system. As the location of every Flexible Fall Pipe section is known by the RFID-system, the fatigue damage factor for every section can be incremented accordingly. As a result, one can make a prediction of the cumulative damage factor in every chain section. When this cumulative damage factor exceeds a predetermined value, the chain section is discarded and replaced with a new one. Furthermore, by performing fatigue testing experiments on the used chain links, one can verify the fatigue damage factor predictions and further increase the accuracy of this model.

4.5.3 Safety Factors

By applying the methodology that has been described in this thesis, it is possible to quantify the amount of fatigue that is present in the Flexible Fall Pipe chains by means

of the Fatigue Damage Factor. From a practical perspective, it is important to identify what an acceptable level of fatigue is and for what level of the Fatigue Damage Factor the chain should be replaced. Two methods for applying the fatigue safety factor γ_F will be discussed, and the safety factor γ_L for the Safe Working Load will be evaluated.

4.5.3.1 Fatigue Safety Factor

In the determination of the fatigue safety factor, it would first be useful to see if an answer can be provided by the literature, or more particularly: the norms for mooring chain. For a mooring component, the American Petroleum Institute (2008) states that a 2.5% probability of fatigue resistance exceedance should be applied. However, it is additionally stated that this practice is not followed precisely due to, inter alia, insufficient test data and lack of test data in the low tension regime where the fatigue damage is most severe. Furthermore, American Petroleum Institute (2008) states: 'The predicted mooring component fatigue life shall be at least 3 times the design service life of the mooring system.' Det Norske Veritas (2010) prescribes the following design equation for the Fatigue Limit State:

$$1 - d_c \cdot \gamma_F \geq 0 \quad (4.20)$$

In Equation 4.20, d_c is the characteristic fatigue damage accumulated as a result of cyclic loading and γ_F is the fatigue safety factor. For the fatigue safety factor γ_F the following values shall be used for mooring lines which are not regularly inspected ashore:

$$\begin{aligned} \gamma_F &= 5 \quad \text{when } d_F \leq 0.8 \\ \gamma_F &= 5 + 3 \left(\frac{d_F - 0.8}{0.2} \right) \quad \text{when } d_F > 0.8 \end{aligned}$$

In determining γ_F , d_F is the adjacent fatigue damage ratio, which is the ratio between the characteristic fatigue damage d_c in two adjacent lines taken as the lesser damage divided by the greater damage. If a mooring line is regularly inspected ashore, then Det Norske Veritas (2010) prescribes a safety factor of 3. Let us explore what it means to apply the fatigue factor of safety on the fatigue damage factor in accordance with Det Norske Veritas (2010).

Applying the Fatigue Safety Factor on the Fatigue Damage Factor By simply applying the fatigue safety factor on the fatigue damage factor, the amount of 'safety' that is achieved is highly non-transparent. Consider the following situation: a factor of safety of 5 on the Fatigue Damage Factor has been selected, i.e. when the chains reach a Fatigue Damage Factor of 0.2, they will be discarded and replaced by a new set. This approach is non-transparent as the factor of safety is applied on the Fatigue Damage

Factor directly, whereas it should be applied first to the fatigue curve. Firstly, in the derivation of the fatigue curve, the endurance limit is estimated. If this estimation is too high, the chain still fatigues and this is not taken into account when applying the factor of safety to the Fatigue Damage Factor. Secondly, one of the determinants in selecting the safety factor is the amount of spread on the fatigue tests. For tests with a high amount of spread, obviously a higher factor of safety should be applied.

Applying the Fatigue Safety Factor on the Fatigue Curve A better approach in determining the fatigue safety factor would be to first identify what the spread on the fatigue measurements is. There are methods, such as Gudehus (1999), by which it is possible to shift the fatigue curve, so as to obtain a certain exceedance curve, which is based on the spread of the measurement results. Figure 4.33 shows the measurements from the fatigue testing and the best fit line in blue, and an example of what an exceedance curve would look like. The exceedance probability can be determined based on, for instance, a cost-benefit analysis. By applying this method, also the endurance

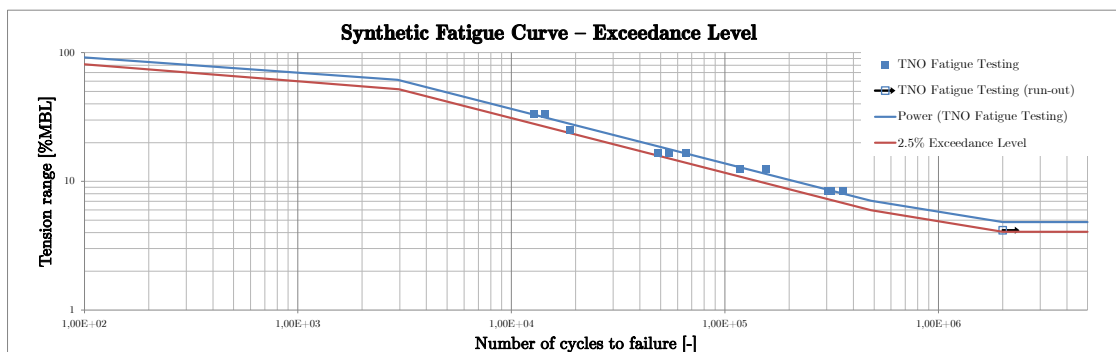


FIGURE 4.33: Example of 2.5% exceedance level fatigue curve

limit will shift downwards, as it is supposed to be. This corrected fatigue curve can be used for determining the Fatigue Damage Factor. On this Fatigue Damage Factor, one can apply a fatigue safety factor that takes into account the difference between the conditions of use and the fatigue testing conditions, plus some additional safety.

4.5.3.2 Safe Working Load and Safety Factor

Both Flexible Fall Pipe chain have a break load of 120 tonnes, which means that in theory, they could suspend a maximum load of 240 tonnes. With a safety factor γ_L of 3, the Safe Working Load (SWL) would be 80 tonnes. The current system is designed in such a way that when the combined chain loading exceeds 75 tons, measures are taken to reduce the loading. However, when the chains have already sustained an extensive amount of fatigue damage, the break load of the chain has probably reduced below 120 tonnes, and it questionable whether a safety factor γ_L of 3 still applies. One can get an

estimate of the break load of the chain link (after it has sustained fatigue damage) by using the fatigue curve in the low cycle fatigue range. However, it should be noted that no fatigue tests have been performed in the low-cycle fatigue range, which makes this merely an estimation.

4.5.4 Subsea Rock Installation in Arctic Conditions

As global energy demand rises, Offshore companies are moving further towards unexplored oil and gas fields in regions that experience Arctic conditions. Arctic conditions classify as those conditions in which snow, ice and low temperatures play a role, which is in fact already the case for operations for the coast of Norway in winter. Therefore, it is of importance to review the suitability of this FFP system for the Arctic conditions and specifically for the low temperature effect on the fatigue life of the chain. The design process for the analytical derivation of the fatigue curves from Section 4.4 does not take into account temperature, and low temperatures have not been investigated in the fatigue testing experiments. However, it is possible to make some qualitative statements based on the literature that is available on this subject, which has been discussed in Section 2.3.6. In a literature review (Stephen, 1982) on the subject of low temperature fatigue, a distinction has been made between high cycle and low cycle fatigue and notched and unnotched samples. The general conclusions for low temperature fatigue behavior in steels are that unnotched high-cycle fatigue strengths have consistently increased at low temperatures. The increased fatigue life can be attributed to the tensile strength and yield strength which generally increases at lower temperatures. Notched high-cycle fatigue strengths have substantially smaller increases at low temperature and in some cases small decreases were found. For low-cycle low temperature fatigue the unnotched and notched resistance can be increased, decreased or have little change. At low-cycle low temperature fatigue the effect of the reduced fracture toughness and reduced ductility plays a larger role, which explains the difference with high-cycle low temperature fatigue behavior (Stephen, 1982). Based on these results, it appears that, as long as the Flexible Fall Pipe chains operate in the high cycle fatigue range and they remain unnotched, then the low temperatures will most likely not have a negative effect on the fatigue life. It should be noted that the conclusions from Stephen (1982) are mainly based on fatigue testing results of which some are at very low temperatures (down to -196°), which is below the ductile-brittle transition temperature, whereas the operating temperatures of the Flexible Fall Pipe system go down to a minimum of -20° , which is still above this transition temperature.

Chapter 5

Discussion

First, this chapter goes briefly through the purpose of the study in Section 5.1, followed by a short overview of the methods and procedure in Section 5.2. Then, in Section 5.3 the major findings of this study are evaluated and finally the points of discussion are dealt with in Section 5.4.

5.1 Purpose of the Study

To remind the reader once again, the two main goals of this research are (1) to find out what the magnitude and configuration is of the external loading conditions during the Subsea Rock Installation process and (2) to gain more insight in the fatigue behavior of the Flexible Fall Pipe chains under these conditions. From thereon, predictions are made regarding the fatigue life of the chains, their replacement frequency and what measures could be undertaken to improve this system.

5.2 Methods and Procedures

To reach the goals of this study, this thesis uses a combination of numerical modeling, theoretical modeling and experiments. OrcaFlex, a marine dynamics program, is used to evaluate and quantify the global loading conditions that are present in the Flexible Fall Pipe system during the Subsea Rock Installation process. On a local scale, by means of a Finite Element Model in ANSYS, the actual chain links are studied when subjected to the different loading situations from OrcaFlex. Further, through an analytical design process, the fatigue curves of the chains are established under various conditions. These fatigue curves have been compared to real-life fatigue testing data which is obtained from fatigue testing experiments at TNO.

5.3 Major Findings

The major findings of this thesis are discussed in this section, i.e. the results of Chapter 4 are summarized: the OrcaFlex loading scenarios, the Finite Element Model results, the fatigue testing experiments results, the results from the analytical derivation of the fatigue curves and the fatigue range graphs.

OrcaFlex Loading Scenarios Results The main results from the OrcaFlex loading scenarios come from the distribution of the tension over the length of the Flexible Fall Pipe. This is shown in Figure 5.1 for a working depth of 1000m and 2m, 4m and 6m significant wave height and no current. The results show that the tension cycles increase

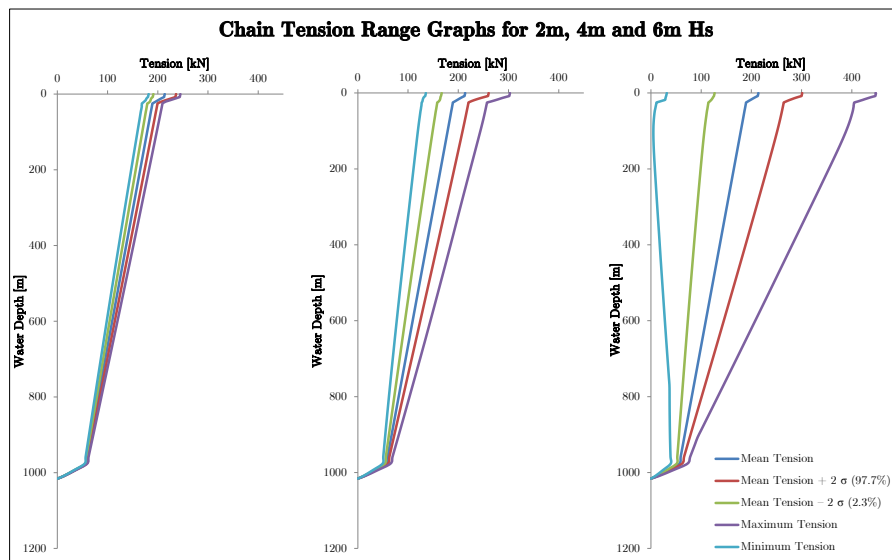


FIGURE 5.1: Effect of wave height on the chain tension - 1000m, 2m/4m/6m significant wave height, 0 m/s current

in magnitude for deeper waters and higher sea states. It was found that during the Subsea Rock Installation process the tension profile as shown in Figure 5.1 tilts to the right. The mean level of tension increases linearly over the Flexible Fall Pipe and a major tension cycle is induced as the Subsea Rock Installation is started or stopped. A similar major tension cycle is found during installation and recovery, when the chain links go from a state in which they are slack to a state of being tensioned. For the deepwater buckets, the tension profile over the length of the Flexible Fall Pipe is less steep than for the normal buckets, but the contact forces between the Flexible Fall Pipe and the Umbilical Moonpool Frame increase. These contact forces also increase for higher current speeds and when the current is more inline with the direction of movement of the FFPV. Further, two locations have been identified in which chain link rotations occur:

1. Maximum rotation of 6.6° on the winch. When the chain runs over the winch, this rotation is always present.
2. Maximum rotation of 3.7° in the moonpool. This rotation was found under a current distribution with a 1 year return period on the Ormen Lange field.

Finite Element Model Results The stress distribution has been analysed by means of a Finite Element Model and peak stresses were found in the inner bend region of the chain link, which is in line with the finding from e.g. Lassen et al. (2009). When

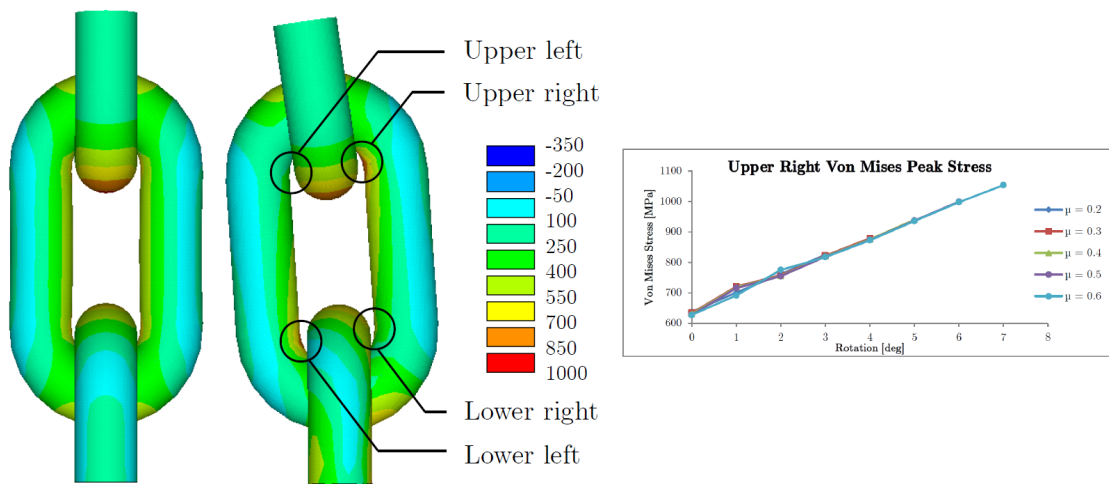


FIGURE 5.2: Stress distribution in the full chain link during axial loading and chain link rotations

the chain link rotates, the upper right and lower left Von Mises peak stresses increase whereas the lower right and upper left peak stresses decrease, as long as the chain links 'stick' under the effect of friction. As the critical rotation angle is exceeded, the chain links 'slip' and stress release take place. For a higher friction factor between the chain links, a higher critical rotation angle is found.

Fatigue Testing Results Fatigue testing experiments have been performed on three chain links in a tensile test bench at a frequency of 1 Hz and a constant amplitude sinusoidal load. Before testing, a bag of seawater was wrapped around the chain to incorporate the effect of corrosion. The results are plotted on a double logarithmic scale with tension range in percentage of the mean break load on the vertical axis and number of cycles to failure on the horizontal axis. The results from the testing experiments are shown in Figure 5.3 and indicated with the blue squares. The fatigue curves for the Dominator connection links have been plotted in the same figure by means of the orange triangles. As expected, the chain outperforms the Dominator connection links. The slope of the fatigue curve from the testing experiments shows good agreement with the

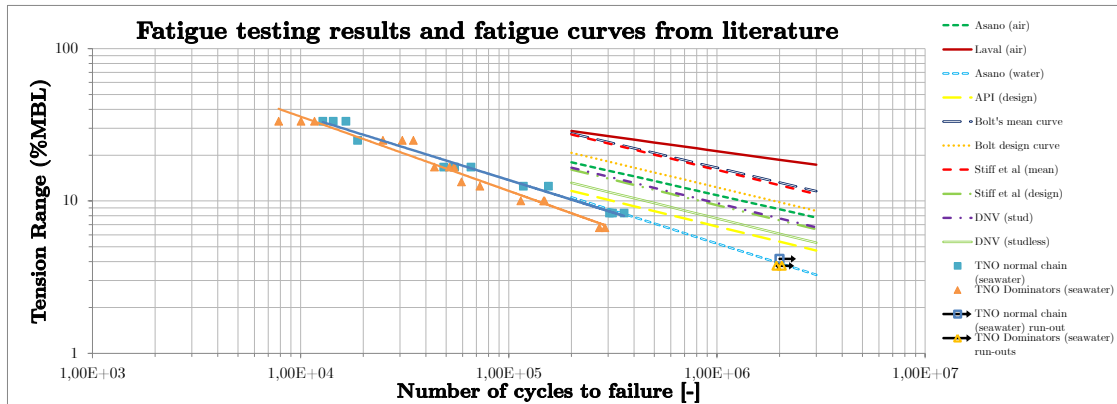


FIGURE 5.3: Fatigue testing results and fatigue curves from literature

slope from the fatigue curves from literature. However, the location of the fatigue curve that was found is low compared to the fatigue curves from literature. This could be (partly) attributed to the high mean load that was applied during the fatigue testing experiments.

Derivation of Fatigue Curves Results By applying the analytical design process from Gudehus (1999) in combination with the results from the fatigue testing experiments, fatigue curves for various conditions were derived. The main results come from the prediction of the fatigue curves in the ranges that were not tested: the low cycle fatigue life range, the infinite life range and the fatigue curves for different mean stresses. These predictions for the fatigue curves are shown in Figure 5.4, together with the results from the fatigue testing experiments which are indicated with the blue squares again. These fatigue curve predictions for different mean stresses are particularly useful for Flexible Fall Pipe chains, as for each chain section a different fatigue curve should be applied. To make this work in practice, it is required to implement a Radio Frequency Identification system (see Section 4.5.2) in combination with an accurate chain tension measurement frame.

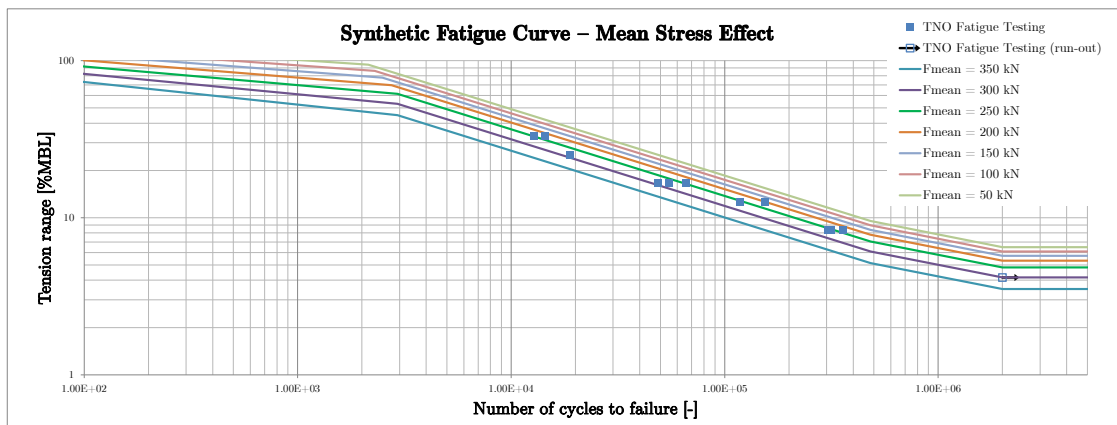


FIGURE 5.4: Effect of mean stress on position of synthetic fatigue curve

Fatigue Range Graphs When the results from OrcaFlex (tension profiles) are now coupled to the derived fatigue curves, one finds a fatigue range graph (Figure 5.5) that shows how the fatigue damage factor progresses along the Flexible Fall Pipe chains. The

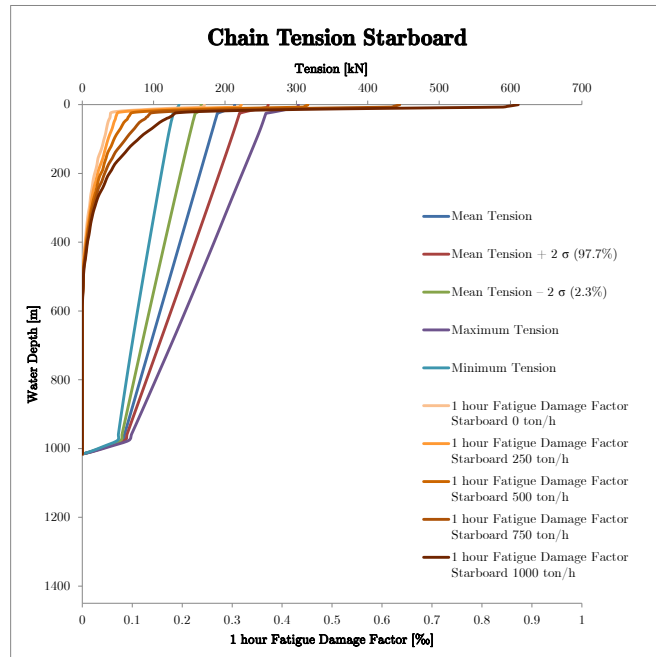


FIGURE 5.5: Fatigue damage factor for 1000m water depth, 4m significant wave height and no current

fatigue damage factor after one hour is plotted on the lower horizontal axis in permille (‰). The most left orange line from Figure 5.5 shows the level of fatigue when there is no Subsea Rock Installation. The fatigue damage increases sharply in the upper part of the Flexible Fall Pipe due to the presence of the steel buckets and the fact that the mean tension and tension cycles are largest in these sections. When the Subsea Rock Installation process is started, the fatigue damage shifts even more to the upper sections as the tension profile from Figure 5.5 tilts to the right during this process.

5.4 Discussion

This section will critically review the methodology that has been applied and it will discuss the shortcomings of this thesis. The points of discussion that are dealt with take the same order as in the Results section: OrcaFlex model (Section 5.4.1), Finite Element Model of the chain link (Section 5.4.2), fatigue testing of the chain link (Section 5.4.3) and the analytical derivation of the fatigue curves (Section 5.4.4).

5.4.1 OrcaFlex Loading Scenarios

This section evaluates the points of discussion from the OrcaFlex loading scenarios: the directionality of the hydrodynamic properties and the measurement data that was used during calibration of the model.

Directionality of the Hydrodynamic Properties OrcaFlex only supports uni-directional drag and added mass, irrespective of the direction or shape of the feature. When looking at the geometry of the buckets, it appears that the buckets are less streamlined in the upward direction compared to the downward direction. This difference in streamline could have an effect on the dynamic properties of the Flexible Fall Pipe and especially at the interface between steel and plastic (or deepwater) buckets.

Calibration of the Model As discussed in Section 4.1.1.1, there is a large amount of hysteresis in the tension measurement frame. From this observation, it was decided not to calibrate to the mean level of measured tension, but to have the mean level of tension follow from the addition of weights from the individual components of the FFP. The dynamic behavior *has* been calibrated based on this hysteric measurement data as it is for the FFP at present the best data there is. Furthermore, in this procedure the OrcaFlex model was calibrated based on the highest of two chain tensions that were measured. This might give an overestimation of the volatility of the tension cycles, which therefore gives an underestimation of the predicted fatigue life on deepwater projects.

5.4.2 Finite Element Model of the Chain Link

This section evaluates the points of discussion from the Finite Element Model: the proof loading of the chain link and the welded section in the chain link.

Proof Loading of the Chain Link During the manufacturing process of the chain, the chain links are proof loaded at 70.6% of the break strength, which causes the links to deform plastically (Deutsches Institut für Normung, 2012). When taken into operation the resulting residual stresses in the chain links are beneficial in terms of fatigue, as the applied loading first has to overcome the residual stresses (Celandar and Strom-Ljusne, 1972). This proof loading effect and the resulting stresses in the chain links are not taken into account in the Finite Element Analysis. However, this effect is (inherently) taken into account in the fatigue testing experiments and therefore also in the derived fatigue curves.

Welded Section in the Chain Link The weld on the straight section of the chain link is not taken into account in the Finite Element Analysis, whereas in 4 out of the 12 cases the chain link failed on the welded section during the fatigue test. It was found that the stresses on the straight section of the chain link are less severe than the peak stresses, but the material is locally weaker due to the weld. In all cases of fatigue failure at the weld, the number of cycles to failure remained in an acceptable bandwidth with respect to the other fatigue tests.

5.4.3 Fatigue Testing of the Chain Links

This section evaluates the points of discussion from the fatigue testing experiments: the corrosional effects during the fatigue testing and the varying mean loading during the fatigue testing experiments.

Corrosional Effects during the Fatigue Testing In the fatigue tests, a bag of sea-water is wrapped around the chain links to model the conditions of use more accurately. However, the fatigue tests are short compared to the lifetime of the chain, which could result in the corrosion not to take full effect. It has been reported in literature that corrosion can have an effect up to a factor of three on the fatigue life (Stiff et al., 1996). Still, the effect of corrosion is (partly) accounted for in the derivation of the fatigue curves by means of the surface roughness factor and by the extension of the fatigue curve in the infinite life region.

Varying Mean Loading during Fatigue Testing Another point of discussion in the fatigue testing experiments is that the mean level of the tension was not constant for all the fatigue tests. It was tried to model the conditions of use during the Subsea Rock Installation process. When rocks are installed in deeper water, not only does the mean level of the tension increase, but also the magnitude of the cycles. Therefore, for higher load cycles during the fatigue test, also the mean load was increased. Still, the difference in mean load remained in an acceptable bandwidth and the established fatigue curve slope shows good agreement with the results from literature. For the derivation of the fatigue curves, a better approach would be to perform the fatigue tests at a constant mean load.

5.4.4 Analytical Derivation of the Fatigue Curve

This section evaluates the points of discussion from the analytical derivation of the fatigue curves: the application of the peak stresses due to chain link rotations, the tension cycles in the low cycle fatigue range and the endurance limit.

Peak Stresses due to Chain Link Rotations This thesis has identified two locations where chain link rotations take place: at the Umbilical Moonpool Frame where the Flexible Fall Pipe leaves the vessel and on the guidance structure where the Flexible Fall Pipe is suspended. From the Finite Element Analysis it was found that these chain link rotations can increase the peak stresses by a factor 1.29-1.68 depending on the friction between the chain links. The design method that is used for the analytical derivation of the fatigue curves can only be applied when the loading is predominantly in one direction. For loading from multiple directions, which is the case during chain link rotations, one should apply a multi-axial fatigue assessment, such as a critical plane method or equivalent stress approach as put forward by Lee et al. (2012). Therefore, the synthetic fatigue curves cannot be applied in the two locations where the chain link rotations take place. In practice, a higher safety factor can be applied in the two locations where the chain link rotations occurs. Another option would be to create a point of suspension below the winch, possibly in combination with a heave compensator, which means that the winch is only used during installation and recovery. This is further discussed in Section 6.2.2.

Tension Cycles in the Low Cycle Fatigue Range This thesis works under the assumption that the tension cycles stay in the high-cycle fatigue range. However, the predictions from OrcaFlex show that this is not a valid assumption for the deeper water projects at high significant wave heights and high mean tensions (due to the SRI). Although the fatigue curve in the lower-cycle fatigue region is estimated, there is no test data to verify these predictions.

Endurance Limit In the fatigue testing experiments, merely one fatigue test classified as a run-out, which means that after $2 \cdot 10^6$ cycles the chain link still did not fail. Therefore, with only one test, the derived fatigue curves have no real experimental 'back-up' in the infinite-life region.

Chapter 6

Conclusion

This chapter will first discuss the goals of this thesis and how they have been achieved in the main conclusion of Section 6.1. The underlying conclusions are split up into two parts: conclusions from the loading scenarios and conclusions from the fatigue analysis. Then in Section 6.2, recommendations for further study are given and practical recommendations for the Flexible Fall Pipe system are discussed.

6.1 Conclusion

The goals of this thesis were (1) to find out what the magnitude and configuration is of the external loading conditions during the Subsea Rock Installation process and (2) to gain more insight in the fatigue behaviour of the Flexible Fall Pipe chains under these conditions. Through the combined interaction of a hydrodynamic model in OrcaFlex, a Finite Element Model in ANSYS and the derivation of fatigue curves through an analytical design process and fatigue experiments, a method has been established for the prediction of the fatigue damage factor in the Flexible Fall Pipe chains. Besides the use for this particular application, this method can fruitfully be used for other (mooring) chain systems in the maritime industry.

Real Time Fatigue Prediction From a practical sense, it can be concluded that the fatigue damage factor in the Flexible Fall Pipe chains can be predicted real-time onboard of the FFPV. This does require the use of a Radio Frequency Identification system for the Flexible Fall Pipe components and it is essential to have a measurement frame that accurately records the chain tension.

6.1.1 Conclusions from Loading Scenarios

The main conclusions from the loading scenarios are discussed in this section: the tension profile along the Flexible Fall Pipe, the tension profile and the Subsea Rock Installation process, the contact forces in the moonpool, the application of deepwater buckets and the possibility of a slacking chain.

Tension Profile along Flexible Fall Pipe It was found that the tension cycles and the mean level of tension decreases linearly along the Flexible Fall Pipe. The linear decrease is in correspondence with the weights of the particular sections of the Flexible Fall Pipe, i.e. sharper decreases for sections with steel buckets as compared to sections with plastic buckets. Further, the current appears to have a very limited influence on the tension profile along the Flexible Fall Pipe.

Tension Profile and Subsea Rock Installation Two effects take place due to the rock friction during to the Subsea Rock Installation process. First, the mean level of the tension increases linearly over the length of the Flexible Fall Pipe. This effect is largest for the upper sections, as these sections have to carry all the rock friction. Secondly, when applying rainflow counting, a major tension cycle is induced when going from the 'old' mean tension level to the 'new' mean tension level. The dynamics of the Flexible Fall Pipe system remain more or less unchanged during the Subsea Rock Installation process.

Contact Forces in the Moonpool The Flexible Fall Pipe system can come in contact with the Umbilical Moonpool Frame. The maximum contact force amounts to 10 tonnes and it was found during a current distribution with a return period of 1 year on the Ormen Lange field. The exact configuration of how the contact is established between the Flexible Fall Pipe and the Umbilical Moonpool Frame is difficult to predict with the used software packages. The main conditions for which the contact forces between the Flexible Fall Pipe system and the Umbilical Moonpool Frame increase are:

- Higher current speeds
- Higher wave heights; only when in combination with high enough current
- Lighter Flexible Fall Pipe system; the current 'shifts' the FFP more easily
- Current direction; higher forces when the current direction is opposite to the FFPV moving direction

Deepwater Buckets Under the assumption that deepwater buckets have the same hydrodynamic properties as the normal buckets, a linear decrease in mean tension over the length of the Flexible Fall Pipe is observed. This is beneficial in terms of fatigue. As the Flexible Fall Pipe is lighter, the contact forces in the moonpool increase under the effect of the current. Furthermore, the probability of a slacking chain becomes higher.

Slacking Chain It was observed that there is a 'critical seastate' or 'critical wave' for which the tension cycles become large enough to reach the level of zero tension (a slacking chain). The location where this phenomena manifests itself first is just below the top section of the Flexible Fall Pipe. The probability of the chain to go slack increases for higher seastates and for a lighter Flexible Fall Pipe.

6.1.2 Conclusions from Fatigue Analysis

The main conclusions from the fatigue analysis are discussed in this section: the causes of fatigue in the Flexible Fall Pipe chains, the distribution of fatigue over the length of the Flexible Fall Pipe chains and the effect of chain link rotations on the fatigue life of the chain.

Causes of Fatigue in the Flexible Fall Pipe Chains During the Subsea Rock Installation process, there are three main causes to the fatigue in the Flexible Fall Pipe chains: (1) the vessel motions, particularly the heave motion; (2) installation and recovery of the Flexible Fall Pipe and (3) the Subsea Rock Installation process. Firstly, tension cycles in the Flexible Fall Pipe chains are induced by the vessel motions, and the mean level and magnitude of these tension cycles increases mainly due to higher seastates and a longer Flexible Fall Pipe. These tension cycles are the most frequent. Secondly, during installation and recovery, the chain links on the winch go from a state of being slack to a sudden increase in tension of roughly 35 tonnes (on a project in 1000 meter water depth). This major cycle is induced for every time the Flexible Fall Pipe is deployed and recovered. The third cause of fatigue is every instance of starting and stopping the Subsea Rock Installation process, as this induces an additional major cycle. This happens several times during each deployment of the Flexible Fall Pipe. The magnitude of this cycle is usually between the tension cycles induced by the vessel motions and the major cycle due to the deployment of the Flexible Fall Pipe.

Fatigue Distribution along the Flexible Fall Pipe Chains The fatigue damage is concentrated in the upper part of the Flexible Fall Pipe chains and it decrease sharply as one moves down the Flexible Fall Pipe chains. This can be attributed to the high tension cycles and high mean tension in the upper part of the Flexible Fall Pipe chains,

and the logarithmic nature of the fatigue damage. For many cases, after a hundred or few hundred meters, the tension cycles drop below the endurance limit and the fatigue damage factor is zero. During Subsea Rock Installation, the fatigue damage will shift even more to the upper parts of the Flexible Fall Pipe, due to the linear increase in mean tension over the length of the Flexible Fall Pipe. Further, it was found that the fatigue damage increases rapidly with working depth and it increases rapidly with seastate.

Effect of Chain Link Rotations on Fatigue Life Two locations for which chain link rotations occur have been identified. First, a maximum rotation of 6.6° on the winch has been identified; when the chain runs over the winch, this rotation is always present. Secondly, a maximum rotation of 3.7° in the moonpool region has been identified; this rotation was found under a current distribution with a 1 year return period on the Ormen Lange field. During chain link rotations, the interlink friction causes the chain links to 'stick' (and build up stress) until a critical rotation angle is reached and the chain links 'slip' (and stress release takes place). During this sticking part of the chain link rotation, the peak stresses can increase by a factor 1.29-1.68, depending on the interlink friction. Therefore, these rotations are negative in terms of the fatigue life of chain, but the exact effect cannot be quantified with the current design methodology.

6.2 Recommendations

The Recommendations section has been split into two parts. First, Section 6.2.1 discusses the recommendations that are advised for further study. Secondly, the practical recommendations are dealt with in Section 6.2.2.

6.2.1 Recommendations for Further Study

The recommendations for further study are discussed in this section: the distribution of fatigue causes, the testing for the hydrodynamic properties of the buckets, a probabilistic study, the verification of the fatigue curves, duration of fatigue testing experiments, the further research into chain link rotations and the determination of the fatigue safety factor.

Distribution of Fatigue Causes This study has identified three main causes of fatigue: (1) the vessel motions, (2) the Subsea Rock Installation process and (3) the launching and recovery procedure. The predictions in this thesis are made mainly based on the first cause, the vessel motions, as it is assumed that these motions consume the largest part of the fatigue life of the chain. The other two causes occur much less

frequently, but the induced tension cycles can be of higher magnitude. Therefore, it is recommended to review historical data, to investigate what part of the fatigue life is consumed by each cause. This will then enable one to make more accurate predictions regarding the fatigue life of the chain on future projects and a better decision can be made on which of the three causes to mitigate. The new measurement frame for registering the chain tension (which is currently under instalment) could be fruitfully used.

Hydrodynamic Properties of the Buckets To get more insight into the hydrodynamic behavior of the buckets and to verify the OrcaFlex model it is recommended to perform full scale testing of the buckets in a water tank.

Probabilistic Study The approach that this thesis adopts is almost deterministic, as the analysed loading scenarios all have the same wave spectrum in OrcaFlex. At present, it is still unclear how the Flexible Fall Pipe system responds to certain combinations of wave heights, periods and directions. It could be very useful to look at this problem from a probabilistic approach to identify such 'critical' scenarios in terms of wave height, direction and period, and how this affects the dynamic behavior and the fatigue life of the chain.

Verify Derived Fatigue Curves It is recommended to perform further fatigue testing experiments to verify the established fatigue curves from the analytical derivation. The two main points on which this verification should focus on is (1) the verification of the established fatigue curves for different mean stresses and (2) the verification of the predicted endurance limit stress. The endurance limit stress is very important as the majority of the tension cycles takes place at and around this stress level. Further, it is recommended to perform re-tests of the run-out samples at a high amplitude load as this could give more information about the endurance limit at reasonably low testing effort. Besides performing fatigue testing experiments on new chain, it would also be useful to perform fatigue testing experiments on used chain to find out what the accuracy of the fatigue damage factor prediction is.

Duration of the Fatigue Testing Experiments For the fatigue testing experiments, a fatigue testing set-up is used which tests one sample of three chain links at a time. At a frequency of 1 Hz, the longest fatigue test lasted for roughly 23 days. It could therefore be useful to investigate the possibility of performing more fatigue tests at the same time. First, this could be done by performing the fatigue tests on multiple three chain link samples, which are coupled by means of Dominator connection links. Secondly, one could perform fatigue experiments on small samples that are taken from

the chain. For these small samples, one can easily run numerous fatigue tests simultaneously, which will give a much larger amount testing data. In the interpretation of the testing results one can make use of the Finite Element Model to take into account the peak stresses that are induced when normally testing the chain links. If the small samples show good agreement with the normal testing results of the chain links, the practical verification of the fatigue curves for different mean stresses will be made much easier.

Effect of Chain Link Rotations on the Fatigue Life From the Finite Element Analysis it became clear that chain link rotations can increase the Von Mises peak stresses by a factor of 1.29-1.68 depending on the level of friction between the chain links. As it is still unclear how these chain link rotations exactly affect the fatigue life of the chain, it could be useful to create a fatigue testing set-up which investigates these chain link rotations.

Determining the Fatigue Safety Factor It is recommended for further study to look into the determination of the fatigue safety factor γ_F as proposed by Gudehus (1999). This method has already been described qualitatively in Section 4.5.3.

6.2.2 Practical Recommendations

The practical recommendations for the Flexible Fall Pipe system are discussed in this section: the application of a heave compensator, making the Flexible Fall Pipe lighter, making the Flexible Fall Pipe more resilient, performing the fatigue experiments on an in-house fatigue test bench and rejection criteria of the chain link.

Applying a Heave Compensator The characteristic of fatigue is that failure occurs under a repetitive cyclic loading, at a level that is lower than the static break load. If one would reduce or eliminate this cyclic load, the fatigue problem would be tackled at its roots. By installing a heave compensator that compensates for the motions of the vessel, this is very beneficial to the fatigue life of the chain. Due to the logarithmic nature of the fatigue failure, if a heave compensator would reduce the cyclic loading by a factor 2, the chain fatigue life would increase by approximately a factor of 5. If a heave compensator would be applied that could damp out 80% of the vessel motions, in most of the cases, fatigue due to the motions is not an issue anymore, as the cyclic loading drops below the endurance limit. A heave compensator does not have an effect on the tension cycles that are induced by the Subsea Rock Installation process and those induced by installation and recovery of the Flexible Fall Pipe. It is recommended to install the heave compensator directly inline with the Flexible Fall Pipe, below the

winch and without the use of any guidance or sprocket wheels. The advantage of this inline configuration is that no peak stresses are induced due to the chain link rotations.

Making the Flexible Fall Pipe Lighter As discussed in Section 2.3.4, 'Effect of Mean Load on the Fatigue Life of Chain', the mean level of the cyclic load has a negative effect on the fatigue life of the chain. Therefore, by making the system lighter, this has a positive effect on the fatigue life of the chain. Clearly, the effect of a lighter system is not as convincing as a heave compensator, but it is still beneficial to the chain's fatigue life. To make the system lighter, one can think of many options, e.g. by using buckets with additional buoyancy, by using a smaller chain size for the bottom part of the FFP, by using an aluminium telescopic pipe and by using fewer steel buckets. When making the Flexible Fall Pipe lighter, one should keep in mind that this increases the contact forces in the moonpool and it increases the possibility for the chain to go slack.

Making the Flexible Fall Pipe System more Resilient The fatigue life of the chain can be increased by making the system more resilient to fatigue. This can be achieved by increasing the chain size, applying a higher proof load during the manufacturing process, using additional chains or by means of other methods. However, all these practical solutions still require one to make a prediction of the level of fatigue in the chain links to be able to know when to replace them. For that purpose, the RFID-system in combination with an accurate chain tension measurement frame is essential. As the replacement frequency of the chain links in deeper water becomes very high, it is recommended to investigate the possibility of using steel wire instead of chain links for suspension of the Flexible Fall Pipe. Steel wire has a higher strength to weight ratio compared to chain and therefore the steel wire outperforms the chain in terms of fatigue (Rossi, 2005).

Fatigue Test Bench At present, the fatigue testing experiments are executed on the fatigue test bench of TNO. With the substantial amount of fatigue experiments that will follow in the near future, it is recommended for Van Oord to look into the possibility of constructing or buying their own fatigue test bench, which could decrease the expenses considerably.

Rejection Criteria of the Chain Link It is recommended to establish a set of rejection criteria for the chain link, i.e. when a chain link satisfies one or more of the rejection criteria it should be discarded. These rejection criteria should at least take into account a maximum allowable level of fatigue damage, the maximum reduction of break load as a result of fatigue damage, a maximum lifetime period and a maximum amount of wear and tear.

Appendix A

System Overview

In this Appendix the different parts of the Flexible Fall Pipe system are shown, including information regarding dimensions, weights and other specifications. The same description order is used as in Chapter 2, which means the system is described from top to bottom. In Table A.1, an overview of the specifications of the Flexible Fall Pipe Vessel

TABLE A.1: Flexible Fall Pipe Vessel Stornes

Description	Value
Name	Stornes
Type	Flexible Fall Pipe Vessel
Classification	DP-2, ABS
Year of construction	2009
Dimensions	Length 175 m Width 26 m Moulded depth 14.5 m
Loading capacity	27000 tonnes
Cargo hold volume	24 200 m ³
Speed loaded	14.7 kn
Propulsion	2 x 4000 kW
Maximum working depth	1200 m
Total power installed	16 572 kW

Stornes is given and a side and top view of the Stornes is depicted in Figure A.1. The variables used for indicating the dimensions of the steel buckets, Dominator connection links and the round steel chain links are depicted in respectively Figures A.2 to A.4. The dimensions and other specifications of the buckets, Dominator connection links and the chain links are given in Table A.3. In addition, a chemical composition of the chain links from a spectral analysis is shown in Table A.2.

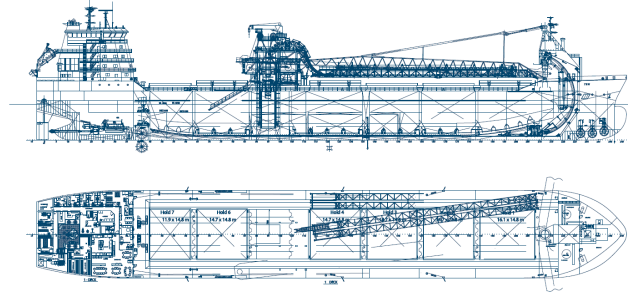


FIGURE A.1: Flexible Fall Pipe Vessel Stornes: side and top view

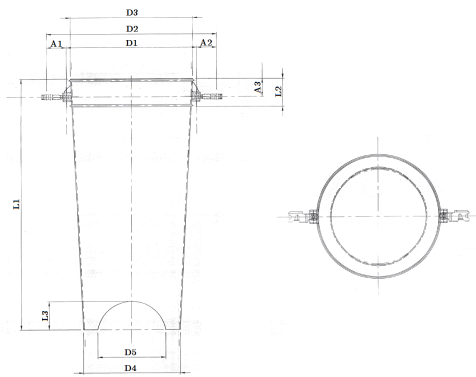


FIGURE A.2: Steel bucket: dimensions and geometry

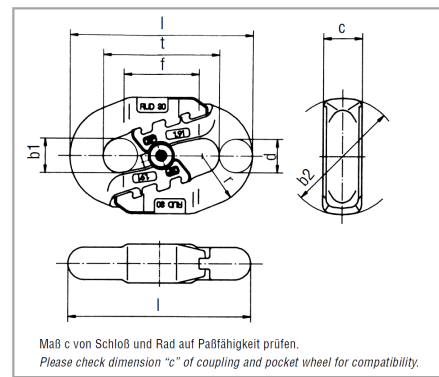


FIGURE A.3: Dominator connection links dimensions (RUD Ketten, 2012)

TABLE A.2: Round steel chain link: spectral analysis

Chemical composition as a percentage by mass								
C	Si	Mn	P	S	Cr	Mo	Ni	Al
0,213	0,212	1,3128	0,0084	0,0081	0,566	0,529	1,082	0,102 %

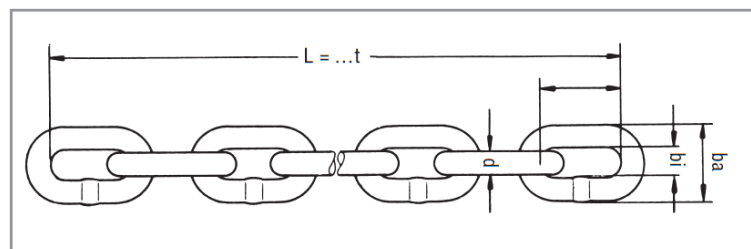


FIGURE A.4: Round steel chain link: dimensions and geometry (RUD Ketten, 2012)

TABLE A.3: Dimensions and specifications of the round steel chain link, Dominator connection link and the steel bucket

Round steel chain link				
Description	Item	Symbol	Value	Dimension
Dimensions	Diameter	d	30	mm
	Pitch	t	108	mm
	Inside width	bi	34	mm
	Outside width	ba	97	mm
Loading	Proof load		848	kN
	Break load		1200	kN
Hardness	Room temperature	leg	77	J
		crown	68	J
	0° C	leg	58	J
		crown	53	J
	-20° C	leg	42	J
		crown	39	J
Weight			18	kg m ⁻¹
Submerged weight			15.7	kg m ⁻¹
Surface finish			tectyl	
Dominator connection link				
Description	Item	Symbol	Value	Dimension
Dimensions	diameter	d	30	mm
	pitch	t	108	mm
		b ₁	32	mm
		b ₂	109	mm
		c	36	mm
		f	70	mm
		l	170	mm
		r	47	mm
Loading	break load		1200	kN
	break stress		850	N mm ⁻²
Weight			2.9	kg
Submerged Weight			2.5	kg
Steel bucket				
Description	Item	Symbol	Value	Dimension
Dimensions	diameter	D1	1150	mm
	diameter	D2	1500	mm
	diameter	D3	1100	mm
	diameter	D4	849	mm
	diameter	D5	600	mm
	length	L1	2225	mm
	length	L2	250	mm
	length	L3	250	mm
	distance	A1	175	mm
	distance	A2	175	mm
	distance	A3	162.5	mm
	effective length	L	1728	mm
	Weight	air		460
submerged			400	kg

Appendix B

Environmental Conditions

The Ormen Lange field is located 120 kilometers north-west of the Møre Coast, Mid-Norway, in water depths ranging from 800 to 1100 meters (Statoil, 2013). Van Oord is contracted to perform Subsea Rock Installation for depths up to 900 meters water depth. Figure B.1 indicates the approximate location of the Ormen Lange field. The Ormen



FIGURE B.1: Location of the Ormen Lange field (Google Maps, 2013)

Lange field is used in this research as the base case scenario. In Figure B.2 a scatter diagram of the annual distribution of the significant wave height and mean wave period for the Ormen Lange field is shown, whereas Figure B.3 shows the annual distribution of the significant wave height and the directional profile. The wave heights and periods for the loading scenarios which have been described in Section 3.3.1.3 are based on the information from Figures B.2 and B.3. The field operator of Ormen Lange, Shell, has done extensive field measurements to gather information about the distribution of the current distribution over the water depth. From these measurements, Shell has developed three extreme cases for the current distribution on which they base their design. These design cases will be used to investigate the effects of extreme current distributions on the fatigue life of the FFP chains. The return period of the design cases from Figure B.4 is one year.

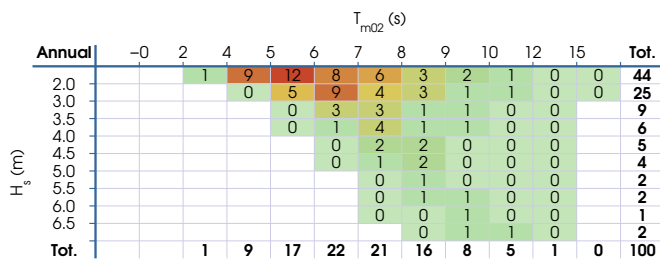


FIGURE B.2: Annual distribution of significant wave height versus mean wave period at the Ormen Lange field

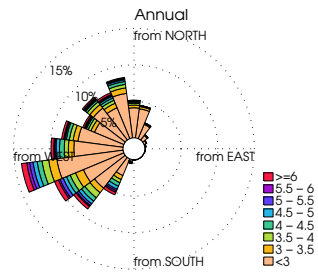


FIGURE B.3: Annual distribution of significant wave height and direction at the Ormen Lange field

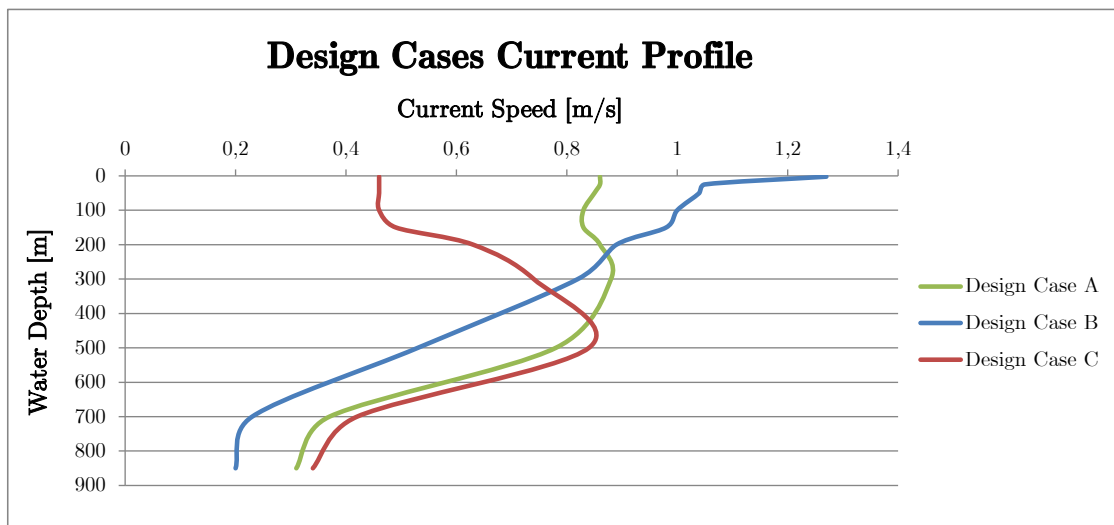


FIGURE B.4: Limit case current profiles at the Ormen Lange field

Appendix C

Theory

In this Appendix background theory for the different models is given. Section C.1 describes the main theory on which the OrcaFlex marine dynamics program is based on. In Section C.2 it is discussed how the nominal stress in the round steel chain link is calculated, which is applied for the analytical derivation of the fatigue curves in Section 4.4. Finally, the process of analytically deriving the fatigue curves is shown in Section C.3.

C.1 OrcaFlex Theory

OrcaFlex is a marine dynamics program developed by Orcina Ltd. for static and dynamic analysis of a wide range of offshore systems, including different types of marine risers, global analysis, moorings, installation and towed systems. The theory by which OrcaFlex runs its calculations is discussed in this section.

C.1.1 Global Theory

OrcaFlex performs 3D non-linear finite element time domain analyses. As OrcaFlex is a very visually based software, this section will shortly describe how the program works and what happens in the background. Before running the simulation in the time domain, OrcaFlex first performs a static analysis in which the initial positions and orientations of all objects in the model are calculated. The global equation of motion that OrcaFlex solves is the following:

$$M(p, a) + C(p, v) + K(p) = F(p, v, t) \quad (\text{C.1})$$

where $M(p, a)$ is the system inertia load, $C(p, v)$ is the system damping load, $K(p)$ is the system stiffness load and $F(p, v, t)$ is the external load. The variables p , v , a and

t are acceleration, velocity, position and time, respectively. The dynamic integration scheme within OrcaFlex recomputes the systems geometry at every timestep and takes into account all geometric non-linearities. For every free body and every line node, a local equation of motion is formed:

$$M(p)a = F(p, v, t) - C(p, v) - K(p) \quad (\text{C.2})$$

Equation C.2 is solved for the acceleration vector at the beginning of each time step for every free body and line node, and integrated to obtain the velocities and positions. At the end of each time step, the positions and orientations of all nodes and free bodies are again known and the process is repeated. These are, in short, the global working principles of OrcaFlex, which were obtained from Orcina (2012).

C.1.2 Environment Theory

OrcaFlex calculates the hydrodynamic loads on lines and buoys by using a modified version of Morison's equation, which is shown by Equation C.3.

$$F_w = (\Delta a_w + C_a \Delta a_r) + \frac{1}{2} \rho C_d A V_r |V_r| \quad (\text{C.3})$$

In Equation C.3, F_w is the fluid force, Δ is the mass of fluid displaced by the body, a_w is the fluid acceleration relative to earth, C_a is the added mass coefficient, a_r is the fluid acceleration relative to the body, ρ is the water density, V_r is the fluid velocity relative to the body, C_d is the drag coefficient and A is the drag area. Equation C.3 is used by OrcaFlex when calculating the effects of the hydrodynamic loading such as current and waves on a structure (Orcina, 2012).

C.1.3 Line Theory

OrcaFlex uses a Finite Element Model for a line as shown in Figure C.1. The line is divided into a series of line segments which are then modeled by straight massless segments with a node at each end. The axial stiffness and damping of the line is modeled by an axial spring and damper at the center of each line segment. Bending properties are represented by rotational springs and dampers and torsion can be modeled by a torsional spring and damper (Orcina, 2012).

C.1.4 Buoys, Shapes and Winches

In OrcaFlex, buoys can be used for various modeling applications. Besides the obvious one, the floating buoy, they are used for connecting objects together, transferring loads,

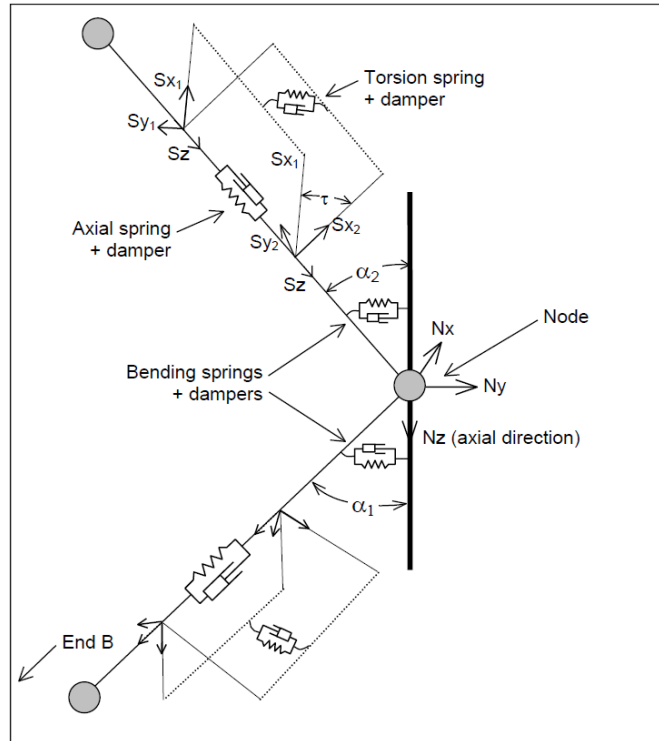


FIGURE C.1: OrcaFlex structural model (Orcina, 2012)

building complex structures or they can function as sea anchors, moving objects or for other purposes. There are two types of buoys available, the 3D-buoy with three translational degrees of freedom or the 6D-buoy with all six degrees of freedom. Additionally, OrcaFlex has other features for modeling purposes, such as shapes and winches. Shapes can be used to model the effects of contact and the effects of trapped water (e.g. in a moonpool). Winches are used to model constant tension or constant speed winches.

C.2 Nominal Stress in the Chain Link

In the process of establishing the synthetic fatigue curve in Section 4.4, it is required to obtain the nominal stress σ_{nom} at the location of the peak stress σ_{peak} . The peak stress location is found on the inner bend region of the chain link (at the cross section on the right side of Figure C.2). The nominal stress is calculated by means of Equation C.4, in which F is the external force, A is the cross-sectional area, M_b is the bending moment and W_b is the section modulus in bending.

$$\sigma_{nom} = \frac{F}{A} + \frac{M_b}{W_b} \quad (\text{C.4})$$

As the nominal stress in Equation C.4 is calculated for a circular cross-section, A reduces to $\frac{\pi}{4}D^2$ and W_b reduces to $\frac{\pi}{32}D^3$. When applying Equation C.4 to the cross-section on

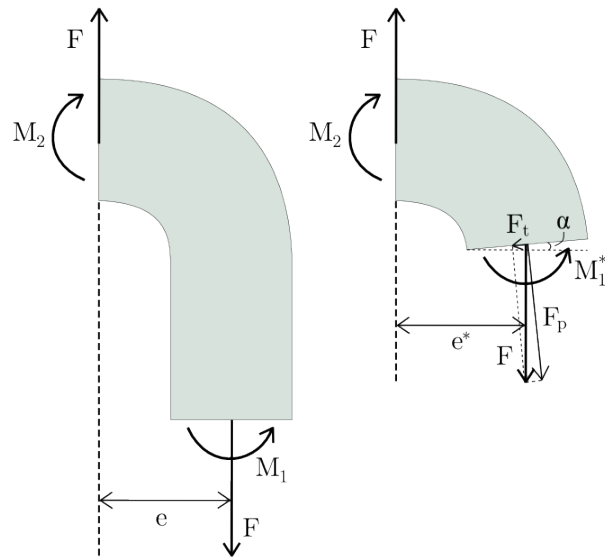


FIGURE C.2: Free Body Diagram of the chain link

the right side of Figure C.2, one obtains Equation C.5.

$$\sigma_{nom} = \frac{F_p}{\frac{\pi}{4}D^2} + \frac{M_1^*}{\frac{\pi}{32}D^3} \quad (\text{C.5})$$

In Equation C.5, the tension perpendicular to the cross-section T_p is found by $F_p = F \cos \alpha$. The moment M_1^* can be found by Equation C.6.

$$M_1^* = Fe^* + M_2 \quad (\text{C.6})$$

In Equation C.6, M_2 can be found by utilizing Equation C.7.

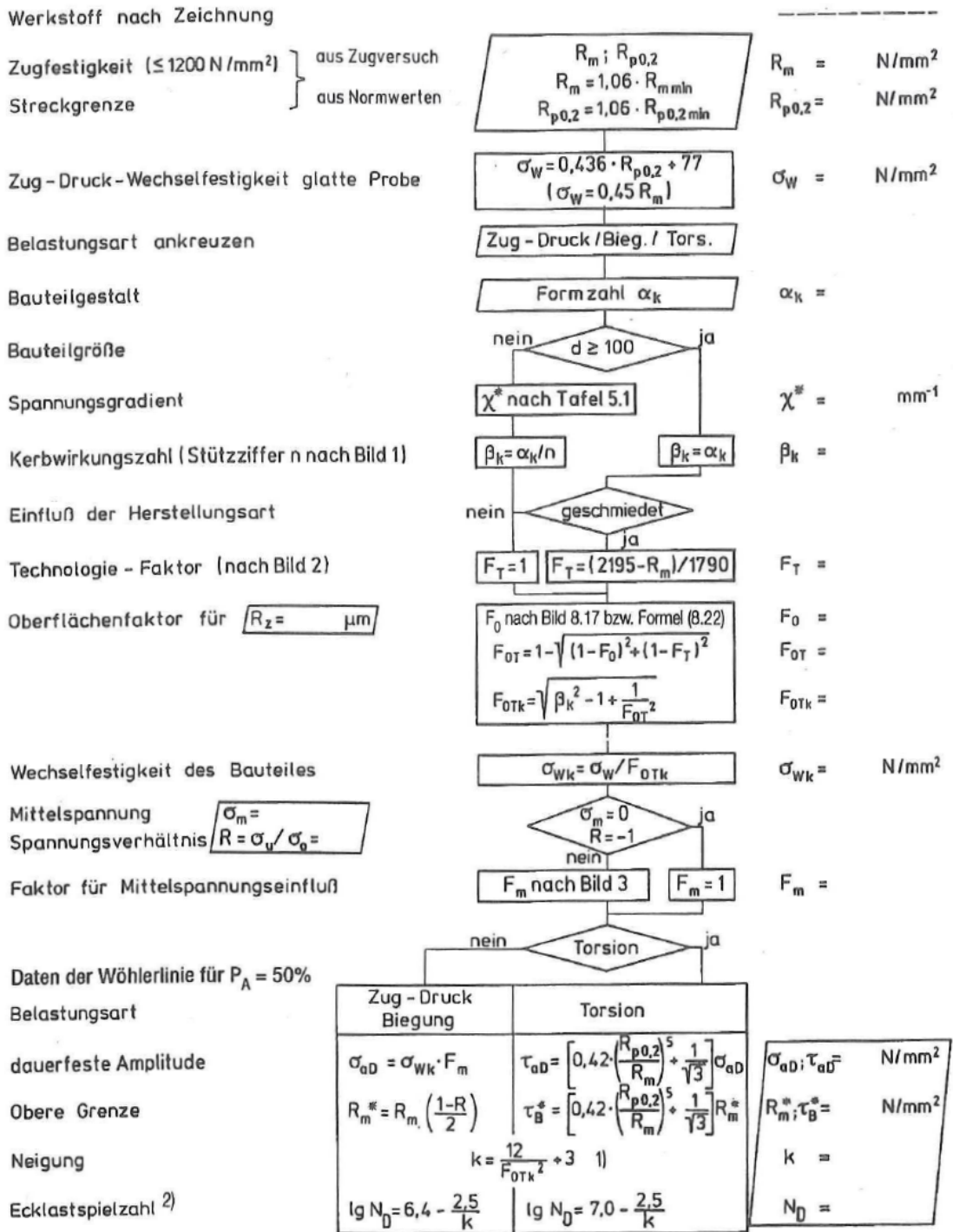
$$M_2 = M_1 - Fe \quad (\text{C.7})$$

M_1 is the last variable which is necessary to solve Equations C.5 to C.7 for the nominal stress σ_{nom} . At the location of M_1 in Figure C.2, one can obtain the stress distribution from the FEA in Section 4.2. One can find M_1 by calculating back from this stress-distribution using Equation C.4.

C.3 Analytical Derivation of the Fatigue Curve

The design process for the analytical derivation of the fatigue curve is depicted by Figure C.3.

Tafel 8.1: Berechnung der Wöhlerlinie für Bauteile aus **Stahl** (nach [8.14])



1) Nach neueren Erfahrungen kann die Neigung k bei Biegung steiler und bei Torsion flacher sein als nach dieser Beziehung.
 2) Bei Vergütungsstählen im Vergütungszustand tendiert N_D zu kleineren Werten

FIGURE C.3: Design process for the analytical derivation of the fatigue curve (Gudehus, 1999)

Appendix D

Results

This Appendix gives an overview of the results. First, three tables are presented that link to the figures in which the results are presented (these figures follow further on in this Appendix). Table D.1 gives an overview of the figures for the calibration and validation procedures, Table D.2 shows the figures that depict the general loading scenarios and Table D.3 presents the figures of the remaining loading scenarios. Finally, the results of the Finite Element Analysis can be found in Figure D.74, Figure D.75 and Figure D.76.

TABLE D.1: Results overview - calibration and validation

Calibration and Validation					
Time domain	Frequency domain	Water depth [m]	SRI rate [ton/h]	Variable	
Figure D.1	Figure D.12	240	0	Chain tension	
Figure D.2	Figure D.13	350	0	Chain tension	
Figure D.3	Figure D.14	350	1570	Chain tension	
Figure D.4	Figure D.15	350	0	Chain tension	
Figure D.5	Figure D.16	350	1600	Chain tension	
Figure D.6	Figure D.17	515	0	Chain tension	
Figure D.7	Figure D.18	515	1000	Chain tension	
Figure D.8	Figure D.19	815	0	Chain tension	
Figure D.9	Figure D.20	815	900	Chain tension	
Figure D.10	Figure D.21	827	0	Chain tension	
Figure D.11	Figure D.22	842	0	Chain tension	

TABLE D.2: Results overview - general loading scenarios

General Loading Scenarios				
Figure	Water depth [m]	Significant wave height [m]	Current speed [m/s]	Variable
Figure D.23	800	2	0	Chain tension and FDF
Figure D.24	800	4	0	Chain tension and FDF
Figure D.25	800	6	0	Chain tension and FDF
Figure D.26	800	2	0.2	Chain tension and FDF
Figure D.27	800	4	0.2	Chain tension and FDF
Figure D.28	800	6	0.2	Chain tension and FDF
Figure D.29	800	2	0.4	Chain tension and FDF
Figure D.30	800	4	0.4	Chain tension and FDF
Figure D.31	800	6	0.4	Chain tension and FDF
Figure D.32	1000	2	0	Chain tension and FDF
Figure D.33	1000	4	0	Chain tension and FDF
Figure D.34	1000	6	0	Chain tension and FDF
Figure D.35	1000	2	0.2	Chain tension and FDF
Figure D.36	1000	4	0.2	Chain tension and FDF
Figure D.37	1000	6	0.2	Chain tension and FDF
Figure D.38	1000	2	0.4	Chain tension and FDF
Figure D.39	1000	4	0.4	Chain tension and FDF
Figure D.40	1000	6	0.4	Chain tension and FDF
Figure D.41	1200	2	0	Chain tension and FDF
Figure D.42	1200	4	0	Chain tension and FDF
Figure D.43	1200	6	0	Chain tension and FDF
Figure D.44	1200	2	0.2	Chain tension and FDF
Figure D.45	1200	4	0.2	Chain tension and FDF
Figure D.46	1200	6	0.2	Chain tension and FDF
Figure D.47	1200	2	0.4	Chain tension and FDF
Figure D.48	1200	4	0.4	Chain tension and FDF
Figure D.49	1200	6	0.4	Chain tension and FDF
Figure D.50	1400	2	0	Chain tension and FDF
Figure D.51	1400	4	0	Chain tension and FDF
Figure D.52	1400	6	0	Chain tension and FDF
Figure D.53	1400	2	0.2	Chain tension and FDF
Figure D.54	1400	4	0.2	Chain tension and FDF
Figure D.55	1400	6	0.2	Chain tension and FDF
Figure D.56	1400	2	0.4	Chain tension and FDF
Figure D.57	1400	4	0.4	Chain tension and FDF
Figure D.58	1400	6	0.4	Chain tension and FDF

TABLE D.3: Results overview - other loading scenarios

Extreme Current Scenarios Results					
Figure	Water depth [m]	Significant wave height [m]	Current distribution	Variable	
Figure D.59	900	2	Distr. 1, 2, 3	UMF contact force	
Directional Current Profile Scenarios Results					
Figure	Water depth [m]	Significant wave height [m]	Current direction [°]	Variable	
Figure D.60	900	2	0, 90, 180	UMF contact force	
Subsea Rock Installation Loading Scenarios					
Figure	Water depth [m]	Significant wave height [m]	SRI rate [ton/h]	Variable	
Figure D.61	900	2	500	Chain tension	
Figure D.62	900	2	1000	Chain tension	
Figure D.63	900	2	1500	Chain tension	
Figure D.64	900	4	500	Chain tension	
Figure D.65	900	4	1000	Chain tension	
Figure D.66	900	4	1500	Chain tension	
Deepwater Buckets Scenarios Results					
Figure	Water depth [m]	Significant wave height [m]	Bucket type	Variable	
Figure D.67	1300	4	Both	UMF contact force	
Figure D.68	1300	4	Both	UMF contact force	
Figure D.69	1300	2	Deepwater	Chain tension and FDF	
Figure D.70	1300	2	Normal	Chain tension and FDF	
Figure D.71	1300	4	Deepwater	Chain tension and FDF	
Figure D.72	1300	4	Normal	Chain tension and FDF	
Vessel Loading Condition Scenario Results					
Figure	Water depth [m]	Significant wave height [m]	Vessel loading [%]	Variable	
Figure D.73	1200	4	25, 100	Chain tension	

D.1 Calibration and Validation Results

D.1.1 Time Series

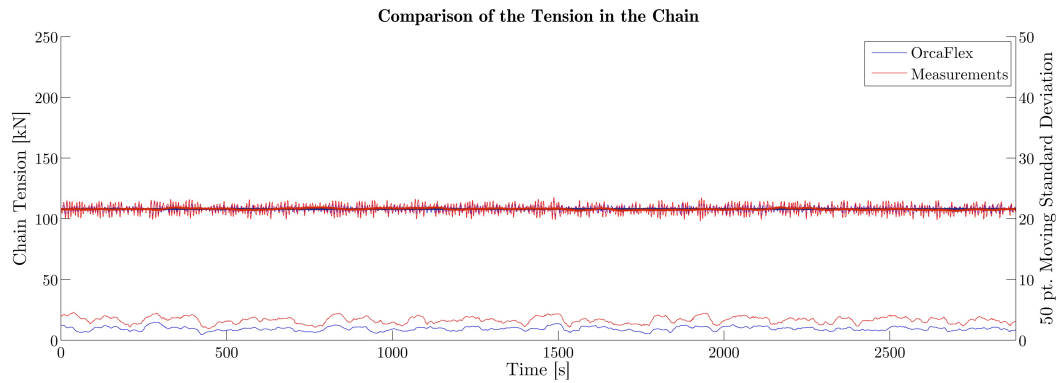


FIGURE D.1: Comparison of the Chain Tension for a water depth of 240m with no rock flow

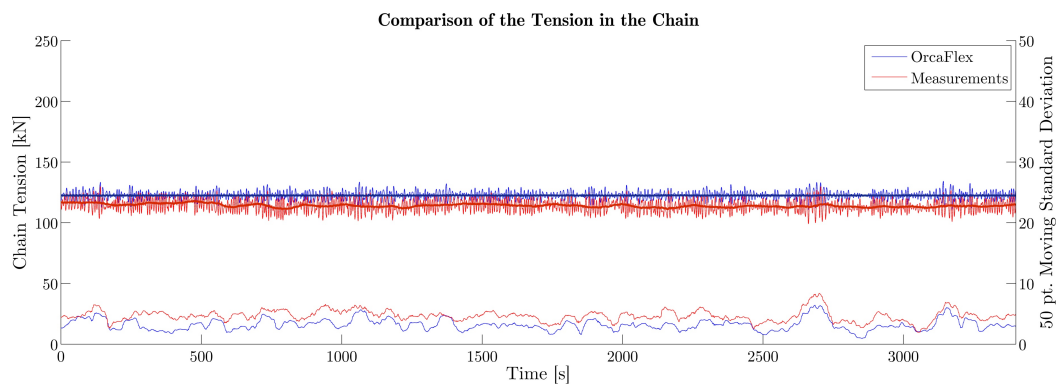


FIGURE D.2: Comparison of the Chain Tension for a water depth of 350m with no rock flow

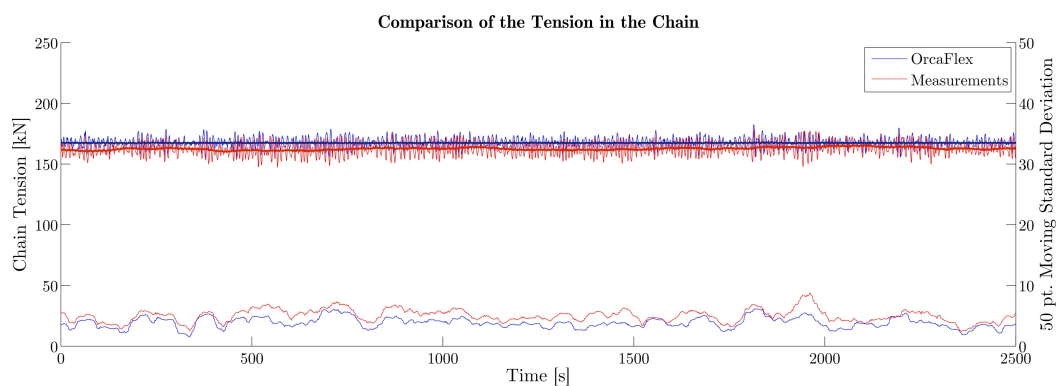


FIGURE D.3: Comparison of the Chain Tension for a water depth of 350m with a rock flow rate of 1570 te/h

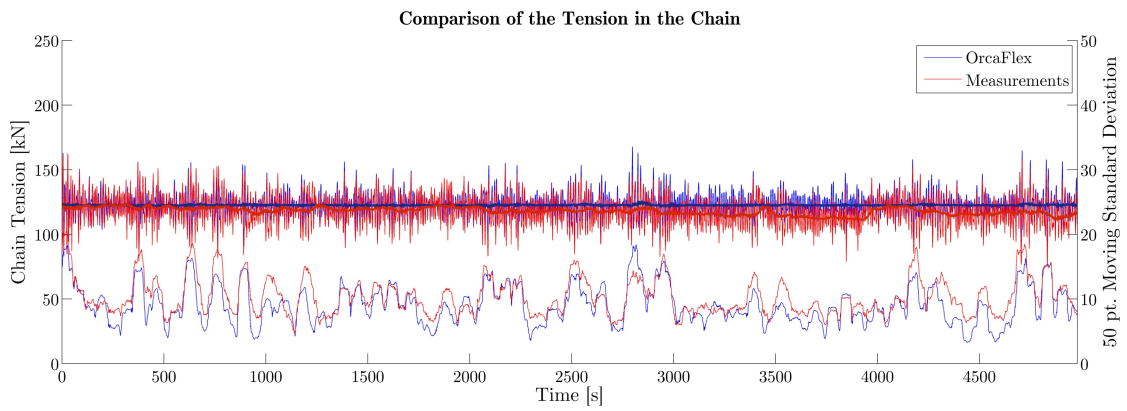


FIGURE D.4: Comparison of the Chain Tension for a water depth of 350m with no rock flow

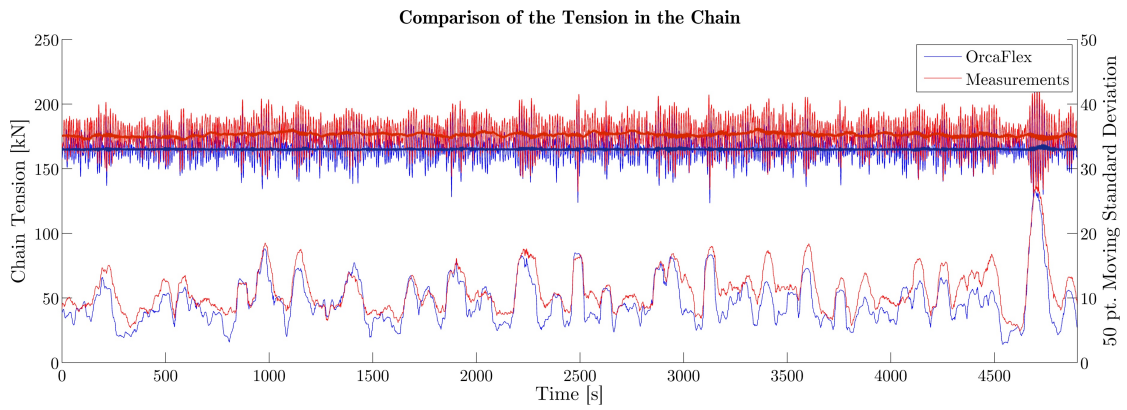


FIGURE D.5: Comparison of the Chain Tension for a water depth of 350m with a rock flow rate of 1600 te/h

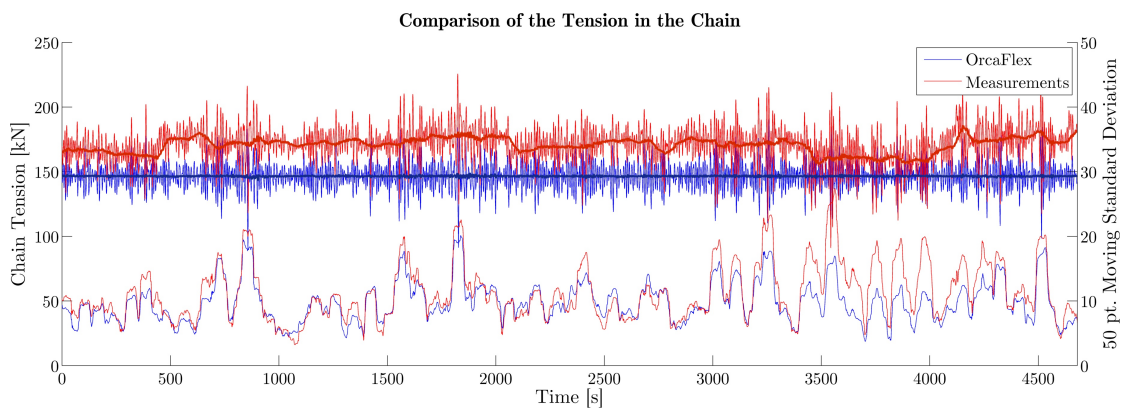


FIGURE D.6: Comparison of the Chain Tension for a water depth of 515m with no rock flow

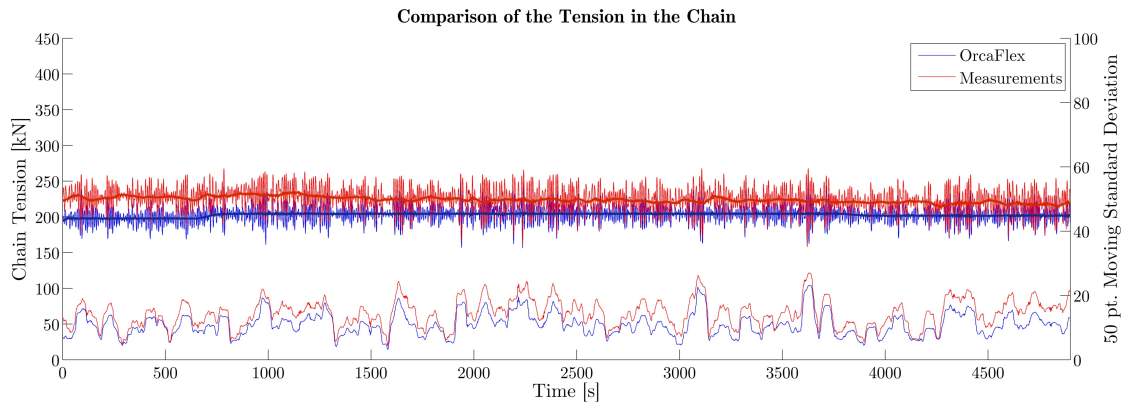


FIGURE D.7: Comparison of the Chain Tension for a water depth of 515m with a rock flow rate of 1000 te/h

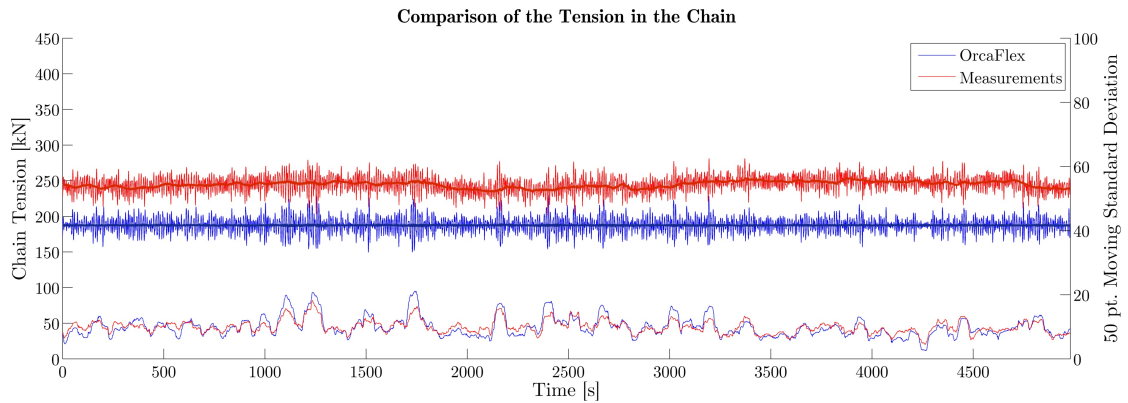


FIGURE D.8: Comparison of the Chain Tension for a water depth of 815m with no rock flow

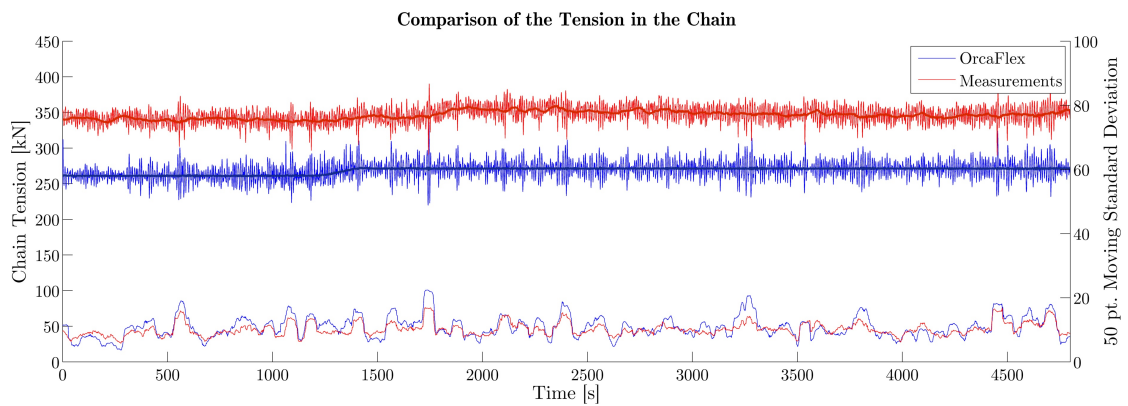


FIGURE D.9: Comparison of the Chain Tension for a water depth of 815m with a rock flow rate of 900 te/h

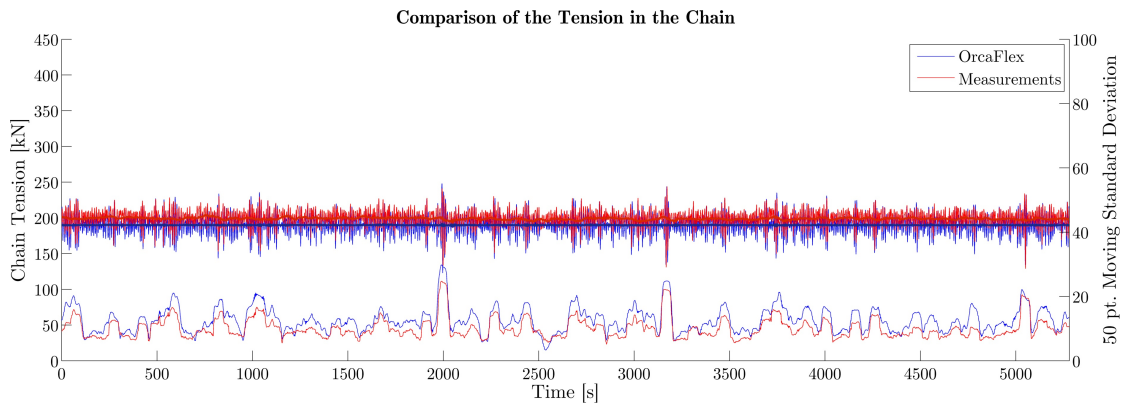


FIGURE D.10: Comparison of the Chain Tension for a water depth of 827m with no rock flow

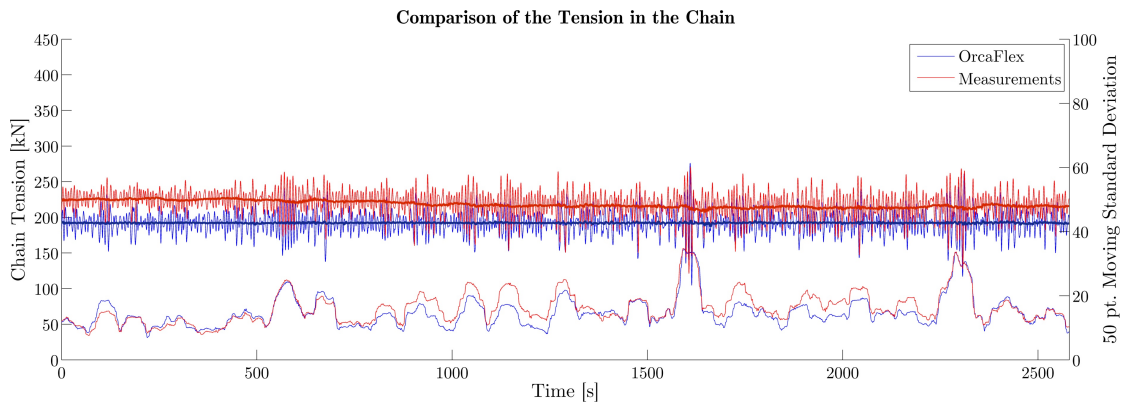


FIGURE D.11: Comparison of the Chain Tension for a water depth of 842m with no rock flow

D.1.2 Frequency Spectra

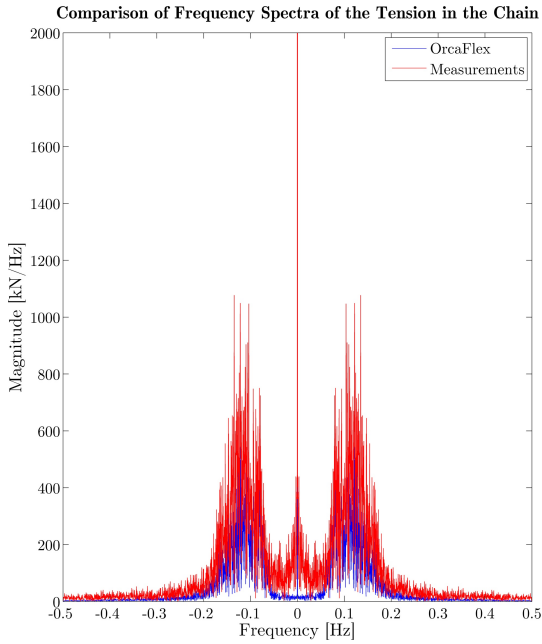


FIGURE D.12: Frequency Spectrum of the Chain Tension for a water depth of 240m with no rock flow

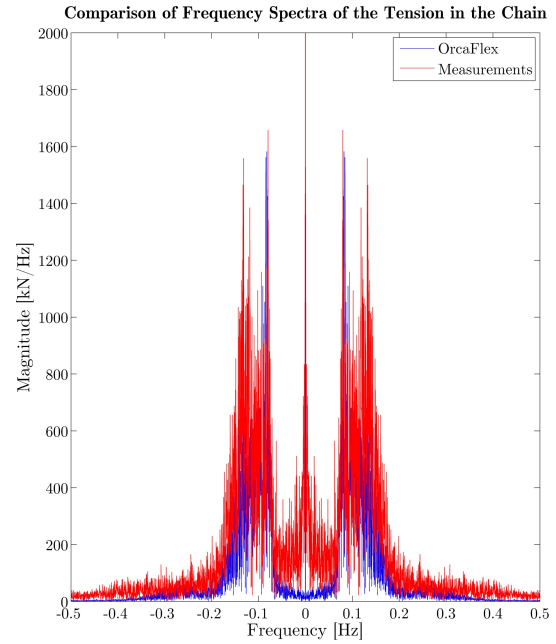


FIGURE D.13: Frequency Spectrum of the Chain Tension for a water depth of 350m with no rock flow

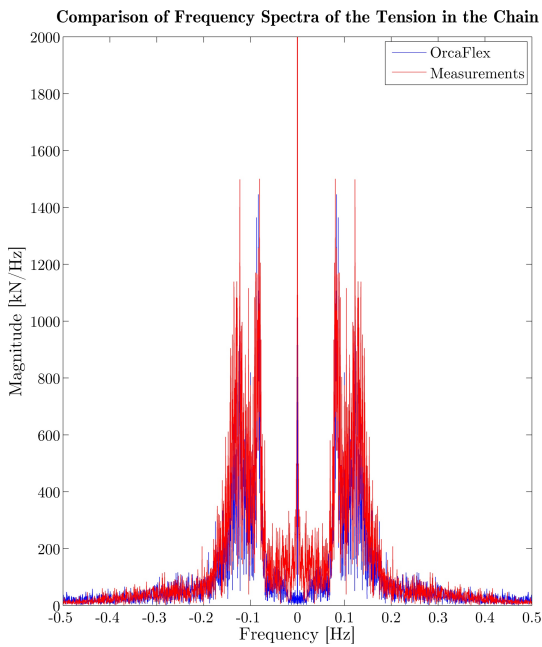


FIGURE D.14: Frequency Spectrum of the Chain Tension for a water depth of 350m with a rock flow rate of 1570 te/h

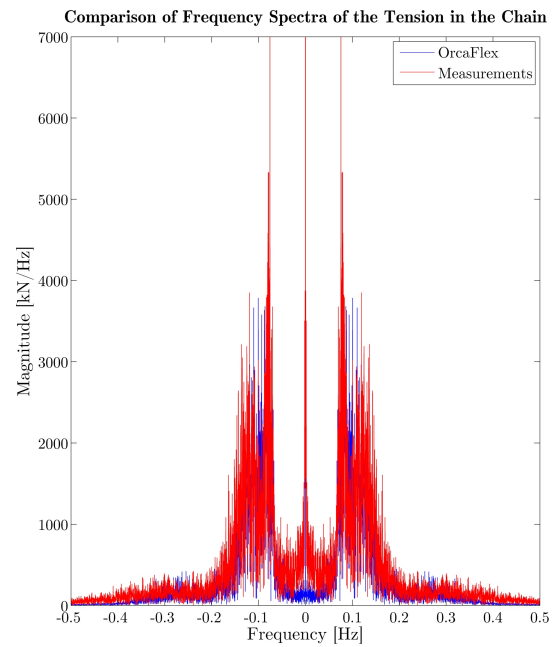


FIGURE D.15: Frequency Spectrum of the Chain Tension for a water depth of 350m with no rock flow

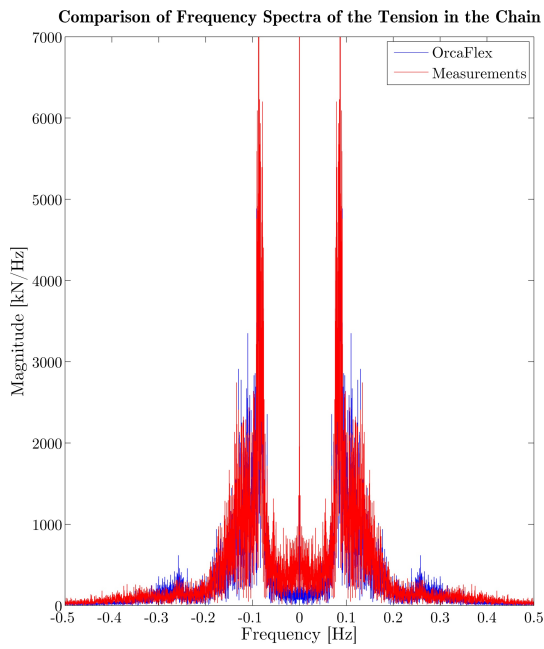


FIGURE D.16: Frequency Spectrum of the Chain Tension for a water depth of 350m with a rock flow rate of 1600 te/h

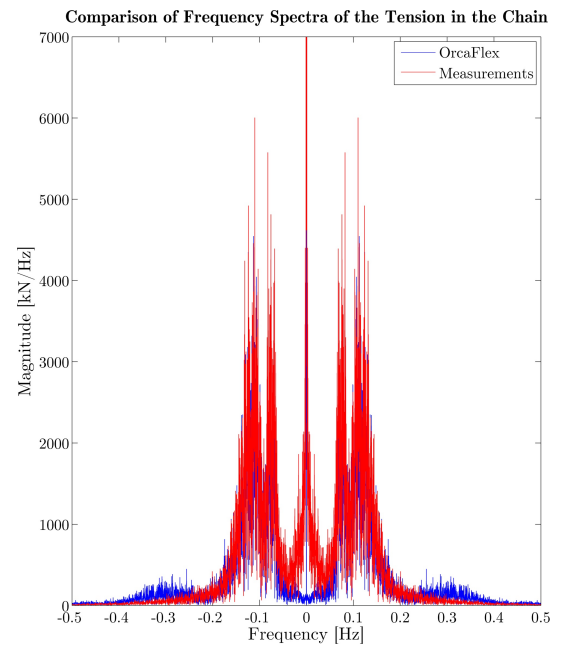


FIGURE D.17: Frequency Spectrum of the Chain Tension for a water depth of 515m with no rock flow

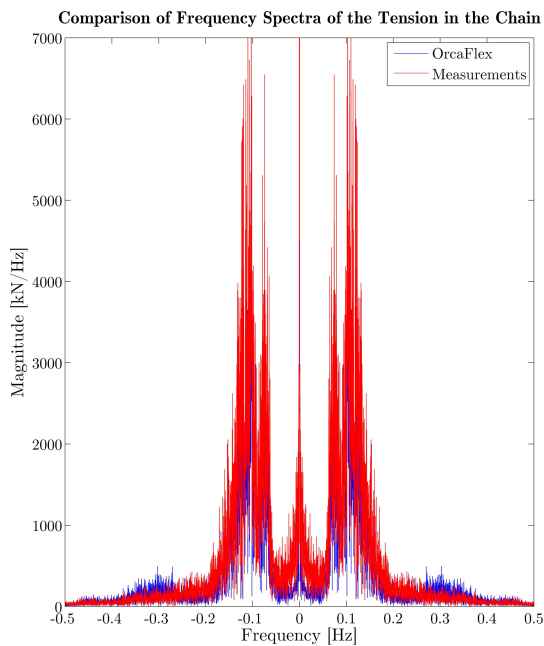


FIGURE D.18: Frequency Spectrum of the Chain Tension for a water depth of 515m with a rock flow rate of 1000 te/h

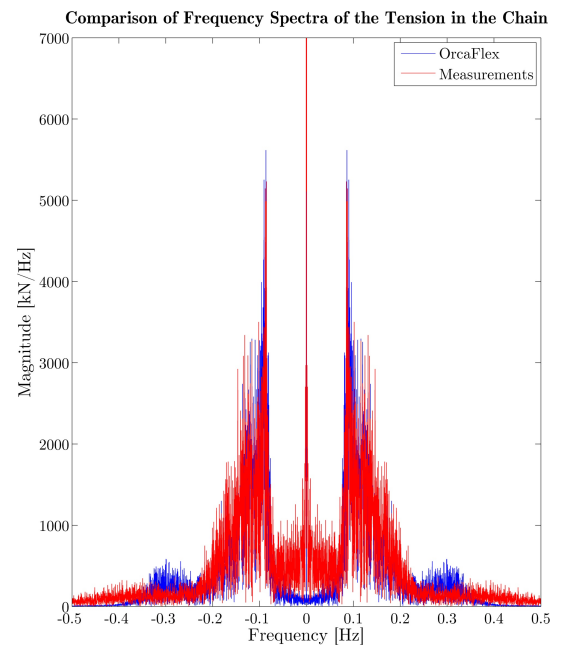


FIGURE D.19: Frequency Spectrum of the Chain Tension for a water depth of 815m with no rock flow

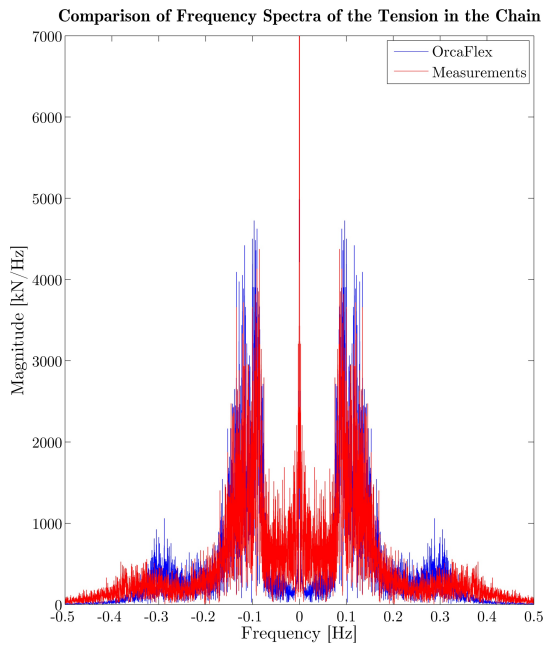


FIGURE D.20: Frequency Spectrum of the Chain Tension for a water depth of 815m with a rock flow rate of 900 te/h

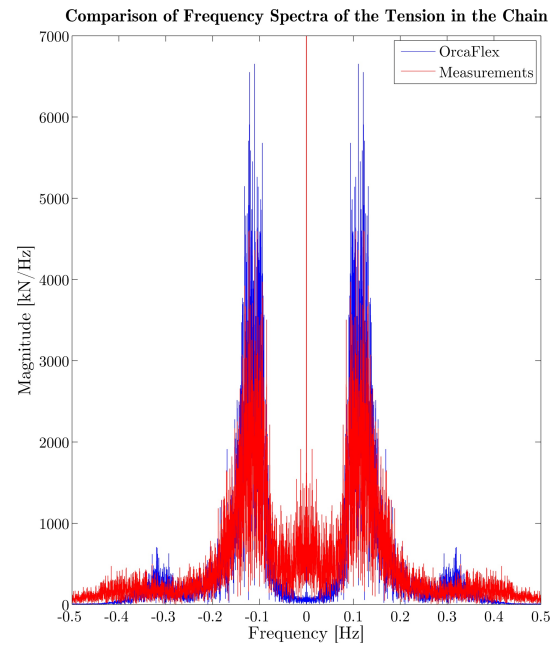


FIGURE D.21: Frequency Spectrum of the Chain Tension for a water depth of 827m with no rock flow

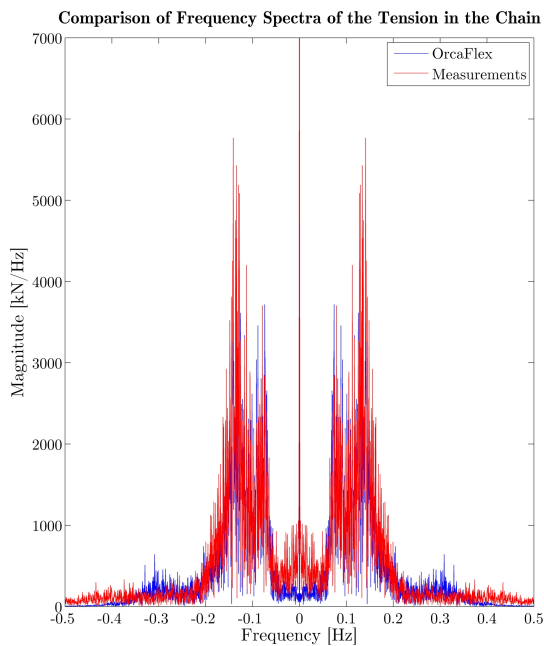


FIGURE D.22: Frequency Spectrum of the Chain Tension for a water depth of 842m with no rock flow

D.2 General Loading Conditions Results

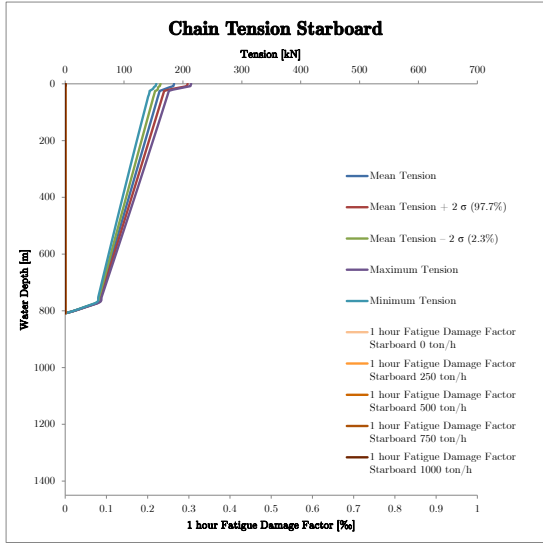


FIGURE D.23: Range graph for water depth of 800m, significant wave height of 2m and no current

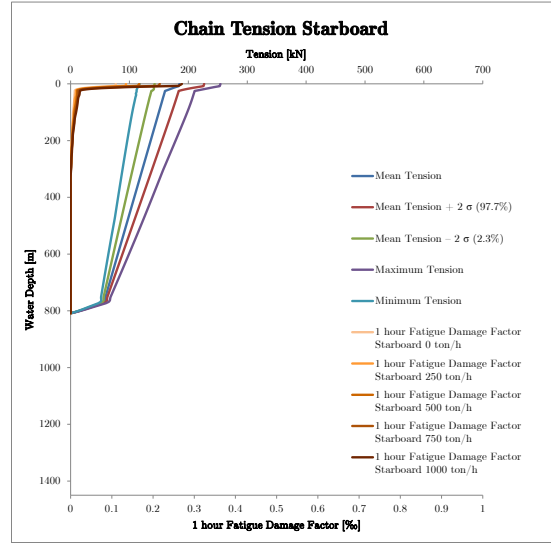


FIGURE D.24: Range graph for water depth of 800m, significant wave height of 4m and no current

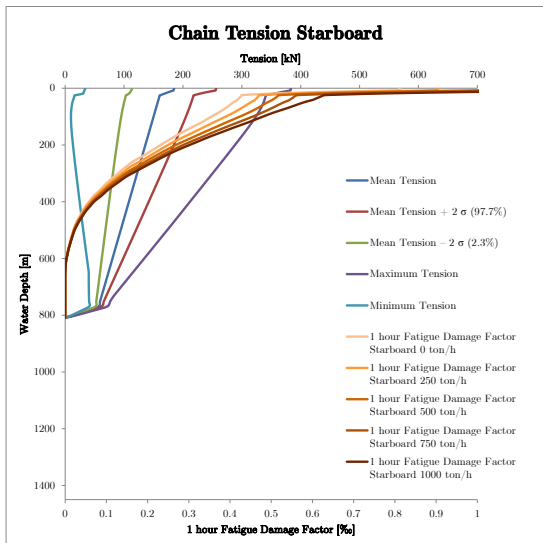


FIGURE D.25: Range graph for water depth of 800m, significant wave height of 6m and no current

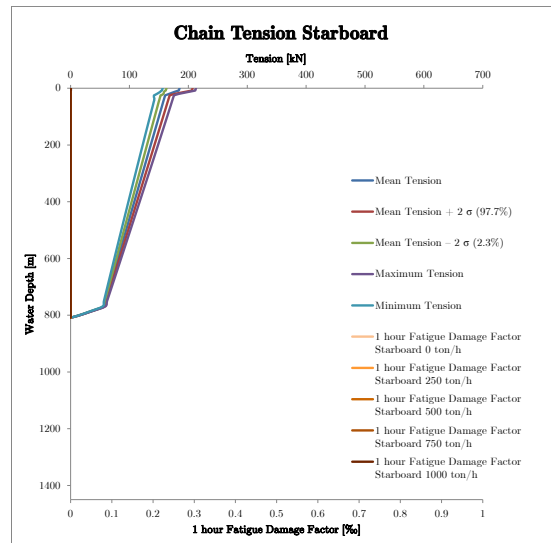


FIGURE D.26: Range graph for water depth of 800m, significant wave height of 2m and a current of 0.2 m/s

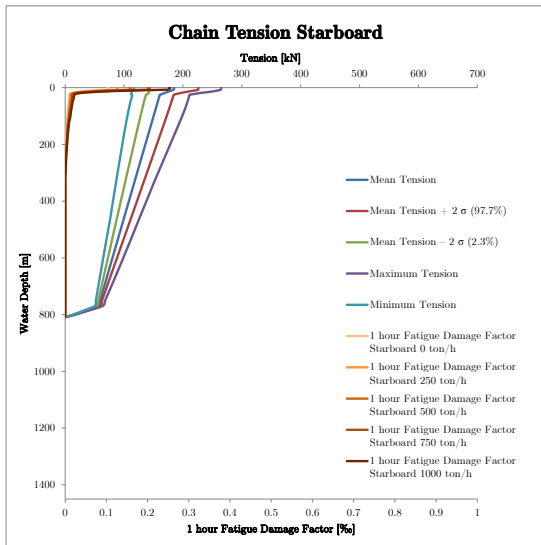


FIGURE D.27: Range graph for water depth of 800m, significant wave height of 4m and a current of 0.2 m/s

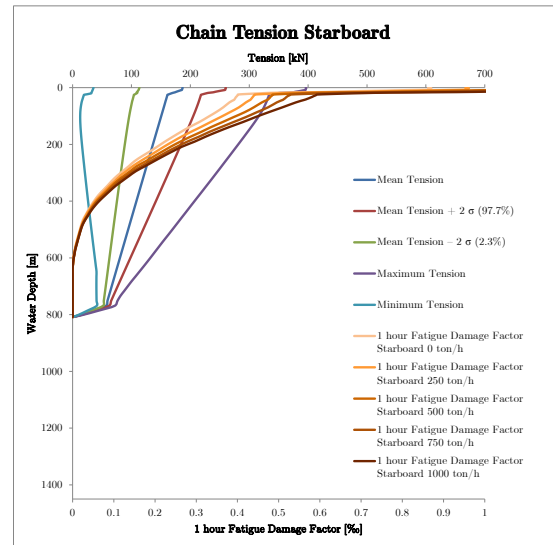


FIGURE D.28: Range graph for water depth of 800m, significant wave height of 6m and a current of 0.2 m/s

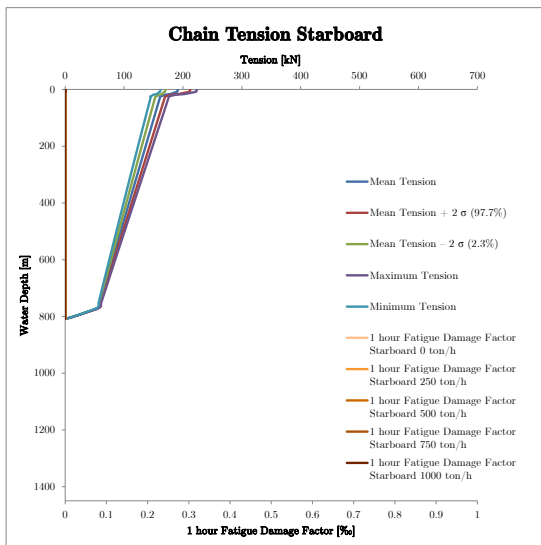


FIGURE D.29: Range graph for water depth of 800m, significant wave height of 2m and a current of 0.4 m/s

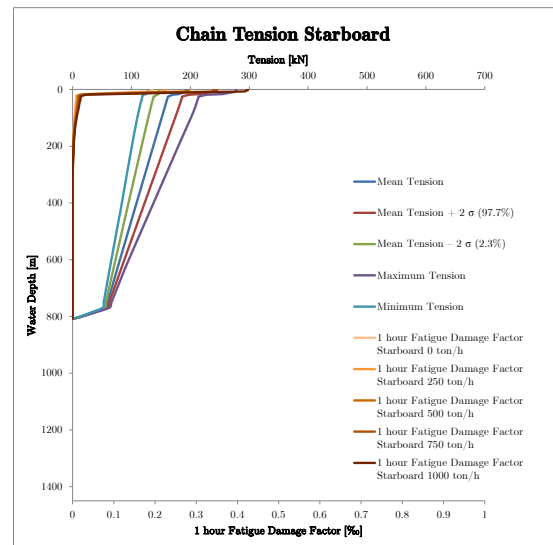


FIGURE D.30: Range graph for water depth of 800m, significant wave height of 4m and a current of 0.4 m/s

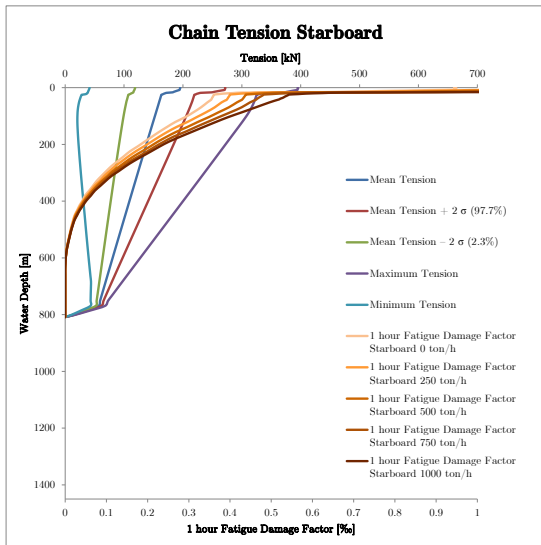


FIGURE D.31: Range graph for water depth of 800m, significant wave height of 6m and a current of 0.4 m/s

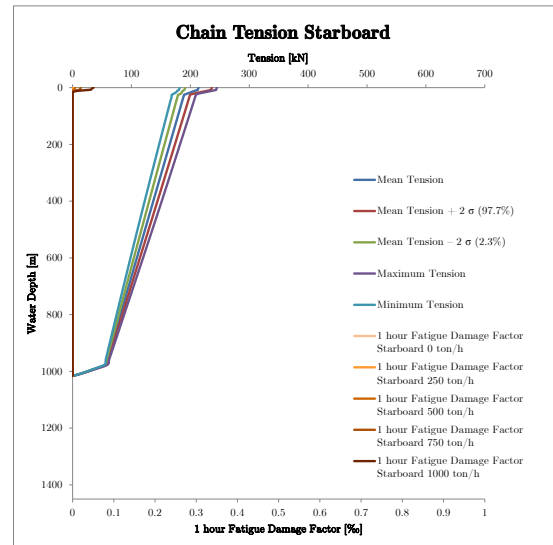


FIGURE D.32: Range graph for water depth of 1000m, significant wave height of 2m and no current

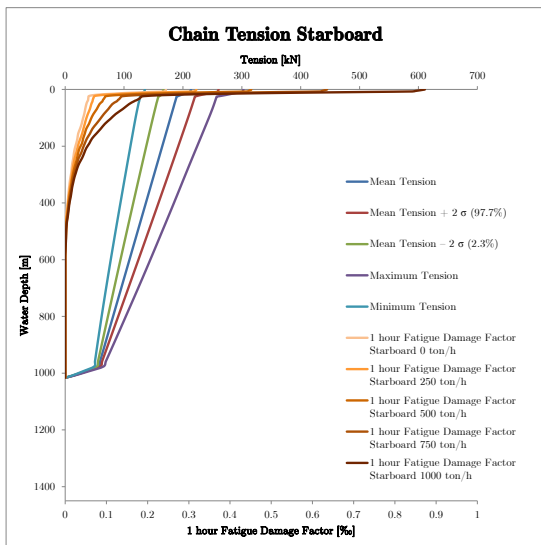


FIGURE D.33: Range graph for water depth of 1000m, significant wave height of 4m and no current

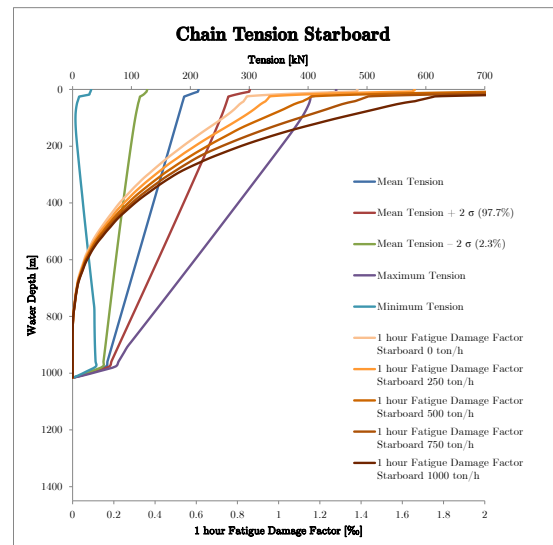


FIGURE D.34: Range graph for water depth of 1000m, significant wave height of 6m and no current

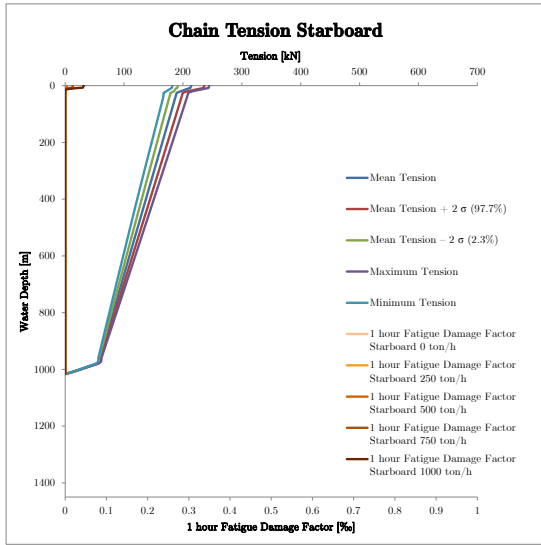


FIGURE D.35: Range graph for water depth of 1000m, significant wave height of 2m and a current of 0.2 m/s

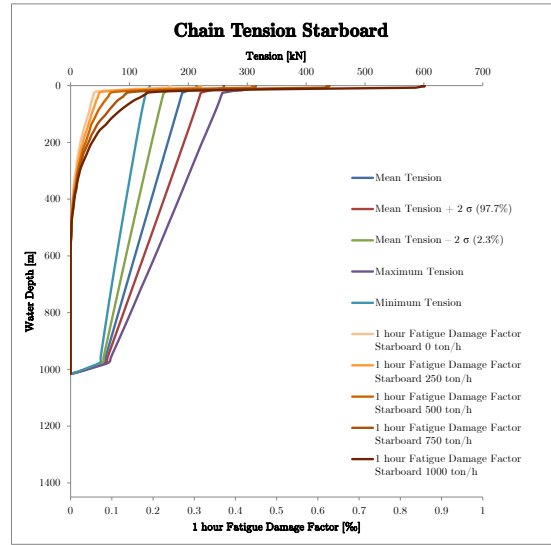


FIGURE D.36: Range graph for water depth of 1000m, significant wave height of 4m and a current of 0.2 m/s

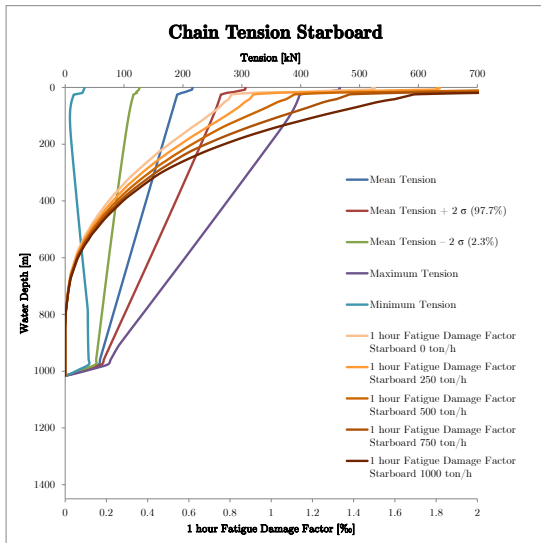


FIGURE D.37: Range graph for water depth of 1000m, significant wave height of 6m and a current of 0.2 m/s

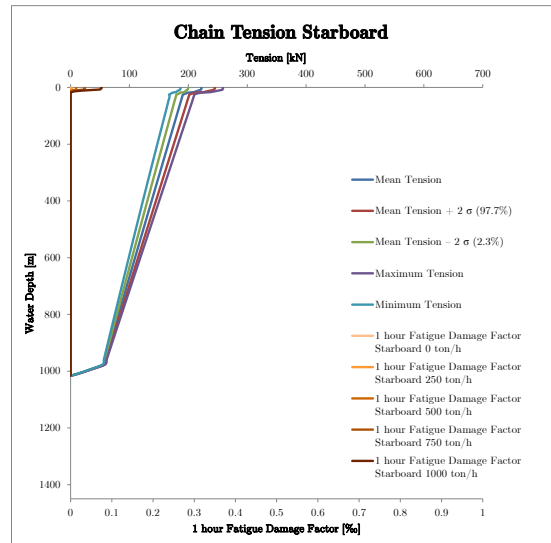


FIGURE D.38: Range graph for water depth of 1000m, significant wave height of 2m and a current of 0.4 m/s

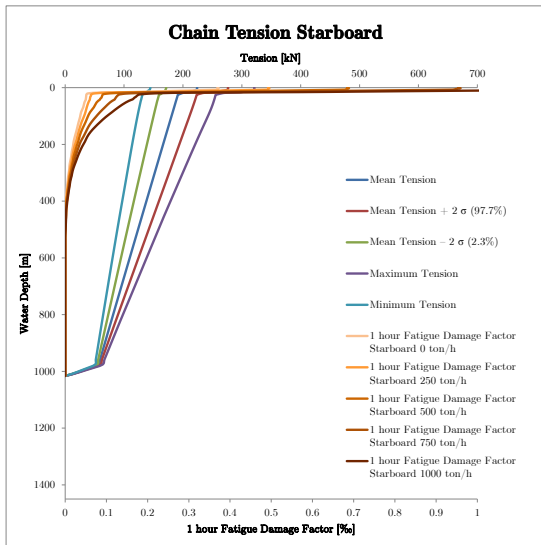


FIGURE D.39: Range graph for water depth of 1000m, significant wave height of 4m and a current of 0.4 m/s

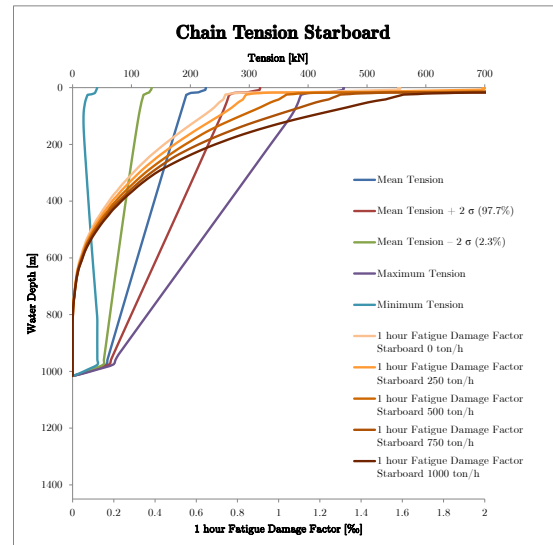


FIGURE D.40: Range graph for water depth of 1000m, significant wave height of 6m and a current of 0.4 m/s

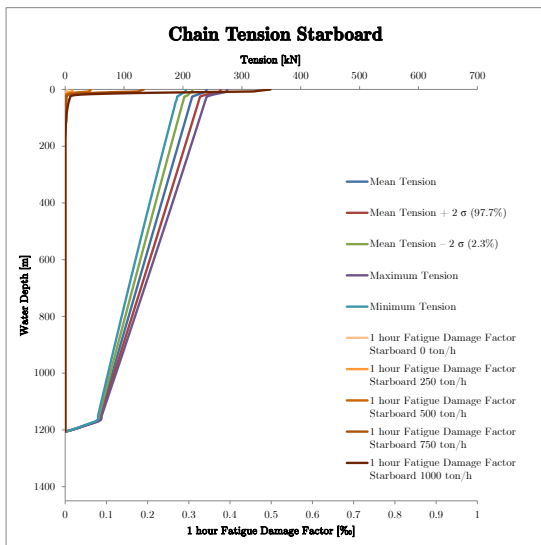


FIGURE D.41: Range graph for water depth of 1200m, significant wave height of 2m and no current

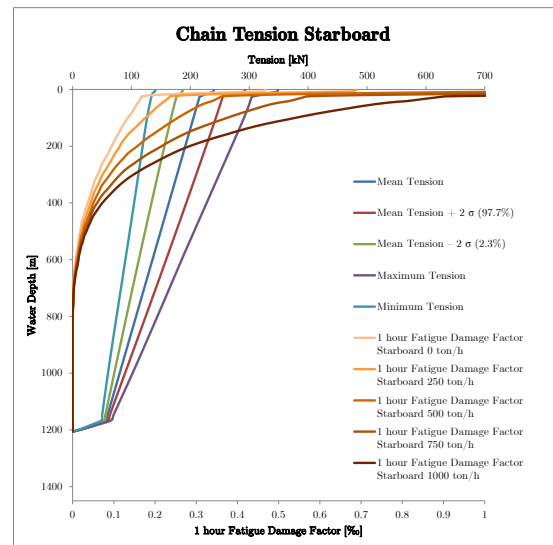


FIGURE D.42: Range graph for water depth of 1200m, significant wave height of 4m and no current

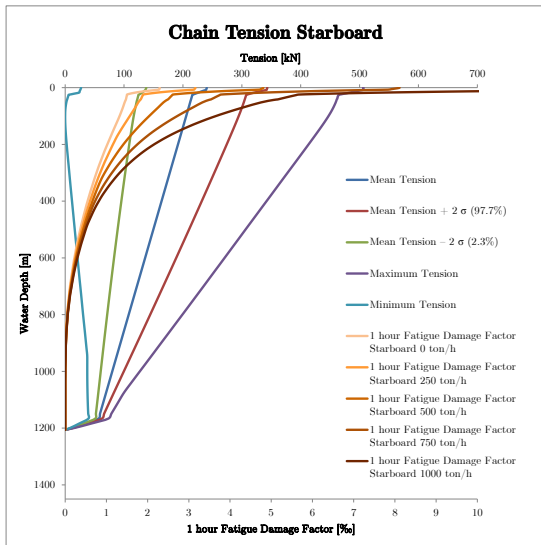


FIGURE D.43: Range graph for water depth of 1200m, significant wave height of 6m and no current

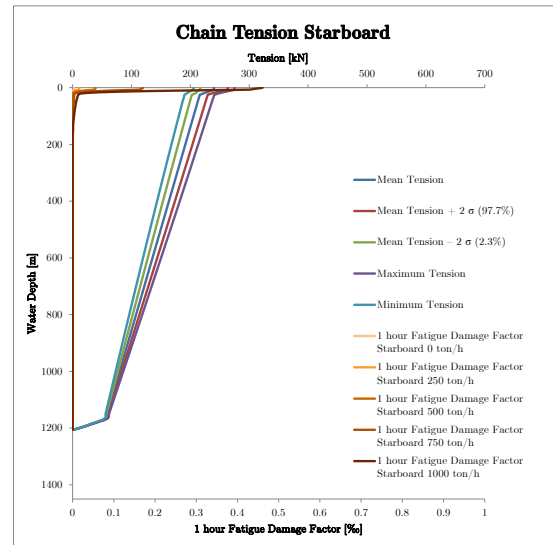


FIGURE D.44: Range graph for water depth of 1200m, significant wave height of 2m and a current of 0.2 m/s

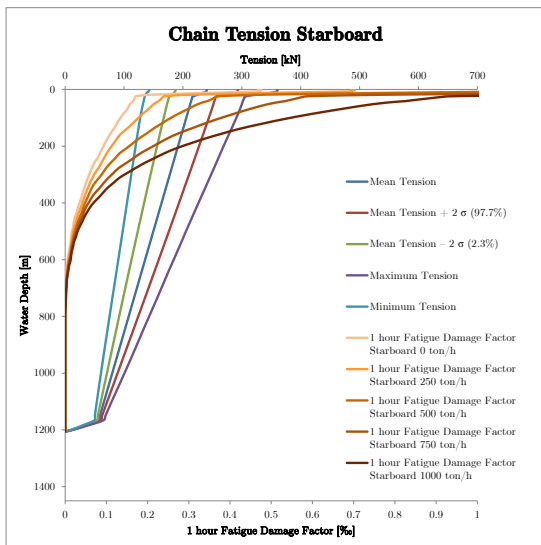


FIGURE D.45: Range graph for water depth of 1200m, significant wave height of 4m and a current of 0.2 m/s

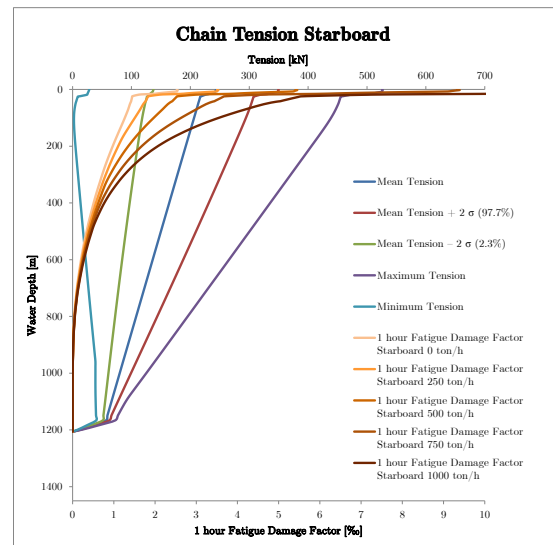


FIGURE D.46: Range graph for water depth of 1200m, significant wave height of 6m and a current of 0.2 m/s

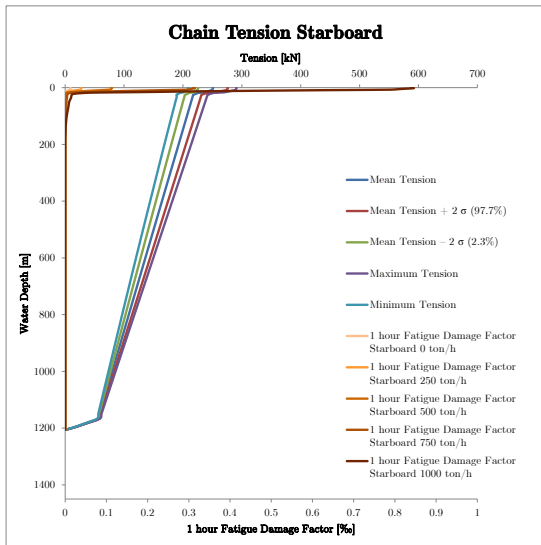


FIGURE D.47: Range graph for water depth of 1200m, significant wave height of 2m and a current of 0.4 m/s

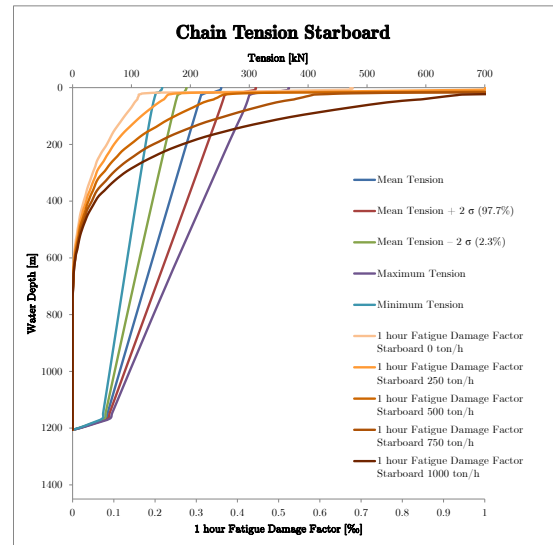


FIGURE D.48: Range graph for water depth of 1200m, significant wave height of 4m and a current of 0.4 m/s

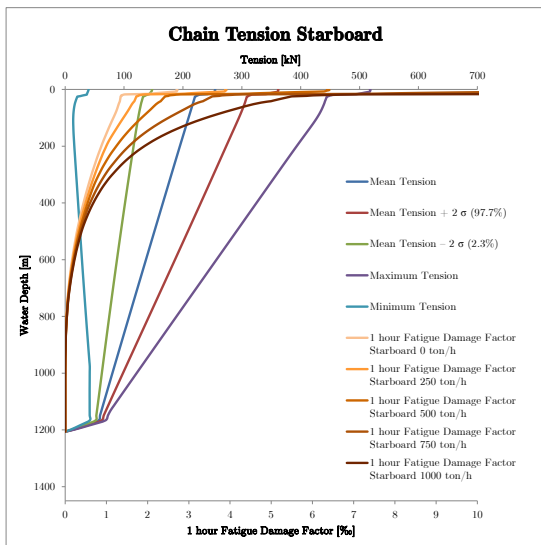


FIGURE D.49: Range graph for water depth of 1200m, significant wave height of 6m and a current of 0.4 m/s

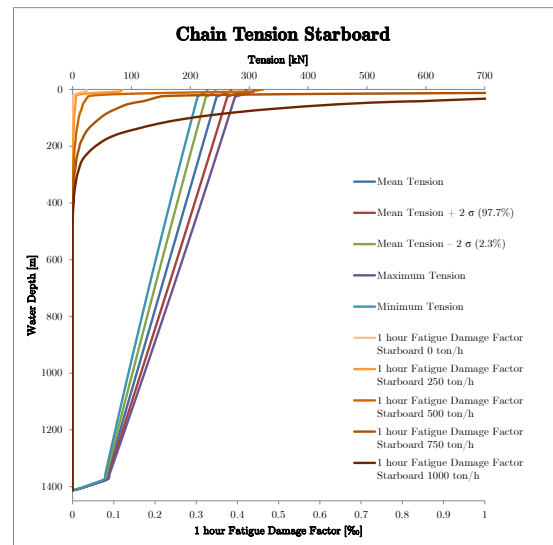


FIGURE D.50: Range graph for water depth of 1400m, significant wave height of 2m and no current

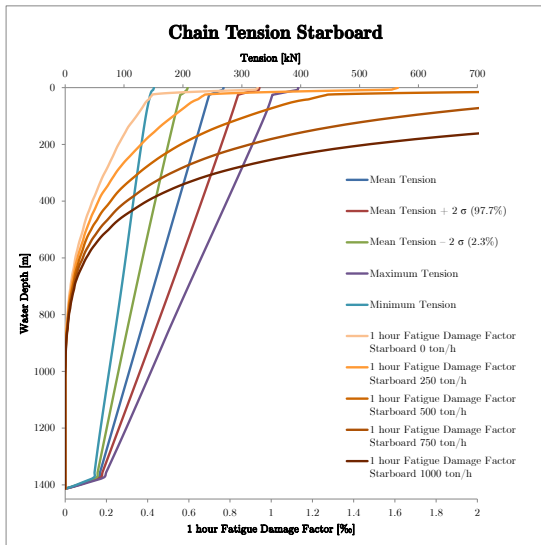


FIGURE D.51: Range graph for water depth of 1400m, significant wave height of 4m and no current

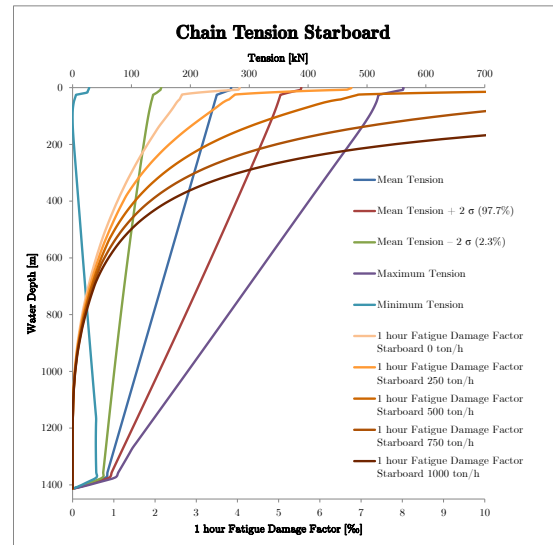


FIGURE D.52: Range graph for water depth of 1400m, significant wave height of 6m and no current

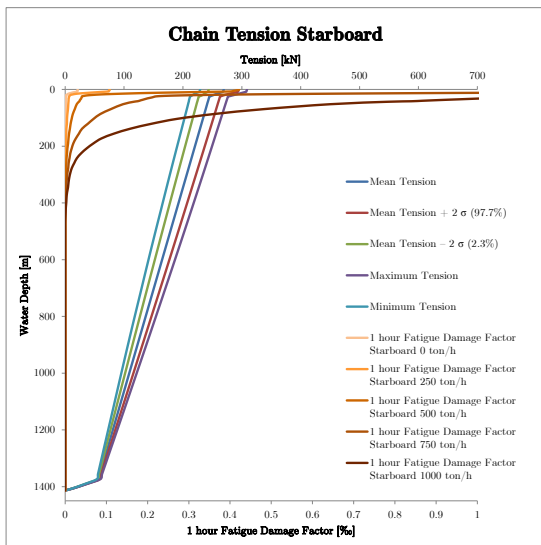


FIGURE D.53: Range graph for water depth of 1400m, significant wave height of 2m and a current of 0.2 m/s

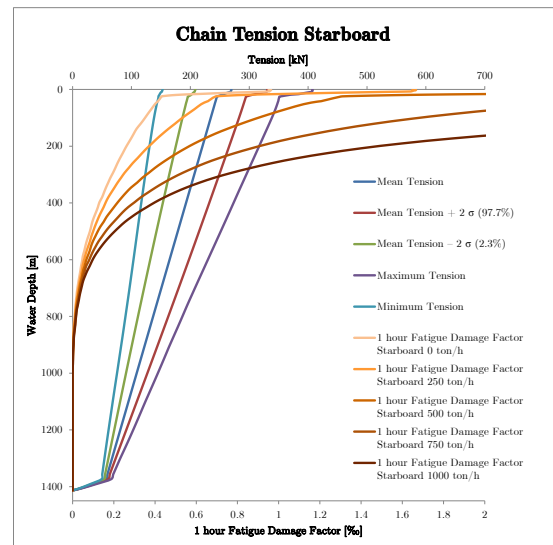


FIGURE D.54: Range graph for water depth of 1400m, significant wave height of 4m and a current of 0.2 m/s

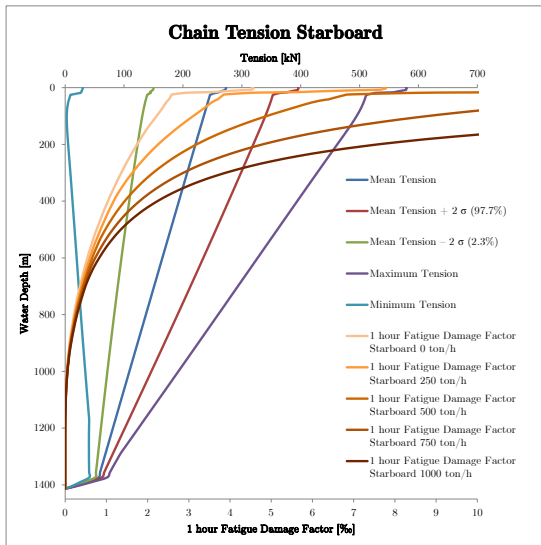


FIGURE D.55: Range graph for water depth of 1400m, significant wave height of 6m and a current of 0.2 m/s

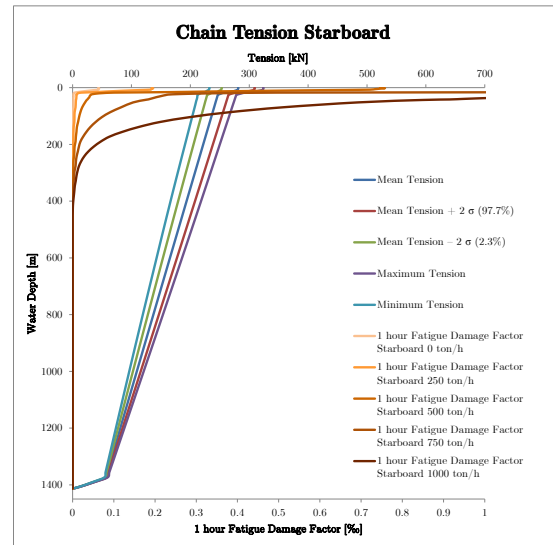


FIGURE D.56: Range graph for water depth of 1400m, significant wave height of 2m and a current of 0.4 m/s

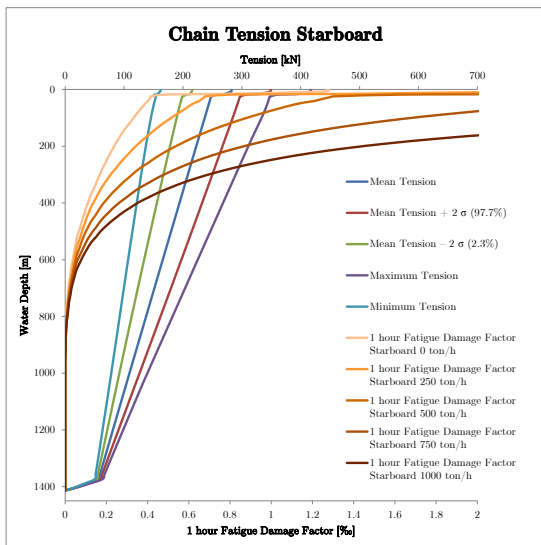


FIGURE D.57: Range graph for water depth of 1400m, significant wave height of 4m and a current of 0.4 m/s

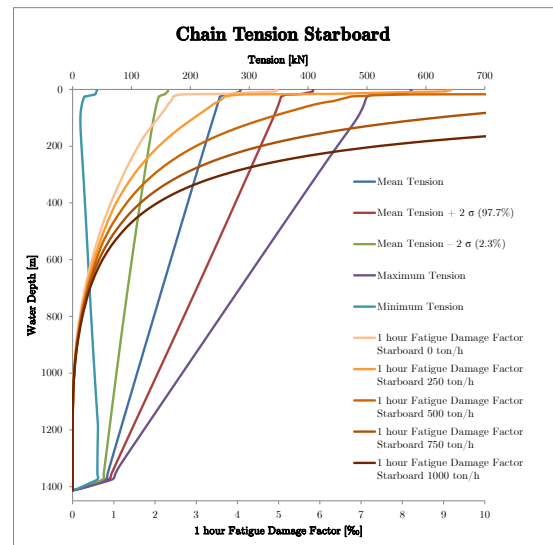


FIGURE D.58: Range graph for water depth of 1400m, significant wave height of 6m and a current of 0.4 m/s

D.3 Extreme Current Scenarios Results

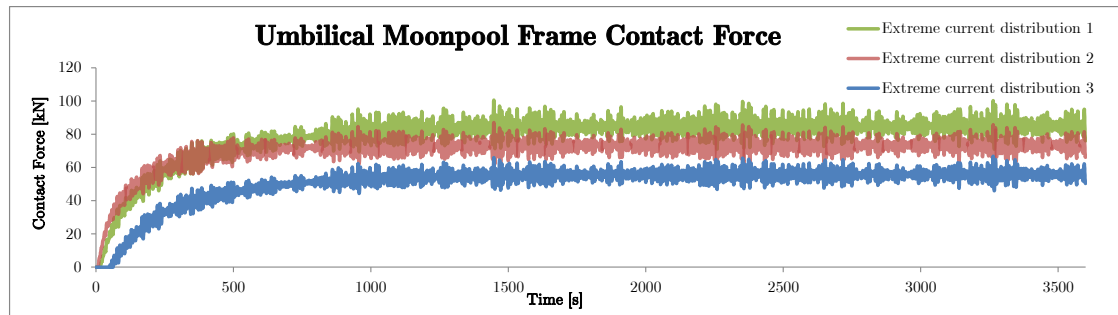


FIGURE D.59: Umbilical Moonpool Frame Contact Force for three Extreme Current Distributions

D.4 Directional Current Profiles Scenarios Results

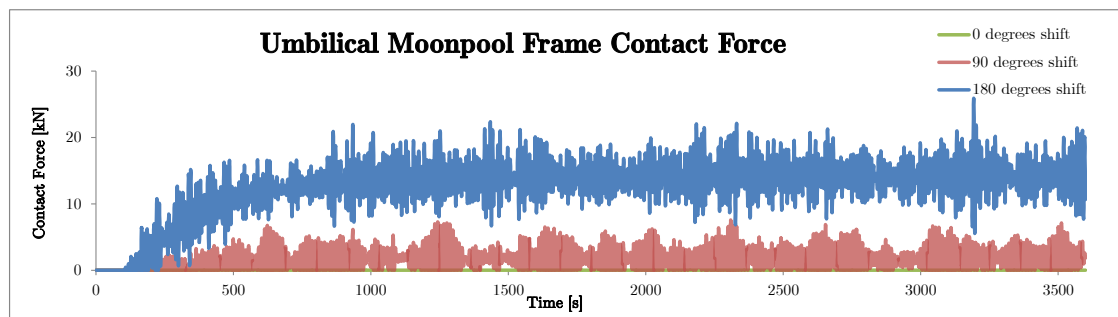


FIGURE D.60: Umbilical Moonpool Frame Contact Force for a Vessel Velocity of 0.15 m/s and three Directional Current Profiles

D.5 Subsea Rock Installation Scenarios Results

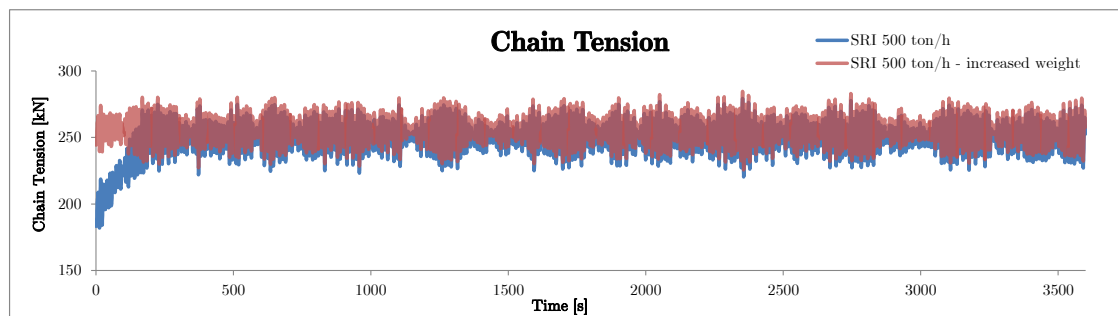


FIGURE D.61: Chain Tension Comparison - Simulating SRI versus Increased Self Weight for 2m waves and 500 ton/h

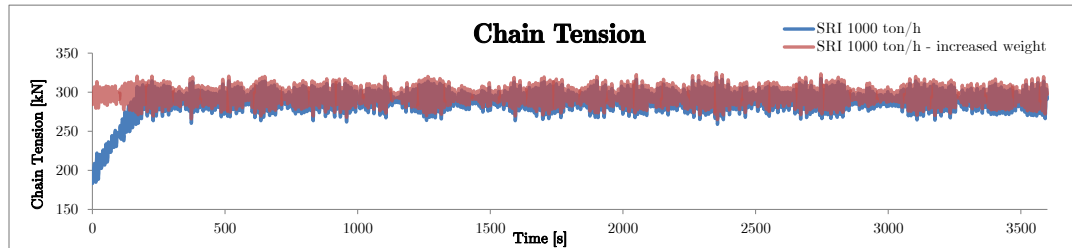


FIGURE D.62: Chain Tension Comparison - Simulating SRI versus Increased Self Weight for 2m waves and 1000 tonnes/h

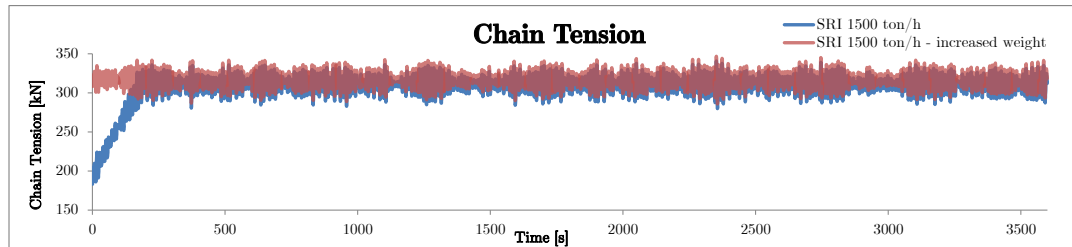


FIGURE D.63: Chain Tension Comparison - Simulating SRI versus Increased Self Weight for 2m waves and 1500 tonnes/h

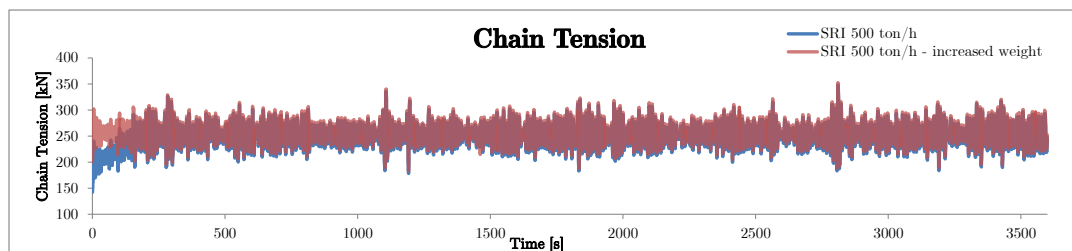


FIGURE D.64: Chain Tension Comparison - Simulating SRI versus Increased Self Weight for 4m waves and 500 tonnes/h

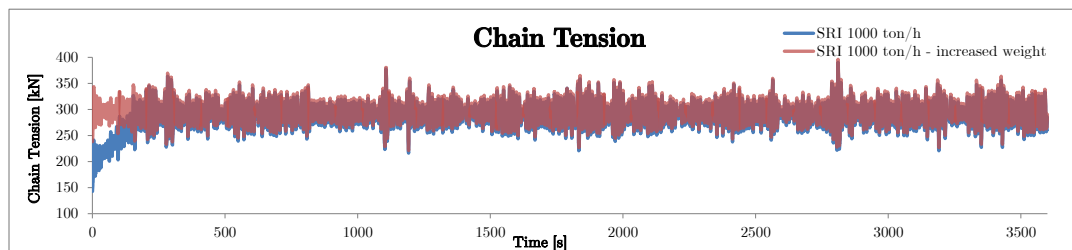


FIGURE D.65: Chain Tension Comparison - Simulating SRI versus Increased Self Weight for 4m waves and 1000 tonnes/h

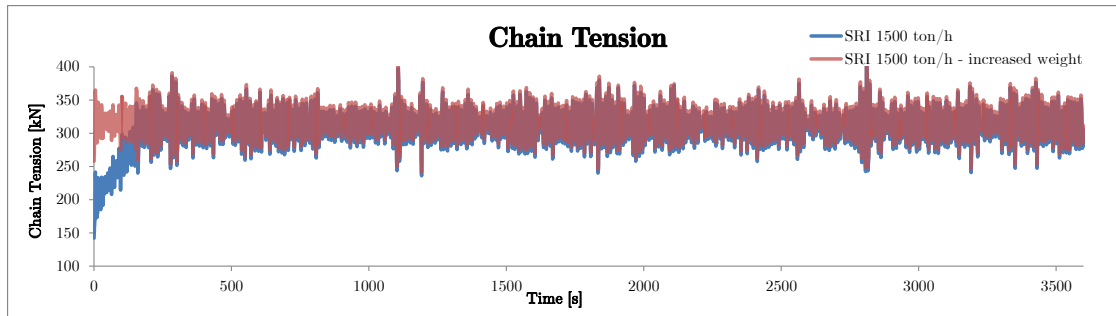


FIGURE D.66: Chain Tension Comparison - Simulating SRI versus Increased Self Weight for 4m waves and 1500 tonnes/h

D.6 Deepwater Buckets Scenarios Results

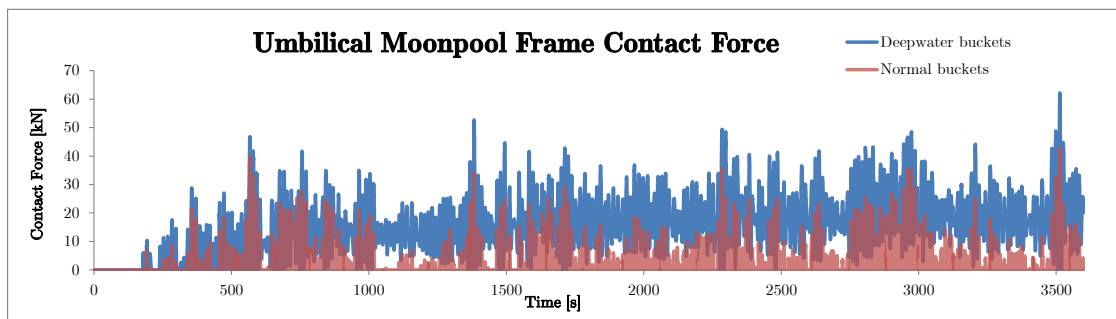


FIGURE D.67: Umbilical Moonpool Frame Contact Force for Normal and Deepwater Buckets

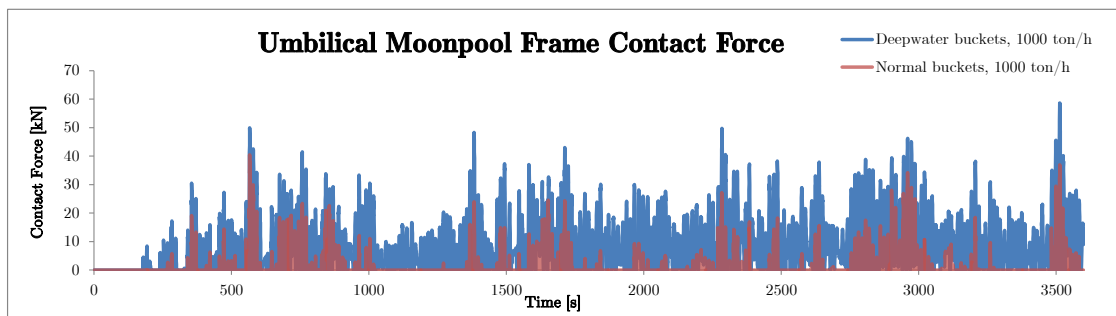


FIGURE D.68: Umbilical Moonpool Frame Contact Force for Normal and Deepwater Buckets - SRI 1000 tonnes/h

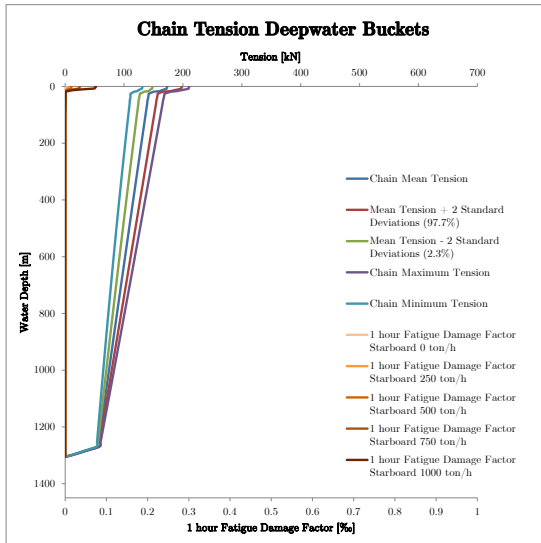


FIGURE D.69: Deepwater Buckets - Range graph for water depth of 1300m, significant wave height of 2m and 0.3 m/s current

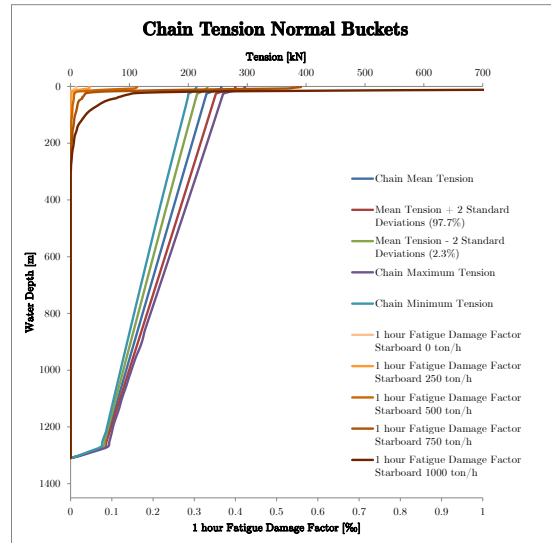


FIGURE D.70: Normal Buckets - Range graph for water depth of 1300m, significant wave height of 2m and 0.3 m/s current

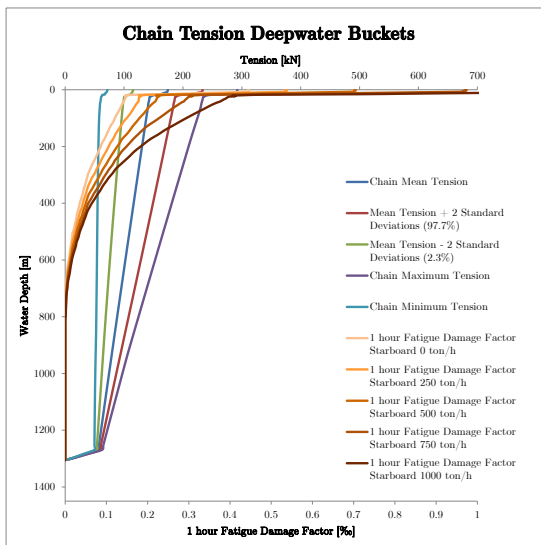


FIGURE D.71: Deepwater Buckets - Range graph for water depth of 1300m, significant wave height of 4m and 0.3 m/s current

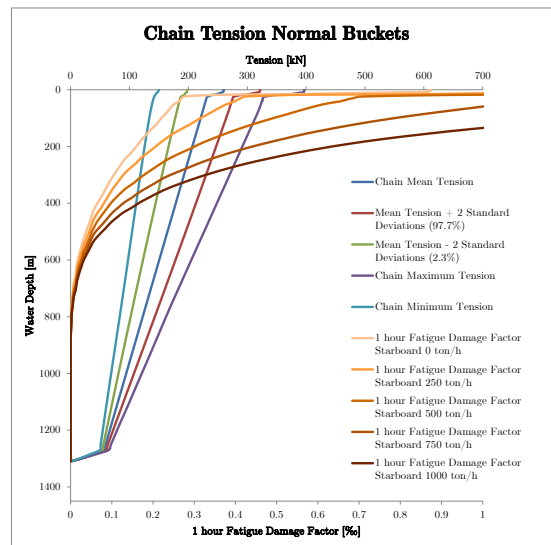


FIGURE D.72: Normal Buckets - Range graph for water depth of 1300m, significant wave height of 4m and 0.3 m/s current

D.7 Vessel Loading Condition Scenario Results

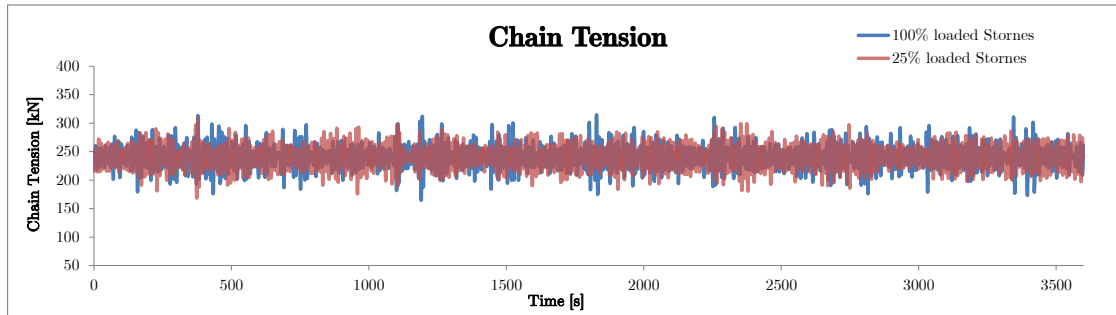


FIGURE D.73: Chain Tension - Stornes 100% loaded versus 25% loaded

D.8 Finite Element Model Results

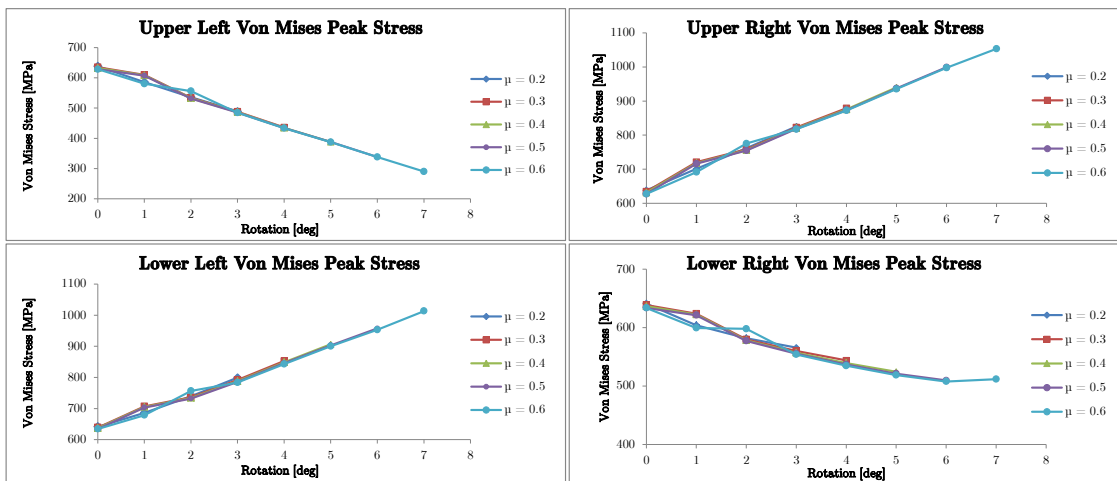


FIGURE D.74: FEA Full Chain Link Model - Von Mises Peak Stresses during Chain Link Rotations

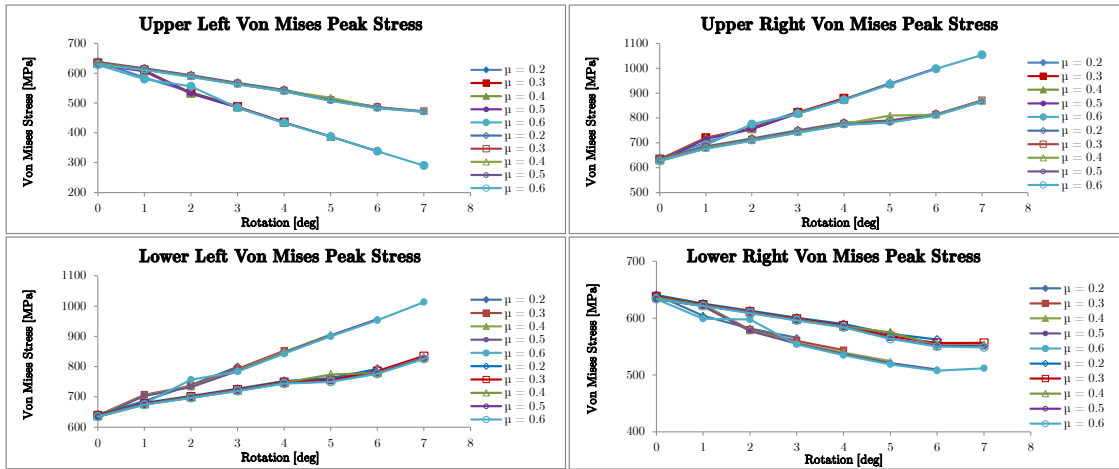


FIGURE D.75: FEA Full Chain Link Model - Von Mises Peak Stresses during Chain Link Rotations

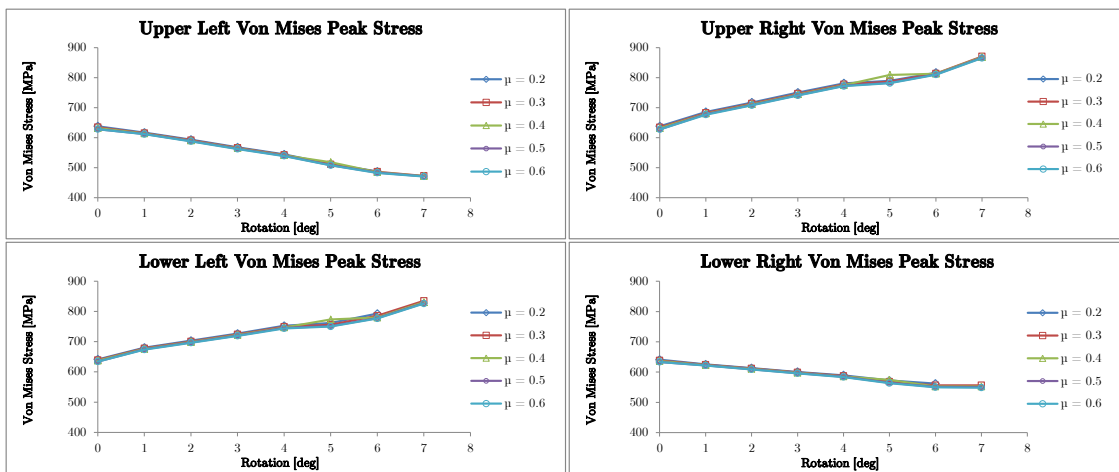


FIGURE D.76: FEA Full Chain Link Model - Von Mises Peak Stresses during Double Chain Link Rotations

Bibliography

- R.J. de Heer. De ontwikkeling van het stenenstorten onder water: Van zinkstuk tot valpijp - ROV, December 2008.
- B3D. Flexible Fall Pipe Vessel Stornes. [VIDEO], April 2013.
- RUD Ketten. Bulkos: Customised Conveyor Systems for Bulk Materials, May 2012. Third edition.
- Van Oord. Flexible Fall Pipe Vessel Nordnes: Investigation into the breakage of Dominators, November 2008.
- Van Oord. Additional Incident Investigation Report: Stornes Fall Pipe Failure, November 2012. VOMS-PR1.07-TE-01.
- J.J. Xiong and R.A. Shenoi. Deterministic Theorem on Fatigue and Fracture. In *Fatigue and Fracture Reliability Engineering*, Springer Series in Reliability Engineering, pages 1–26. Springer London, 2011. ISBN 978-0-85729-217-9.
- D. Socie and G. Malton. eFatigue, June 2009. URL <http://www.efatigue.com/>.
- D. Marghitu. *Mechanical Engineer's Handbook*. Academic Press, Amsterdam, Boston, 2001. ISBN 978-0-080-51136-8.
- M. Matsuishi and T. Endo. Fatigue of Metals subjected to Varying Stress. 1968. Japan Society of Mechanical Engineering.
- R.R. Rossi. A Review of Fatigue Curves for Mooring Lines. In *Proceedings of the 24th International Conference on Ocean, Offshore and Arctic Engineering*. American Society of Mechanical Engineers, June 2005. OMAE2005-67583.
- I. Celander and A.B. Strom-Ljusne. Preload Influence on Fatigue Characteristics of Chain Cable Exposed to Salt Water and Atmospheric Conditions. 1972.
- G.J. Shoup, S.M. Tipton, and J.R. Sorem. The Effect of Proof Loading on the Fatigue Behaviour of Stud Link Chain. *International Journal of Fatigue*, 14(1):35–40, 1992. ISSN 0142-1123.

- H. Gudehus. *Leitfaden für eine Betriebsfestigkeitsrechnung: Empfehlungen zur Lebensdauerabschätzung von Maschinenbauteilen*. Stahleisen GmbH, 1999. ISBN 9783514005846.
- Noble Denton. Floating Production System: JIP FPS mooring integrity, 2006. Health and Safety Executive.
- Det Norske Veritas. Position Mooring, October 2010. Offshore Standard:DNV-OS-E301.
- P. Vargas and P. Jean. FEA of Out-of-Plane Fatigue Mechanism of Chain Links. In *Proceedings of the 24th International Conference on Ocean, Offshore and Arctic Engineering*. American Society of Mechanical Engineers, June 2005. OMAE2005-67354.
- C. Melis, P. Jean, and P. Vargas. Out-of-Plane Bending Testing of Chain Links. In *Proceedings of the 24th International Conference on Ocean, Offshore and Arctic Engineering*. American Society of Mechanical Engineers, June 2005. OMAE2005-67353.
- J. van der Cammen, E. ter Brake, and R. Uittenbogaard. Calculation Methodology of Out of Plane Bending of Mooring Chains. In *Proceedings of the 26th International Conference on Ocean, Offshore and Arctic Engineering*. American Society of Mechanical Engineers, June 2007. OMAE2007-29178.
- T. Lassen, E. Storvoll, and A. Bech. Fatigue Life Prediction of Mooring Chains subjected to Tension and Out-of-Plane Bending. In *Proceedings of the 28th International Conference on Ocean, Offshore and Arctic Engineering*. American Society of Mechanical Engineers, May 2009. OMAE2009-79253.
- R. Stephen. Fatigue and Fracture Toughness of Five Carbon or Low Alloy Cast Steels at Room Temperature or Low Climate Temperature. Research Report No. 94A, Steel Founders' Society of America, October 1982.
- Orcina. *OrcaFlex Manual*. Orcina Limited, Daltongate, Ulverston, Cumbria, LA12 7AJ, United Kingdom, October 2012. Version 9.6a.
- Ansys. *Basic Analysis Guide*. Ansys Incorporated, 275 Technology Drive, Canonsburg, PA 15317, United Kingdom, January 2007. Release 11.0.
- Ansys. *Contact Technology Guide*. Ansys Incorporated, 275 Technology Drive, Canonsburg, PA 15317, United Kingdom, November 2009. Release 12.1.
- A. Niesłony. Determination of Fragments of Multiaxial Service Loading strongly influencing the Fatigue of Machine Components. *Mechanical Systems and Signal Processing*, 23(8):2712–2721, 2009.

- M. Hück, L. Thrainer, and W. Schütz. *Berechnung von Wöhlerlinien für Bauteile aus Stahl, Stahlguß und Grauguß - Synthetische Wöhlerlinien*. Bericht des Vereins zur Förderung der Forschung im Transportwesen der Eisenhüttenindustrie. Stahleisen GmbH, 1983.
- E. Haibach and G. Pahl. *Betriebsfeste Bauteile: Ermittlung und Nachweis der Betriebsfestigkeit*. Springer-Verlag, 1992. ISBN 3540548157.
- E. Haibach. *Betriebsfestigkeit: Verfahren und Daten zur Bauteilberechnung*. VDI-Verl., 1989. ISBN 3184008282.
- Yung-Li Lee, Mark E. Barkey, and Hong-Tae Kang. *Metal Fatigue Analysis Handbook - Practical Problem-solving Techniques for Computer-aided Engineering*. Elsevier, Amsterdam, 2012. ISBN 978-0-123-85204-5.
- American Petroleum Institute. Design and Analysis of Stationkeeping Systems for Floating Structures, May 2008. Recommended Practice: API RP 2SK.
- Deutsches Institut für Normung. DIN 22252:2012-07, July 2012. Norm.
- J.J. Stiff, D.W. Smith, and N.F. Casey. Fatigue of Mooring Chain in Air and Water - Results and Analysis. In *Proceedings of the 28th Annual Offshore Technology Conference*, pages 291–297. Noble, Denton and Associates, Offshore Technology Conference, May 1996. OTC 8147.
- Statoil. Ormen Lange gas field, May 2013. URL <http://www.statoil.com/en/eurooperations/explorationprod/partneroperatedfields/ormenlange/pages/default.aspx>.
- Google Maps. Location of the Ormen Lange gas field, August 2013. URL <https://maps.google.nl/>.